

Dissertations and Theses

7-2014

Early Damage State Criterion from a Fault-Seeded Helicopter Gear Using Acoustic Emission and Neural Networks

Rudy L. Baum

Embry-Riddle Aeronautical University - Daytona Beach

Follow this and additional works at: <http://commons.erau.edu/edt>



Part of the [Aerospace Engineering Commons](#), and the [Mechanical Engineering Commons](#)

Scholarly Commons Citation

Baum, Rudy L., "Early Damage State Criterion from a Fault-Seeded Helicopter Gear Using Acoustic Emission and Neural Networks" (2014). *Dissertations and Theses*. Paper 20.

EARLY DAMAGE STATE CRITERION FROM A FAULT-SEEDED HELICOPTER GEAR USING ACOUSTIC EMISSION AND NEURAL NETWORKS

by

Rudy L. Baum

A Thesis Submitted to the College of Engineering Department of Mechanical
Engineering in Partial Fulfillment of the Requirements for the Degree of
Master of Science in Mechanical Engineering

Embry-Riddle Aeronautical University

Daytona Beach, Florida

July 2014

EARLY DAMAGE STATE CRITERION FROM A FAULT-SEEDED HELICOPTER GEAR USING ACOUSTIC EMISSION AND NEURAL NETWORKS

by

Rudy L. Baum

This thesis was prepared under the direction of the candidate's Thesis Committee Chair:

Dr. Fady F. Barsoum, Professor of Mechanical Engineering at Embry-Riddle Aeronautical University, and has been approved by thesis Committee Members: Dr. Daewon Kim, Assistant Professor of Aerospace Engineering at Embry-Riddle Aeronautical University, and Dr. George Atia, Assistant Professor of Electrical Engineering at University of Central Florida. It was submitted to the Department of Mechanical Engineering in partial fulfillment of the requirements for the degree of Master of Science in Mechanical Engineering

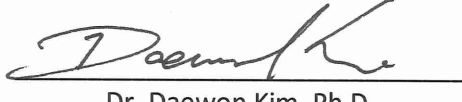
THESIS REVIEW COMMITTEE:



Dr. Fady F. Barsoum, Ph.D.
Committee Chair



Dr. George Atia, Ph.D.
Committee Member



Dr. Daewon Kim, Ph.D.
Committee Member


Dr. Charles F. Reinholtz, Ph.D.
Department Chair, Mechanical Engineering

7/25/14
Date


Dr. Robert Oxley, Ph.D.
Associate Vice President of Academics

7/31/2014
Date

ACKNOWLEDGEMENTS

First and foremost I would like to thank God. I whole-heartedly admit His support was present through thick and thin and I could not have succeeded without His support.

I would like to express a sincere appreciation to my adviser, Dr. Barsoum, for his guidance and wisdom throughout the journey. His high standards of expectations and tough love have helped push me to seek continuous improvement. I am also grateful for the life lessons you have provided to me outside of academia. They will continue to guide me as my career progresses. I would also like to thank Dr. Kim and Dr. Gangadharan for their support and allowing me to be a part of other projects outside of my AE research.

I sincerely appreciate Dr. Atia's willingness to be a part of my committee on such short notice and the valuable input he provided.

In working with other students at Embry-Riddle I was able to meet some great friends and learn a lot about myself. I enjoyed the motivation and energy Kiwoong would bring to the work environment. I would have been distraught without the intellectual discussions with Lenny, Thiago, Vikram, and Shane. I have the highest expectations for all of you and wish you the best of luck with your careers.

Last and certainly not least for the support of my friends and family - to my parents Ray and Leslie, and my girlfriend, Katie, for pushing me to be the best that I can be. I love you and don't know who or what I would be without you. I would like to extend a shout out to Joshua for convincing me to apply to Embry-Riddle. I am appreciative to my lab buddies, Balaji, Boutros and Audrey for bringing a high energy environment to the lab.

ABSTRACT

Researcher: Rudy L. Baum

Title: Early Damage State Criterion from a Fault-Seeded Helicopter Gear Using Acoustic Emission and Neural Networks

Institution: Embry-Riddle Aeronautical University

Degree: Master of Science in Mechanical Engineering

Year: 2014

In response to five failures since 2008 of the tail gearbox of multiple models of Sikorsky's H-60 helicopter, acoustic emission (AE) data collected from a rotating gearbox test stand at the Naval Air Station in Patuxtent River, MD, was used to monitor the initiation and propagation of a flaw from an electro-discharge machined (EDM) notch seeded on the face of a gear tooth. A period of testing was considered which spanned ~300,000 seconds or ~83 hours and culminates to a damage state such that a flaw has initiated on both ends of the EDM notch. AE data was analyzed for three separate channels which span a wide range of amplitude thresholds using clustering methods and verification algorithms developed at the Embry-Riddle Aeronautical University (ERAU) Structure Health Monitoring (SHM) and Nondestructive Evaluation (NDE) Laboratory. Energy, duration, amplitude, and average frequency of the AE signals were input into the Kohonen Self-Organizing Map (KSOM) artificial neural network (ANN) function in NeuralWorks Professional II/Plus software to separate cracking signals from other mechanisms such as noise and plastic deformation. Visual inspection and statistical analysis of the data in the AE plots created using the output ANN results was used to

separate the cluster(s) which exhibited higher amplitude and energy, and lower duration and average frequency; hits typical to cracking. The similarities and differences in the progression of clusters sourced to cracking for each of the three channels is discussed. Cumulative testing time plots of AE parameters were compiled using both entire data sets and using clusters representative of cracking mechanisms. Replica cross sections which were taken throughout testing visually display, in chronological fashion, circumferential crack growth across gear splines adjacent to the spline with the EDM notch. Data analysis techniques are used in conjunction with replica cross sections to provide insight into the AE activity for crack initiation and crack propagation and define early damage state detection criterion for rotary components.

TABLE OF CONTENTS

ACKNOWLEDGEMENTS	iii
ABSTRACT	iv
LIST OF TABLES	x
LIST OF FIGURES.....	xi
LIST OF ABBREVIATIONS AND NOMENCLATURE	xiv
CHAPTER 1 - Introduction.....	15
1.1 Thesis Objective.....	15
1.2 Background	15
1.2.1 H-60 Overview.....	16
1.2.2 Tail Gearbox Output Bevel Gear Specifics	17
1.2.3 Root Cause	18
CHAPTER 2 – Principles of Acoustic Emission Non-Destructive Evaluation.....	20
2.1 Nondestructive Evaluation Overview	20
2.2 Other Nondestructive Testing Methods	20
2.3 Acoustic Emission	22
2.3.1 History of Acoustic Emission Testing	22
2.3.2 Acoustic Emission as a Nondestructive Testing Method	23
2.3.3 Acoustic Emission Structure Health Monitoring	24
2.4 Acoustic Emission Data Acquisition	24
2.4.1 AE Piezoelectric Transducers	25
2.4.2 AE Signal Parameters	26
2.4.3 Layout File Parameters	27
CHAPTER 3 – Literature Review	29

3.1 Characteristics of Failure Mechanisms in Metal Specimens using AE Data	29
3.2 Prognostics and Health Assessment of Rotary Components	31
3.2.1 Notable Former Investigations.....	31
3.2.2 ERAU Research Summary for 2010 and 2011 OBG Testing.....	31
3.2.3 AE Structural Health Monitoring of Helicopter Power Train Gearbox	34
3.3 Acoustic Emission Crack Initiation of Cyclically Loaded Specimens	34
3.4 Acoustic Emission as a Basis for Crack Growth Rate Models	35
3.5 Gearbox and Rotating Machinery Overview	40
3.5.1 Gear Failure Modes.....	40
CHAPTER 4 – H60 Tail Rotor Gearbox Experimental Setup	42
4.1 Ground Test Stand	42
4.2 Load Conditions and Testing Procedure	43
4.3 Electro-Discharge Machined Notch.....	48
4.4 AE Data Collection	49
4.4.1 Data Acquisition and PZT Transducer Locations.....	49
4.4.2 Layout File Parameters	51
CHAPTER 5 – Data Analysis and Research Methodologies	53
5.1 Summary of Collected AE Data	53
5.2 Data Analysis and Research Methodology Flow Chart.....	55
5.3 Navair AE Sensor Data Processing.....	57
5.3.1 Navair Channel Selection	57
5.3.2 Navair Data Pre-processing and Filtering.....	58
5.4 ERAU AE Sensor Data Processing.....	60
5.4.1 ERAU Channel Selection	60

5.4.2 ERAU Data Pre-Processing and Filtering.....	64
5.5 Data Clustering Algorithm.....	65
5.5.1 Artificial Neural Networks	68
5.5.2 Kohonen Self-Organizing Map.....	68
5.5.3 AE Plot Verification	71
5.6 Approach for Early Damage State AE Data Behavior Characterization	73
5.6.1 Clustered Plot Inspection	73
5.6.2 Cumulative Plot Inspection.....	74
CHAPTER 6 - Results	75
6.1 Early Damage State Replica Cross Section	75
6.2 Navair Data Clustered Plots Results	76
6.2.1 Channel 1 Clustered AE Plots.....	77
6.2.2 Channel 2 Clustered AE Plots.....	84
6.3 ERAU Data Clustered Plots Results.....	91
6.4 Cumulative Hit Count Plots	96
6.4.1 Navair Sensor Channel 1 and Channel 2	96
6.4.2 ERAU Sensor Channel 1	98
CHAPTER 7 – Conclusions and Recommendations.....	100
7.1 Conclusions.....	100
7.2 Recommendations.....	102
REFERENCES	104
APPENDICES.....	108
APPENDIX A – Clustered AE Plots	108
A.1 Navair Sensor Channel 1 Clustered AE Plots.....	108
A.2 Navair Sensor Channel 2 Clustered AE Plots.....	117

A.3 ERAU Sensor Channel 1 Clustered AE Plots.....	125
APPENDIX B – Sensor Specification Sheets.....	131
B.1 PAC R15I-AST AE Transducer Product Data Sheet	131
B.2 PAC WD AE Transducer Product Data Sheet	132
B.3 PAC Micro-30s AE Transducer Product Data Sheet	133
APPENDIX C – Lycoming T-53 Test Stand.....	134
C.1 Lycoming T-53 Test Stand Design	134
C.2 T-53 Test Stand Data Acquisition.....	136

LIST OF TABLES

Table	Page
Table 1 – Description of Other NDT Methods [7]	21
Table 2 – Description of Primary AE Signal Parameters [13].....	27
Table 3 – Description of Layout File Parameters	28
Table 4 – Characteristics of AE Parameters Associated with Failure Mechanisms in Metals [7]	30
Table 5 – Description of Gear Distress and Failure Modes [34]	40
Table 6 – Early Damage Testing Interval Test Points	44
Table 7 – Load Conditions.....	44
Table 8 – Test Point Operating Procedure.....	45
Table 9 – Navair and ERAU Sensor Amplitude Threshold Settings.....	51
Table 10 – Layout File Settings Common To Navair and ERAU Sensors	52
Table 11 – AE Data File Size Comparison between ERAU and Navair Sensors	54
Table 12 – Summary of Number of Hits in Figure 23 through Figure 26.....	63
Table 13 - Characteristics of AE Parameters Associated with Failure Mechanisms in Metals [7]	67

LIST OF FIGURES

Figure	Page
Figure 1 – Sikorsky MH60 Seahawk [4]	17
Figure 2 – (a) H60 Aircraft Tail [5] (b) H60 Tail Rotor [5] (c) H60 Tail Gearbox Schematic and Typical Crack Propagation Path [2]	17
Figure 3 – OBG Schematic [2] and Bi-Loading Scenario	18
Figure 4 – Typical OBG Fretting Corrosion and Pitting Wear [6]	19
Figure 5 – Basic AE Test Setup [9]	24
Figure 6 – AE Piezoelectric Transducer Schematic and Labeled Components [9]	25
Figure 7 – Primary AE Signal Parameters [13]	26
Figure 8 – Illustration of Predominant Fatigue Cracking Modes in Metallic Specimens [15].....	30
Figure 9 – Sample AE Plot from 2010 Testing [1]	33
Figure 10 – Cumulative AE Hit Count Profile for Cyclically Loaded Specimens [24]	35
Figure 11 – Harris and Dunegan Relationship for Metallic Specimens [24].....	37
Figure 12 – Energy Conversions between Source Energy and AE Event Energy [28].....	39
Figure 13 – H60 Tail Gearbox Ground Test Stand [2]	42
Figure 14 – Cumulative Early Damage Testing Interval Hub Moment Load Profile.....	45
Figure 15 - Cumulative Early Damage Testing Interval Tail Rotor Torque Load Profile.....	46
Figure 16 – Single Test Point Hub Moment Profile	47

Figure 17 – Single Test Point Tail Rotor Torque Profile.....	47
Figure 18 – OBG 3D Model with (a) Notch Location and (b) Notch Dimensions [2]	48
Figure 19 – AE Transducer Locations	50
Figure 20 – Data Processing and Analysis Methodology Flowchart.....	56
Figure 21 – Side-by-side Comparison of AE Plots for (a) 2010 H60 AE data versus (b) 2013 H60 AE data.....	58
Figure 22 – Sample Data Excerpt with Zero-value Hits.....	59
Figure 23 – Duration versus Counts plot for Sample ERAU Channel 1 Data.....	61
Figure 24 - Duration versus Counts plot for Sample ERAU Channel 2 Data	61
Figure 25 - Duration versus Counts plot for Sample ERAU Channel 3 Data	62
Figure 26 - Duration versus Counts plot for Sample ERAU Channel 4 Data	62
Figure 27 – (a) Duration versus Counts and (b) Amplitude versus Time plots of Raw ERAU Channel 1 Data for a Sample Test Date.....	64
Figure 28 – Sample AE Plot for 2013 H60 AE Data Using Seven Clusters	66
Figure 29 – Intricate Kohonen SOM [42].....	69
Figure 30 – Simplified Kohonen SOM Layout for 2013 H60 AE Analysis.....	70
Figure 31 – Visual Inspection of a Sample AE Plot for (a) Three Clusters and (b) Four Clusters	72
Figure 32 – Sample Verification Algorithm Output for Two, Three, and Four Clusters	73
Figure 33 – Early Damage Testing Interval Replica Cross Section	75
Figure 34 – Clustered AE Plot for 12/14/2012 Navair Sensor Channel 1 Data	77
Figure 35 - Clustered AE Plot for 01/11/2013 Navair Sensor Channel 1 Data	78
Figure 36 - Clustered AE Plot for 01/14/2013 Navair Sensor Channel 1 Data	79

Figure 37- Clustered AE Plot for 01/28/2013 Navair Sensor Channel 1 Data	80
Figure 38 - Clustered AE Plot for 01/29/2013 Navair Sensor Channel 1 Data	81
Figure 39 - Clustered AE Plot for 02/05/2013 Navair Sensor Channel 1 Data	82
Figure 40 - Clustered AE Plot for 02/07/2013 Navair Sensor Channel 1 Data	83
Figure 41 - Clustered AE Plot for 12/14/2012 Navair Sensor Channel 2 Data	84
Figure 42 - Clustered AE Plot for 01/03/2013 Navair Sensor Channel 2 Data	85
Figure 43 - Clustered AE Plot for 01/10/2013 Navair Sensor Channel 2 Data	86
Figure 44 - Clustered AE Plot for 01/14/2013 Navair Sensor Channel 2 Data	87
Figure 45 - Clustered AE Plot for 01/28/2013 Navair Sensor Channel 2 Data	88
Figure 46 - Clustered AE Plot for 01/29/2013 Navair Sensor Channel 2 Data	89
Figure 47 - Clustered AE Plot for 02/05/2013 Navair Sensor Channel 2 Data	90
Figure 48 - Clustered AE Plot for 02/11/2013 Navair Sensor Channel 2 Data	91
Figure 49 - Clustered AE Plot for 12/14/2012 ERAU Sensor Channel 1 Data	93
Figure 50 - Clustered AE Plot for 01/03/2013 ERAU Sensor Channel 1 Data	94
Figure 51 - Clustered AE Plot for 01/11/2013 ERAU Sensor Channel 1 Data	95
Figure 52 – Cumulative Hit Count Profile for Navair Sensor Channel 1 Data	96
Figure 53 – Cumulative Hit Count Profile for Navair Sensor Channel 2 Data	97
Figure 54 – Cumulative Hit Count Profile for ERAU Sensor Channel 1 Data	98

LIST OF ABBREVIATIONS AND NOMENCLATURE

ERAU	Embry-Riddle Aeronautical University
SHM	Structure Health Monitoring
NDE	Nondestructive Evaluation
AE	Acoustic Emission
AET	Acoustic Emission Testing
TGB	Tail Gearbox
OBG	Output Bevel Gear
EI	Engineering Investigations
EDM	Electro-Discharge Machined
STTR	Small Business Technology Transfer
ASNT	American Society of Nondestructive Testing
NDT	Nondestructive Testing
SOM	Self-Organizing Map
ANN	Artificial Neural Networks
PE	Processing Elements
LEFM	Linear Elastic Fracture Mechanics
H&D	Harris and Dunegan
CW	Clockwise
CCW	Counter-Clockwise
PAC	Physical Acoustics Corporation

CHAPTER 1 - Introduction

1.1 Thesis Objective

This thesis suggests early damage state detection methods and criterion of fault-seeded gearbox components using acoustic emission (AE) data collected from a Navair sponsored Sikorsky H-60 tail rotor experiment. AE data clustering algorithms developed at the Embry-Riddle Aeronautical University (ERAU) Structure Health Monitoring (SHM) and Nondestructive Evaluation (NDE) Laboratory [1] were used to discriminate between fatigue events and noise signals common to rotary component operation. Theoretical models which relate fracture mechanics energy release parameters and material boundary conditions to crack growth rates are explored.

1.2 Background

As of December 2008, there have been six recorded failures of the tail gearbox (TGB) output bevel gear (OBG) associated with different Sikorsky Blackhawk aircraft variations. Engineering Investigations (EI) associated with each incident failure has revealed a crack located circumferentially along the male splines of the OBG [2]. In response to these incidences, Navair was contracted to investigate the crack growth rate of a crack propagating on the OBG splines and ultimately develop a strategic plan of action to detect and periodically monitor the OBG in the instance a crack is detected. The H-60 TGB OBG Spline Crack Growth Test was conceived in December 2008 and progressed until termination in November 2013. In that time, three separate OBG parts were fault-seeded with an electro-discharge machine (EDM) notch and tested.

AE Data was collected from an experimental setup located at the Naval Air Station in Patuxtent River, Maryland. Through a Small Business Technology Transfer (STTR) program, AE data collected from the OBG experimental setup was forwarded to researchers at the ERAU SHM and NDE Laboratory. Research efforts discussed in this thesis relate to the final OBG test which extended from December 2012 until November 2013. In an effort to characterize the initiation of a crack from the seeded fault and early damage state crack propagation, analysis and results presented within this thesis pertain to an interval of testing which stretched from December 2012 until February 2013 and covers over 300,000 seconds, or approximately 83 hours of testing. This period of testing is referred to as the early damage state testing interval.

1.2.1 H-60 Overview

In 1965, the United States government submitted a request for proposal for a new rotary aircraft system which would replace the Huey. In 1976, Sikorsky won the contract and delivered the first Blackhawk aircraft, YUH-60, to the U.S. Army in October of 1978. To date, Sikorsky has delivered over 3000 variations of the Blackhawk aircraft serving in every branch of the U.S. military and over 30 foreign countries. [3]

1.2.2 Tail Gearbox Output Bevel Gear Specifics

The MH-60 Seahawk is shown below for reference purposes. [4]



Figure 1 – Sikorsky MH60 Seahawk [4]

The tail rotor power train runs longitudinally along the upper edge of the aircraft tail.

Figure 2 provides multiple close-up views of the OBG location.

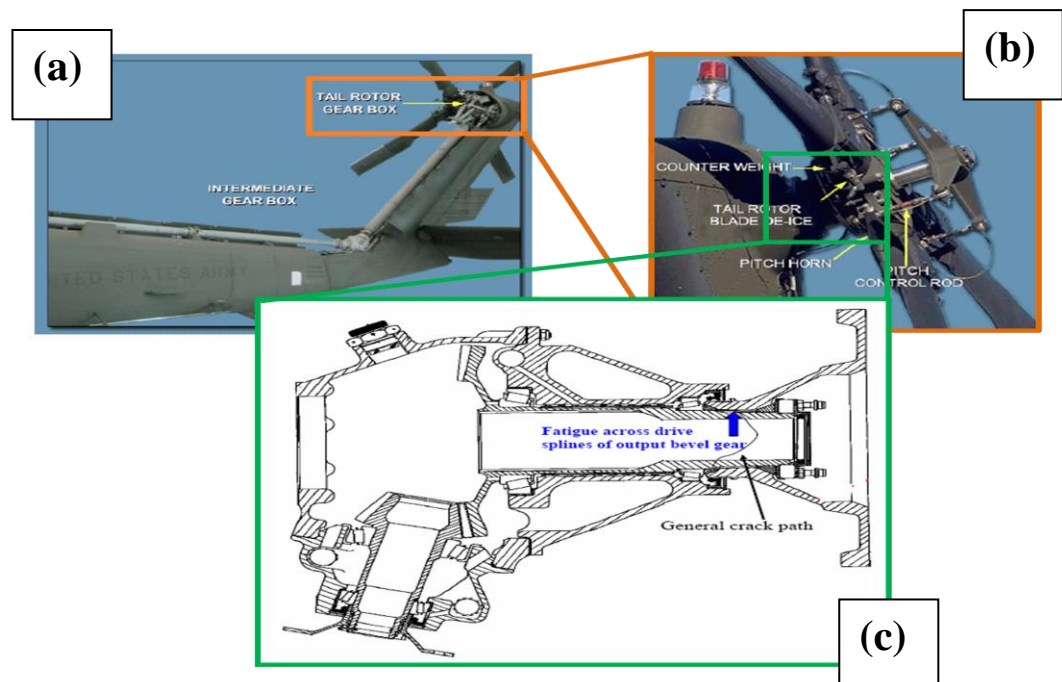


Figure 2 – (a) H60 Aircraft Tail [5] (b) H60 Tail Rotor [5] (c) H60 Tail Gearbox Schematic and Typical Crack Propagation Path [2]

1.2.3 Root Cause

The direct transmission of rotational energy from the TGB to the tail rotor produces a bi-loading scenario; tail rotor torque and hub bending moment. Past investigation has shown that the bending hub moment is the primary factor in circumferential crack propagation about the OBG splines [2].

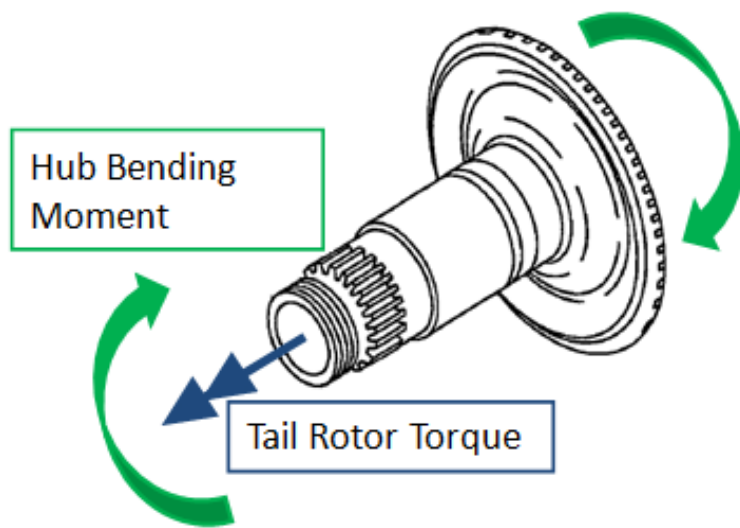


Figure 3 – OBG Schematic [2] and Bi-Loading Scenario

Additional investigation has recognized the presence of fretting corrosion of the silver-plate layer that coats the faces of the gear splines. Once this layer is removed, a higher contact stress between the gear splines is present due to interactions of dissimilar metals [2]. The presence of fretting corrosion leads to pitting wear and is predicted to be the root cause for crack initiation. Figure 4 shows fretting corrosion and pitting wear on the faces of adjacent splines on the OBG that was noted in 2011 H60 OBG testing. Regions where the silver plate material has been removed are indicated.

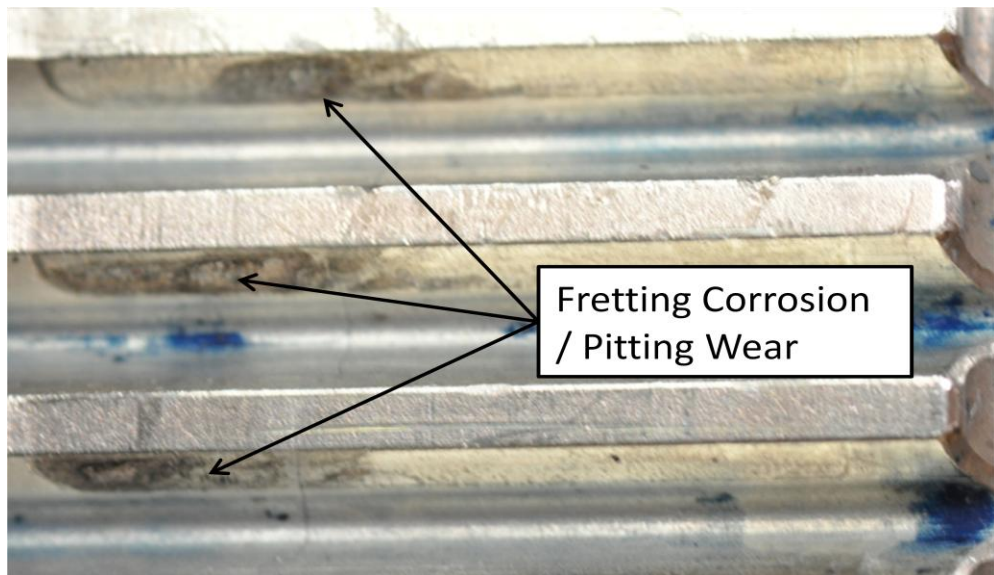


Figure 4 – Typical OBG Fretting Corrosion and Pitting Wear [6]

CHAPTER 2 – Principles of Acoustic Emission Non-Destructive Evaluation

2.1 Nondestructive Evaluation Overview

The American Society of Nondestructive Testing (ASNT) defines nondestructive testing (NDT) as, “the process of inspecting, testing, or evaluating materials, components or assemblies for discontinuities, or differences in characteristics without destroying the serviceability of the part or system” [7]. As opposed to destructive testing methods which are typically used to determine physical properties of a material, such as ductility, strength, and toughness, NDT methods primarily detect flaws and other differences in the characteristics of the material. The extensive list of various NDT procedures span a broad range of fields and include numerous applications throughout the lifetime of a part or system and assist in developing a higher quality product, reduce manufacturability and operability costs, and ensure safety to the public.

2.2 Other Nondestructive Testing Methods

There are thirteen established NDT methods used today. The six most frequently used test methods are Magnetic Particle Testing (MT), Liquid Penetrant Testing (PT), Radiographic Testing (RT), Ultrasonic Testing (UT), Electromagnetic Testing (ET), and Visual Testing (VT) [7]. Table 1 below briefly describes each method and summarizes the associated benefits and limitations. Acoustic Emission is detailed in the last row.

Table 1 – Description of Other NDT Methods [7]

NDT Method	Detection Objective	Advantages	Limitations
Magnetic Particle	Surface and slightly subsurface defects, cracks, seams, porosity, permeability variations	Indicates subsurface defects, relatively fast and low cost. Can be portable.	magnetic field alignment, demagnetization of parts after testing, cleaning prior to inspection, error due to surface coating
Liquid Penetrant	Defects open to surface: cracks, porosity, seams, labs, through wall leaks, etc	Low cost, portable, indications may be examined visually, results easily interpreted	Surface coats may prevent detection, cleaning required prior to inspection, detects must be open to surface
Radiographic	Internal defects and variations: porosity, inclusions, cracks, density variations, corrosion,	No couplant required, many ray source options, small ray sources can be placed in small openings, portable	Equipment can be costly, source decay, radiation hazards, large variation in ray sources
Ultrasonic	Internal defects and variations: porosity, inclusions, cracks, delaminations, texturing, general material properties	Most sensitive to cracks, immediate test results, portable, high penetration capability,	Couplant required, part geometry may be a limitation, manual inspection likely required
Electromagnetic	Cracks, crack depth, resistivity, corrosion	Portable, access to only once surface required	Edge effect, good surface contact required, difficult to automate, surface contaminations
Visual Testing	Cracks, corrosion	Inexpensive, immediate results, little to no equipment needed	Defects must be on surface and visible
Acoustic Emission	Crack initiation and growth rate, internal cracking, friction or wear, plastic deformation	Remote surveillance, dynamic detection, portable, source detection capabilities	Transducers only on surface, limitations with highly ductile materials, parts must be stressed, noise filtration required

2.3 Acoustic Emission

Acoustic emission may be defined as the transient elastic waves propagating through a material under stress which emanate from discrete locations of energy release [7]. AE sources can be attributed to internal sources such as plastic deformation and fatigue cracking as well as external sources such as mechanical or electrical noises. As a general rule, the parent material which would house a flaw is experiencing a load condition of some sort to instigate activity. A relatable example of an AE event would be the crack that is heard after breaking a stick. Though acoustic emission is inaudible to the human ear, acoustic emission testing (AET) equipment located on the surface of the material is capable of isolating and augmenting the wave energy. The digitized signal is parameterized and used to effectively distinguish between the presences of multiple sources of energy release.

2.3.1 History of Acoustic Emission Testing

The earliest known applications of acoustic emission phenomena date back to antiquity. Pottery makers would utilize the audible emissions indicative of fast or non-uniform clay drying to assess production quality [8]. Fuyuhiko Kishinouye was the first to submit a planned scientific report in 1933 characterizing the time distribution of earthquakes based on the acoustic emissions associated with wood fracture signals due to seismic activity. The 1930's witnessed a handful of other experiments which first detailed the results of AE activity within metallic specimens. Major efforts to correlate AE activity to deformation and fracture behavior were initiated in the 1950's and has continued to progress. Extensive applications of AET began in the mid-1990s [9]. AE is emerging as a

more well-established and reliable NDT technique, especially as instrumentation technology and methods are refined.

2.3.2 Acoustic Emission as a Nondestructive Testing Method

AET differs from other NDT methods in two ways. First, AET detects energy signals released from a material under in-service load conditions as opposed to other methods which require an energy input to the test specimen. Second, AE deals with dynamic changes within a material as opposed to static defects [9]. The numerous elastic, chemical, and free energy sources which may lead to the release of AE signals upon changes to the internal structure of a material allow AET to be a reliable NDT method to detect defect formation across a wide range of structures and material types. The nature of AE allows continuous monitoring of an in-service structure and defect detection in areas that are inaccessible using other NDT methods. Unfortunately, applications of AET methods are accompanied by a handful of limitations. Application of AET methods to large structures requires an array of sensors and data collection devices. Aside from sensor performance issues, AE sensors are sensitive to a variety of noise sources which may be present at the testing site. Typically, noise can be attributed to frictional, impact, or mechanical sources. Although noise does not prohibit AE NDT testing, it does further complicate the data collection and analysis process. Another important limitation of AET is irreversibility; if the material is loaded to a given stress level, unloaded, and reloaded, no emissions will be noted upon reloading unless the previous loading has been exceeded [10].

2.3.3 Acoustic Emission Structure Health Monitoring

AET as a SHM method is commonly implemented for damage detection in pressure vessels, piping systems, weld and corrosion monitoring, and many other systems. [9] Applications also exist within the aerospace industry. With an always aging fleet, aircraft SHM is an ever-present issue. As early as 1979, the Acoustic Crack Detection System (ACDS) was developed to monitor the in-flight structural integrity of a U.S. Air Force KC-135 aircraft [11]. In 1998, graduate students studied the acoustic sources present during in-flight monitoring of fatigue crack growth in the vertical tail section of a Cessna T-303 Crusader [12]. The AE NDT program at ERAU has since investigated the principles of AE as a SHM tool for various aircraft.

2.4 Acoustic Emission Data Acquisition

A basic AE test setup and sample output is displayed below.

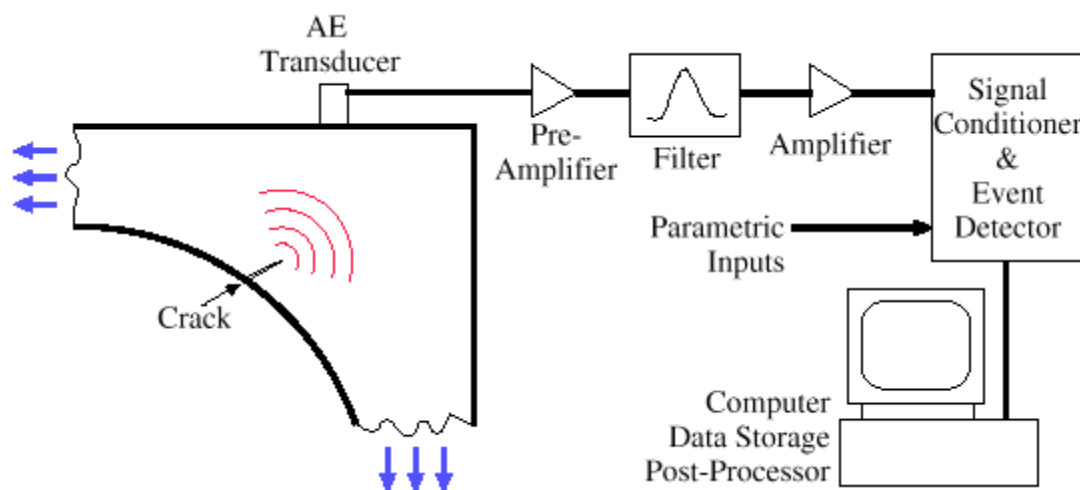


Figure 5 – Basic AE Test Setup [9]

2.4.1 AE Piezoelectric Transducers

As seen in Figure 5, the typical AET setup includes transducers, preamplifiers, filters, amplifiers, and a data acquisition system. Though all of these components are essential in AE data collection and analysis, the AE sensor captures and translates acoustic emissions into a digital form which can be evaluated experimentally and is the most vital element. A sample schematic for a typical AE transducer is shown in Figure 6.

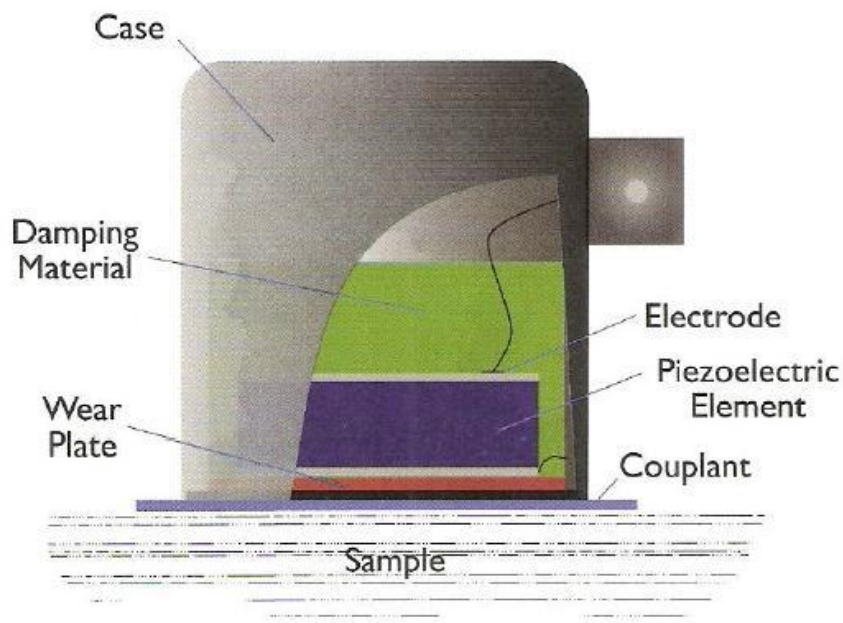


Figure 6 – AE Piezoelectric Transducer Schematic and Labeled Components [9]

A piezoelectric element with a set operating frequency range and damping material is housed within a metallic case. Emission signals emanate through the piezoelectric element and are converted into a voltage signal. The electrode connection transmits the digital AE event for amplification, filtering, and ultimately storage. The damping material prevents transmission of the acoustic event to other components in the AE system.

2.4.2 AE Signal Parameters

Figure 7 portrays a physical representation of a digital signal which would be stored as an AE event.

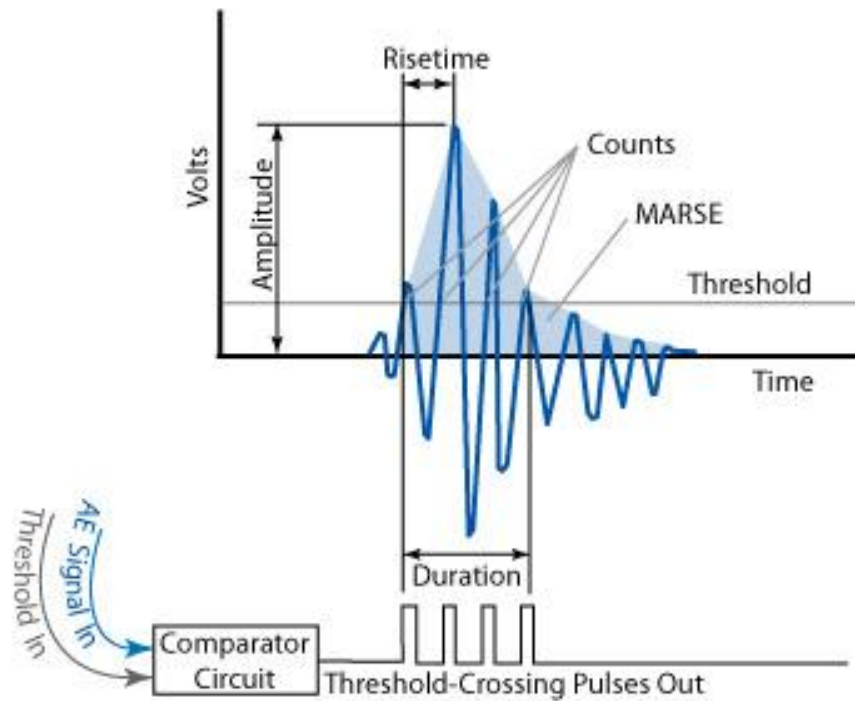


Figure 7 – Primary AE Signal Parameters [13]

The five primary signal parameters labeled in Figure 7 are described in Table 2.

Table 2 – Description of Primary AE Signal Parameters [13]

Signal Parameter	Description
Amplitude (dB)	Greatest measured voltage in a waveform in decibels. Signals with amplitudes below the minimum threshold will not be recorded.
Risetime (μs)	Time interval between the first threshold crossing and the signal peak.
Duration (μs)	Time difference between the first and last threshold crossings. Relies upon the magnitude of the signal and the acoustics of the material.
MARSE	Abbreviated for ‘Measured Area under the Rectified [linear voltage] Signal Envelope’. With units of Energy Counts (EC#) it is proportional to the energy of the event and is referred to as Energy.
Counts	Number of pulses emitted for each time the amplitude is greater than the threshold.

2.4.3 Layout File Parameters

Mistras’ AEWIn, an AE data acquisition and replay software, was used in the collection of all AE data throughout the course of this research. Within AEWIn, a layout file is created which provides the foundation for collection and analysis of raw AE data. The layout file allows the user to adjust various settings to further refine the recorded digital signal. Table 3 lists and defines the relevant layout file settings.

Table 3 – Description of Layout File Parameters

Layout File Parameter	Definition
Amplitude Threshold (dB)	Prime value that controls channel sensitivity. System will not record signal until the amplitude is greater than the threshold value.
Pre-amplifier Gain (dB)	Gain setting used in the amplification of the digital signal. Can be adjusted to allow the use of different pre-amplifiers
Lower Filter (Hz)	Lower boundary on operating frequency of the piezoelectric transducer
Upper Filter (Hz)	Upper boundary on operating frequency of the piezoelectric transducer
Sampling Rate (Samples Per Second)	Frequency at which sensor samples the test specimen
Peak Definition Time (PDT) (μs)	Timing setting parameter of signal measurement process to ensure correct identification of the signal peak for risetime and peak amplitude measurements
Hit Definition Time (HDT) (μs)	Timing setting parameter of signal measurement process to ensure each AE signal is reported as one and only one hit
Hit Lockout Time (HLT) (μs)	Timing setting parameter of signal measurement process to avoid spurious measurements during the signal decay.

CHAPTER 3 – Literature Review

3.1 Characteristics of Failure Mechanisms in Metal Specimens using AE Data

In order to characterize damage criterion for the H60 TGB OBG using acoustic emission, a basic understanding of failure mechanisms in metal specimens using AE data is required. The predominant failure mechanisms in metal specimens are plastic deformation and cracking. Plastic deformations are irreversible changes to the microscopic structure which occur at regions of higher stress concentrations for a specimen under loading. Sufficient plastic damage leads to the initiation of flaw [14]. With sufficient stress concentrations and/or load cycles, a crack will initiate from the flaw and continue to propagate. Three predominant modes of fatigue cracking exist [15]. Mode I, or plane strain, is identified by crack opening through a prying motion and is the most common mode of fatigue cracking of metallic specimens. Mode II corresponds to opposing faces of the crack surface sliding over each other in a perpendicular direction to the edge of the crack. Mode III, or plane stress, is identified by crack opening through a tearing motion. Figure 8 illustrates the three modes of failure.

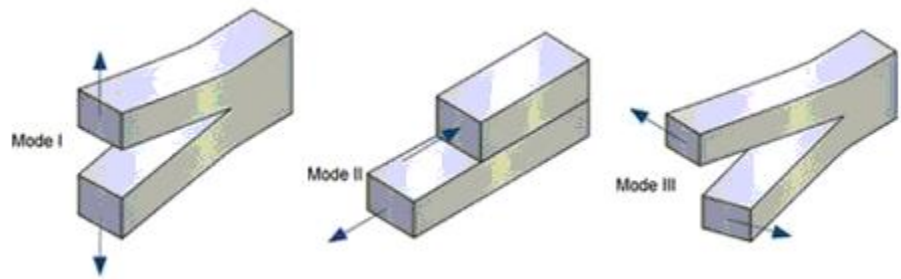


Figure 8 – Illustration of Predominant Fatigue Cracking Modes in Metallic Specimens [15]

Table 7 lists the characteristics of AE signals associated with failure mechanisms in metal materials. AE signals not relevant to cracking activity are referred to as noise signals and can typically be attributed to electric noise (environmental noises) and mechanical noise (rubbing or fretting noises) [1].

Table 4 – Characteristics of AE Parameters Associated with Failure Mechanisms in Metals [7]

Mechanism	Amplitude	Duration	Energy
Fatigue Cracking	High	Low to Medium	High
Plastic Deformation	Low	Short	Low
Noise	Low to Medium	Long	Medium

3.2 Prognostics and Health Assessment of Rotary Components

3.2.1 Notable Former Investigations

Other methods of fault detection and health monitoring of rotating machinery have been proposed. Al-Atat et al. [16] performed a comparative study of vibration signals emanating from a generic gearbox in operation. Time domain and frequency domain analysis of the signals were capable of distinguishing between healthy and damaged gear teeth. Numerous finite element studies have successfully modeled fatigue behavior in gear teeth. Jelaska et al. [17] utilized Franc2D software to model crack initiation and propagation in the root of a gear tooth. Results of the simulation were compared to fatigue crack behavior as predicted by the Coffin-Manson relationship and Paris' Law. Similarly, Abersek et al. [18], Spitas et al. [19] and Eriki et al. [20] separately developed theoretical models coupled with finite element analysis to determine the stress intensity factor (SIF) for edge cracks located at the root of gear teeth. Analytical methods were compared to experimental results. Numerical models were found to accurately predict crack path propagation up until assumptions used to develop the model were no longer valid. An example of this would be the presence of Mode II behavior for a conventional Mode I loading assumption.

3.2.2 ERAU Research Summary for 2010 and 2011 OBG Testing

As mentioned before, an AE data clustering and cluster verification algorithm developed at the ERAU SHM and NDE Lab by Shishino was incorporated in this research to identify the various AE source mechanisms present during testing and to distinguish between fatigue events and noise signals common to rotary component operation.

Shishino used AE data collected for various test dates within 2010-2011 and 2011-2012 H60 TGB OBG testing periods which exhibited significant cracking activity to further develop and refine the clustering algorithm. Shishino compared clustering attempts using an artificial neural network (ANN) or probabilistic models, different combinations of AE parameters as the input data, and a varying number of clusters. He further developed the algorithm by comparing the use of three separate mathematical models to verify the separation of the clusters. Shishino concluded his work by suggesting the Kohonen Self-Organizing Map (KSOM) ANN with energy, duration, amplitude, and average frequency as the input AE parameters. The specifics of the clustering algorithm are described in Section 5.5 of the thesis.

Figure 9 below is a sample AE plot developed by Shishino using energy, duration, amplitude, and average frequency as input AE parameters to the KSOM and five output clusters for 2010 testing data. A table accompanies the AE plot which classifies the source mechanism for each cluster via the corresponding color of the hits.

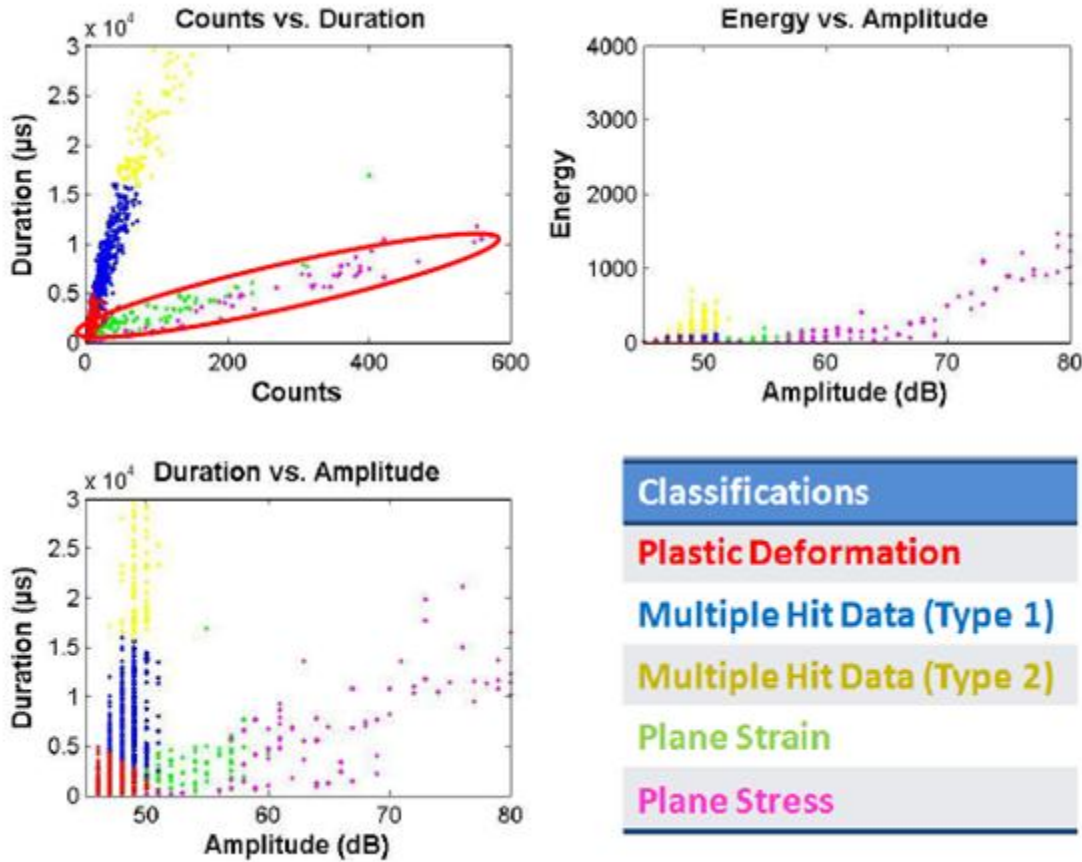


Figure 9 – Sample AE Plot from 2010 Testing [1]

The most notable observations in Figure 9 above are the two bands of hits in the duration versus counts subplot. The arithmetic value of counts divided by duration yields the average frequency. This is represented by the slope of data within the duration versus counts subplot. Past research at ERAU [21] [22] has shown that different clusters and source mechanisms can be characterized by the range of average frequency slopes. The first band consists of the blue and yellow clusters. The long duration and lower amplitude of these clusters is characteristic of noise signals. The second average frequency band is comprised of green and pink hits, circled in red, which exhibit shorter durations and higher amplitude and energy values; typical to cracking activity. Shishino concluded

these clusters corresponded to different cracking modes such as plane strain, or Mode I, and plane stress, or Mode II. The clustered AE plot in Figure 9 provides a baseline for noise signals and AE cracking behavior emanating from a crack propagating circumferentially about the OBG and served as the foundation for research efforts presented in this thesis.

3.2.3 AE Structural Health Monitoring of Helicopter Power Train Gearbox

Miller et al. [23] studied the AE response of crack growth in an SH-60 helicopter drive train in an effort to develop a data clustering method. Similar to the algorithm developed by Shishino at ERAU, Miller incorporated statistical analysis methods coupled with a classifier loosely based on the Kohonen SOM to successfully detect faults and damage in different helicopter drive train components. Furthermore, cracking activity was directly related to amplitude and energy of AE events; specifically a small number of very high amplitude and very high energy values early into testing which most likely correspond to crack initiation as multiple hairline cracks merge together. A phenomenon termed ‘pop-in’.

3.3 Acoustic Emission Crack Initiation of Cyclically Loaded Specimens

AE technology and data acquisition methods have proven to be a reliable means of detecting early signs of plastic deformation in crystalline metal and alloy structures which are likely to occur at the onset of crack nucleation [24]. Slip band formation and twinning are two forms of early plastic damage in which the atomic crystalline structure is rearranged. Slip bands are caused by the dislocation and sliding of adjacent crystal planes whereas twinning is the displacement of atoms in a fashion which still preserves coherent

structural boundaries [14]. In the propagation of an initiated flaw, bursts of AE activity are typically observed which occur sequentially until specimen failure. Figure 10 provides a sample log-log plot of the cumulative AE hit count versus cycles.

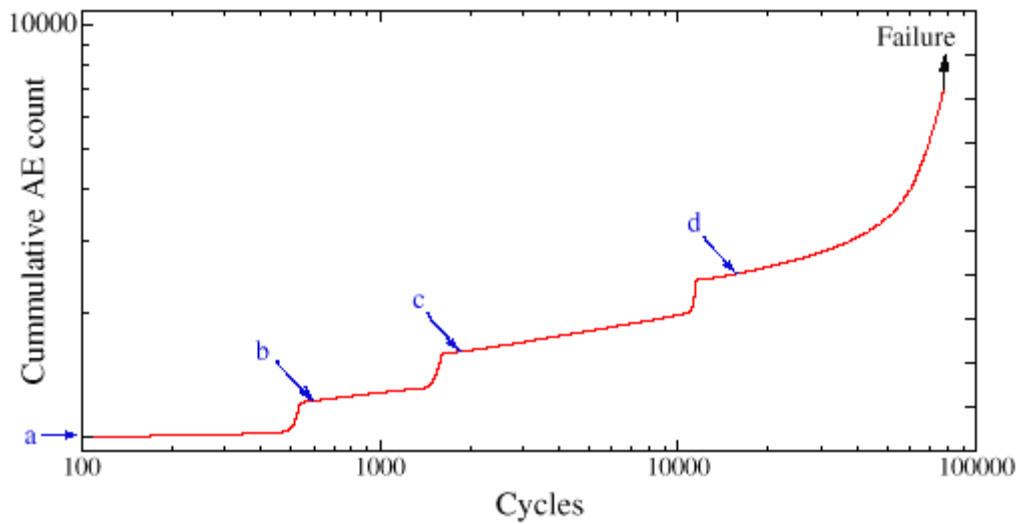


Figure 10 – Cumulative AE Hit Count Profile for Cyclically Loaded Specimens [24]

To provide additional insight into early damage state AE behavior, cumulative AE hit count profiles are developed using data recorded from the H60 TGB OBG early damage state testing interval.

3.4 Acoustic Emission as a Basis for Crack Growth Rate Models

Despite the successful application of AE principles to the domain of structural health monitoring, AE as a basis for crack growth rate models is far more complex yet offers benefits of obvious importance. The definition of acoustic emissions as transient elastic energy waves which propagate through a material under loading assumes the AE source to be an elastic event. This assumption lies within the branch of fracture mechanics

known as Linear Elastic Fracture Mechanics (LEFM). The theoretical LEFM cracking model can be used to compute a crack extension, Δa , based on Equation 1 [25].

$$\Delta a = \frac{U_e * E}{B * K_I^2} \quad \text{Eq. 1}$$

Where B is the specimen thickness, E is the modulus of elasticity, K_I is the mode I stress intensity factor, and U_e is the energy released by crack extension, plastic deformation, and fracture events within the plastic zone [26]. Equation 1 can be modified to account for additional loading scenarios such as cyclic loading and/or mixed mode fatigue.

In 1974, D.O. Harris and H.L. Dunegan of Dunegan/Endevco expanded Equation 1 to develop a theoretical model which correlated the energy released during crack extension to the energy of acoustic emission signal events [27]. Figure 11 displays a sample plot of their effort which corresponds to different metallic specimens.

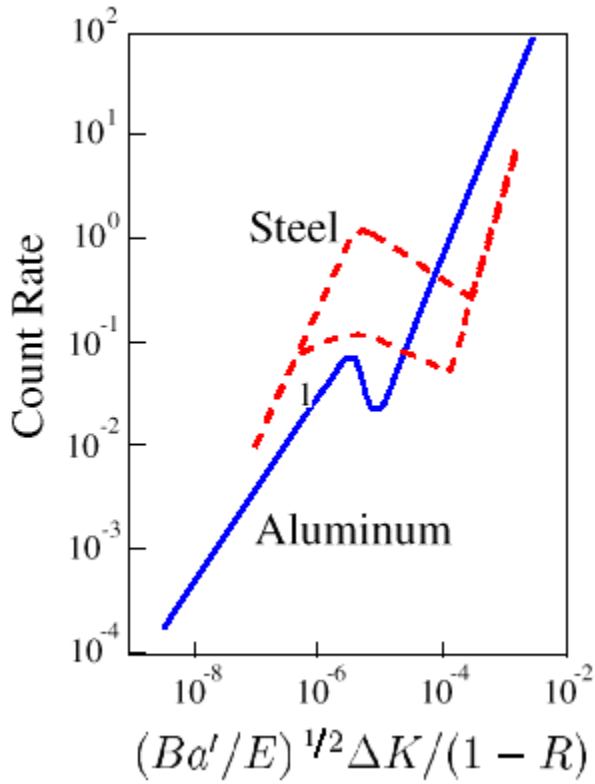


Figure 11 – Harris and Dunegan Relationship for Metallic Specimens [24]

Based on Figure 11, a Harris and Dunegan (H&D) relationship plots the rate at which AE hits occur to the following relationship on the log-log scale:

$$\sqrt{\dot{U}_E} = \sqrt{\left(\frac{B * a'}{E}\right)} \frac{\Delta K}{(1 - R)} \quad \text{Eq. 2}$$

Where \dot{U}_E is elastic energy released per cycle, B is the specimen thickness, a' is the crack growth rate per cycle, E is the modulus of elasticity, delta K is the stress intensity factor range, and R is the load ratio. Evidently, the plot consists of three regions: a log-log linear relationship, two peaks, and a second log-log linear relationship with a steeper slope than the first. H&D theorized that the peaks region corresponds to a transition between predominant failure modes as cracking progresses.

H&D were likely the first to detect a discernible relationship between AE energy levels to fatigue source energy. They further theorized the existence of a proportionality constant, not easily determined, which scaled AE energy to source energy. The complexity of determining a model which ties AE energy to source energy is two-fold. First, the energy levels recorded by AE sensors are logged under a reference unit and are proportional to true source energy. Berlinsky of the National Institute of Standards and Technology (NIST) conducted a two-pronged approach to calibrate AE sensor response to elastic energy transfer of a ball drop collision and a laser impingement. The results of his experiment revealed a power law relationship which accurately relates AE energy to elastic energy. Second, the complex interaction between elastic energy release rate and plastic zone energy absorption greatly affects AE sensor response [28]. The more ductile the material, the more energy is absorbed by the plastic zone resulting in a smaller remnant elastic energy portion which reaches the AE sensor. Figure 12 depicts representations of the amount of source energy which is recorded by the sensor between ductile and brittle materials. The discrepancy between AE event energy and true source energy is a segment of quantitative AE NDE which has been under review for quite some time.

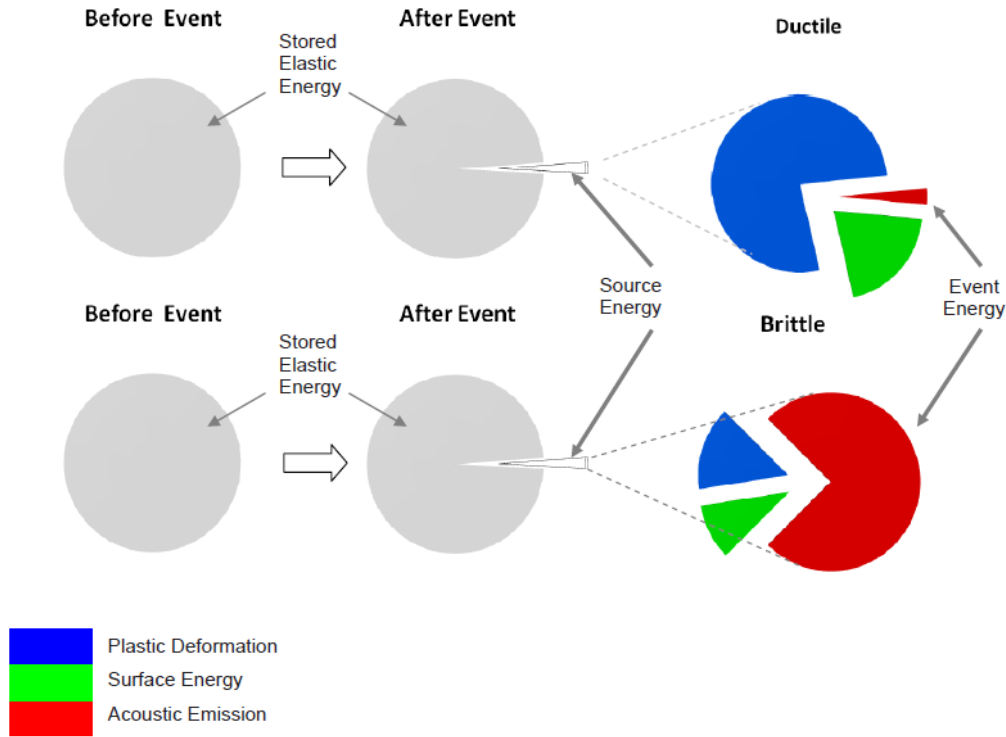


Figure 12 – Energy Conversions between Source Energy and AE Event Energy [28]

Harris also studied the significance and development of energy in AET [29]; efforts which have long since contributed to the evolution of AE energy, other AE parameters, and AE data collection principles as a whole. Supplementary research has stemmed from Harris and Dunegan's first model. Lindley et al. [30], Berkovitis et al. [31] and Roberts et al. [32] found similar relationships between AE hit rate, crack growth rate, and stress intensity factor. Power-law expressions were commonly found to relate AE data to LEFM parameters. Yu et al. [33] developed a model to estimate crack extension and residual service life of steel bridge components. Similar to Paris' law, the model is of the form:

$$\Delta a = \beta(\Delta U)^\alpha \quad \text{Eq. 3}$$

Where β and α are material constant boundary conditions dependent upon the specimen material/geometry and loading conditions.

3.5 Gearbox and Rotating Machinery Overview

By definition, the function of a gear drive is to reliably transmit torque and rotary motion between a prime mover and a driven piece of equipment at acceptable levels of noise, vibration, and temperature. [34]. The complex interactions of gear teeth meshing, shaft alignment issues, and other mechanical intricacies of gearbox operation provide for a difficult problem to analyze; specifically within the domain of damage detection.

3.5.1 Gear Failure Modes

Table 5 outlines the four major categories for gear distress and failure modes.

Table 5 – Description of Gear Distress and Failure Modes [34]

Failure Mode	Description
Pitting	Surface fatigue due to localized areas of high stress typically corresponding to uneven material surfaces.
Wear	Loss of material from the contacting surface of a gear.
Plastic Flow	Surface deformation resulting from the yielding of the gear tooth surface and subsurface material.
Breakage	Fracture of gear teeth originating from propagation of fatigue cracks source from high stress bending loads.

The differences in the four modes result from variations in physical characteristics and properties of the gears as well as residual stress characteristics associated with the surface hardened gearing.

CHAPTER 4 – H60 Tail Rotor Gearbox Experimental Setup

4.1 Ground Test Stand

To replicate the bi-loading scenario produced by the direct transmission of rotational energy from the H60 TGB OBG to the tail rotor during in-flight conditions, Navair engineers designed and assembled a ground test stand located in Patuxtent River, MD. Various combinations of hub moment and torque load conditions were applied throughout testing to ultimately generate a flaw at the seeded fault which propagated circumferentially about the OBG splines. A 3D representation of the ground test stand can be seen in Figure 13 below.

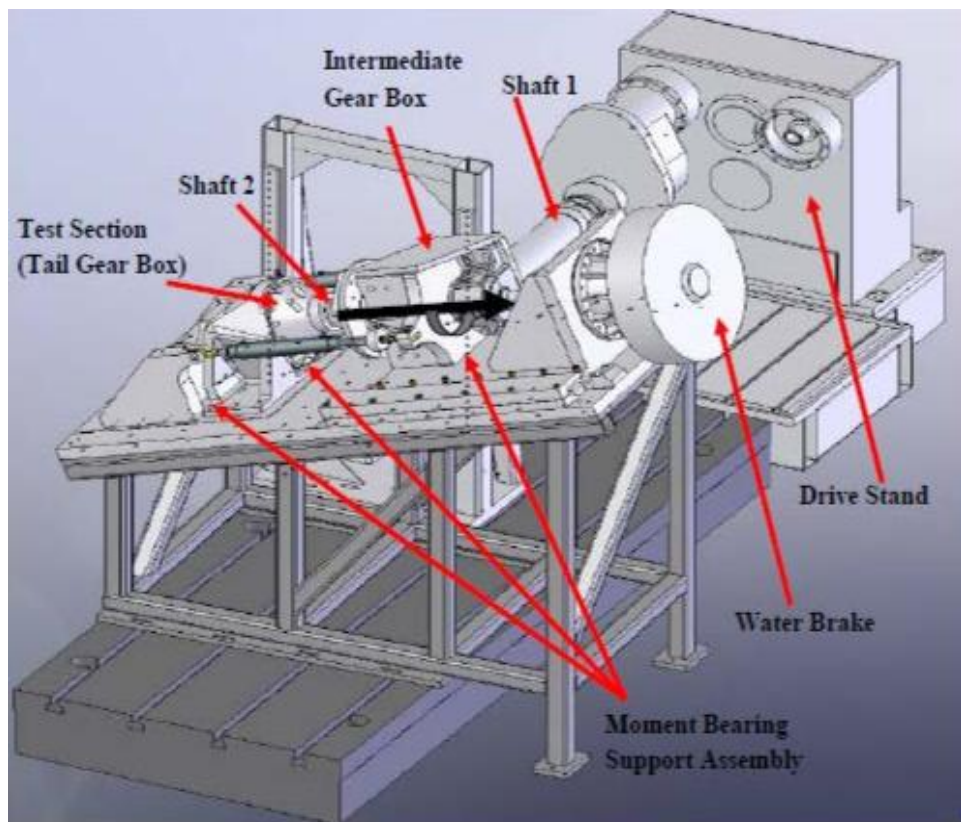


Figure 13 – H60 Tail Gearbox Ground Test Stand [2]

The ground test stand is driven by an Avtron model K938 motor rated up to 500 HP and dual 15000/30000 RPM settings. A Moment Bearing Support Assembly (MBSA) designed by Navair engineers is incorporated in the test setup and is capable of supplying thrust loads up to 2,000 lbs and moment loads up to 70,000 in-lbs. The MBSA is also capable of alternating between clockwise and counter-clockwise hub moments to further simulate in-flight load conditions. A Kahn Model 301-220 water brake is fitted in-line with the gearbox and MBSA shafts to absorb the load and distribute the heat generated by the setup [2].

4.2 Load Conditions and Testing Procedure

A testing procedure was established to simulate the variation of load conditions the H60 OBG would witness during service. Each test point included a pre-determined testing time, application of a clockwise (CW) or counterclockwise (CCW) moment, and a specified load condition. Table 6 outlines the various test points and corresponding test dates within the early damage state testing interval.

Table 6 – Early Damage Testing Interval Test Points

Test Points	Test Date	Time (minutes)	Load Condition	Moment
1	12/14/2012	480	4	CCW
2	12/19/2012	960	4	CW
3	12/20/2012	65	5	CCW
4	01/02/2013	40	6	CW
5	01/03/2013	130	2	CCW
6	01/10/2013	120	2	CW
7	01/11/2013	65	4	CCW
8	01/14/2013	35	5	CW
9	01/16/2013	20	6	CCW
10	01/25/2013	255	1	CW
11	01/28/2013	210	1	CCW
12	01/29/2013	65	2	CW
13	02/05/2013	45	4	CCW
14	02/06/2013	35	5	CW
15	02/07/2013	20	6	CCW
16	02/11/2013	255	1	CW
17	02/12/2013	210	1	CCW

The torque and hub moment combinations which correspond to the six separate load conditions are detailed in Table 7.

Table 7 – Load Conditions

Load Condition	0	1	2	3	4	5	6
Torque (in-lb)	7912	7912	7912	6130	8704	6331	8530
Hub Bending Moment (in-lb)	0	20000	30000	35508	43318	50292	61799

Prior to operating the gearbox at each test point, a start up procedure was followed. First, the gearbox was operated at 750-1250 in-lb until the oil sump temperature reached ~145

°F. At this time, no bending or thrust loads were applied. Next, a simple procedure was followed before and after the application of each test point. This procedure is listed in Table 8.

Table 8 – Test Point Operating Procedure

Step	Thrust/Lift Load (lbs)	Duration (minutes)
1	500	5
2	1,000	5
3	2,000	5
4	Conduct Test Point	
5	2,000	5
6	1,000	5
7	500	5

The hub moment and torque loading profiles for the cumulative early damage state testing interval are plotted in Figure 14 and Figure 15.

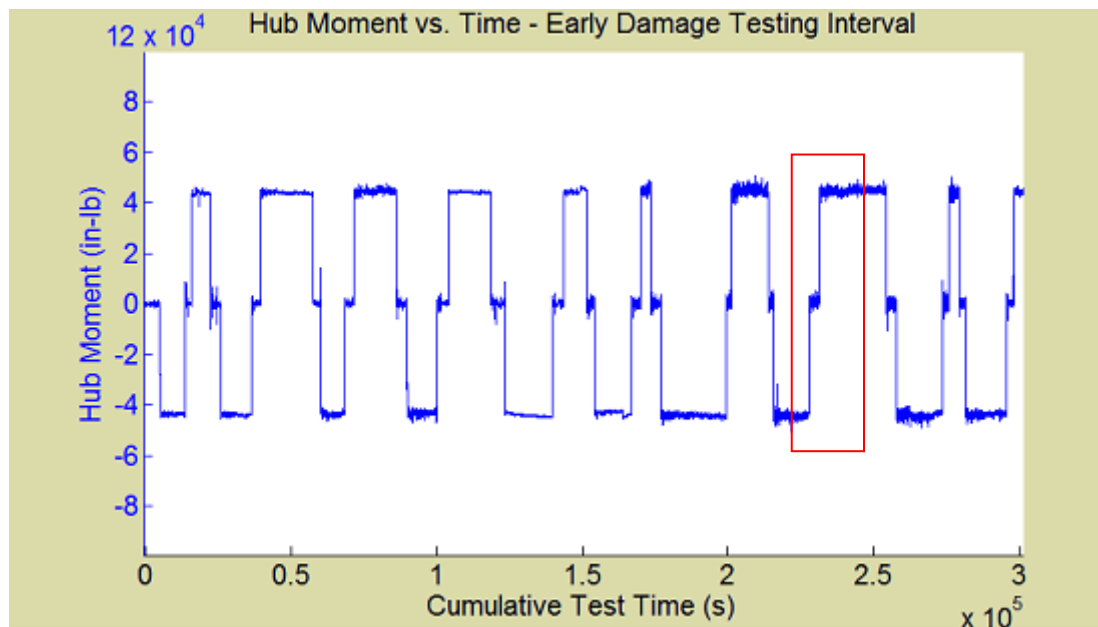


Figure 14 – Cumulative Early Damage Testing Interval Hub Moment Load Profile

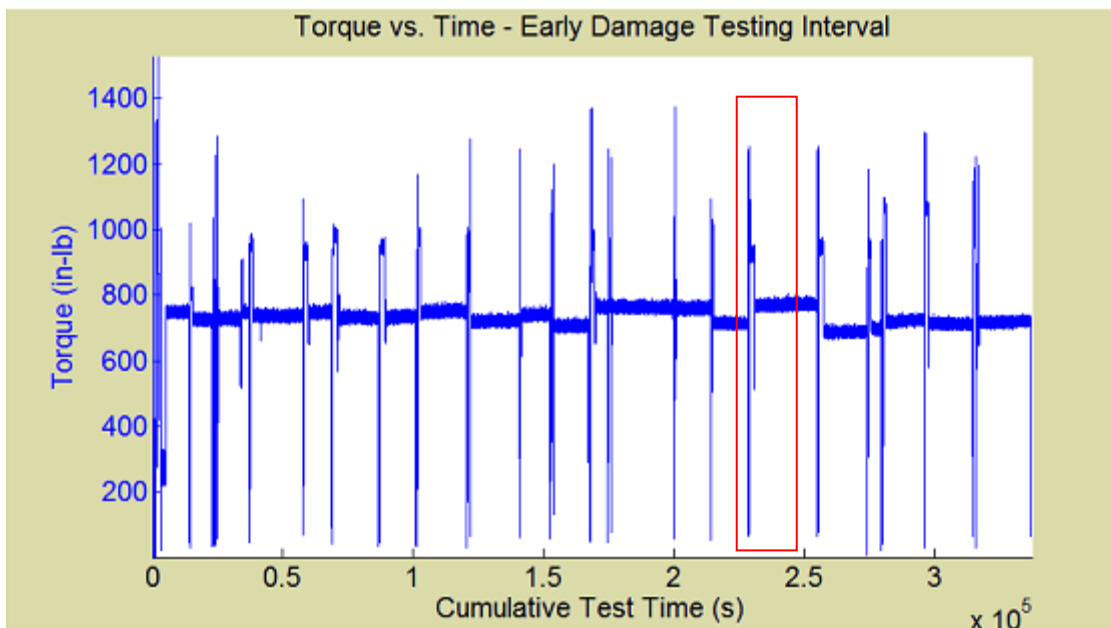


Figure 15 - Cumulative Early Damage Testing Interval Tail Rotor Torque Load Profile

The red boxes in Figures 14 and 15 correspond to a single test point and are expanded in Figures 16 and 17 to provide a supplementary view of a typical loading profile for a single test point.

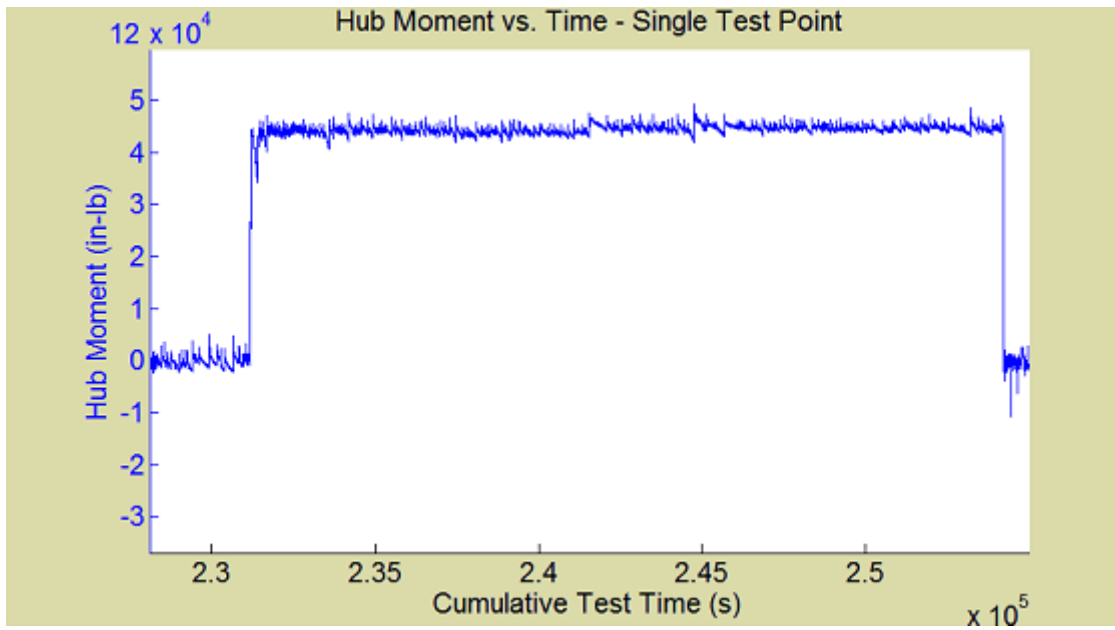


Figure 16 – Single Test Point Hub Moment Profile

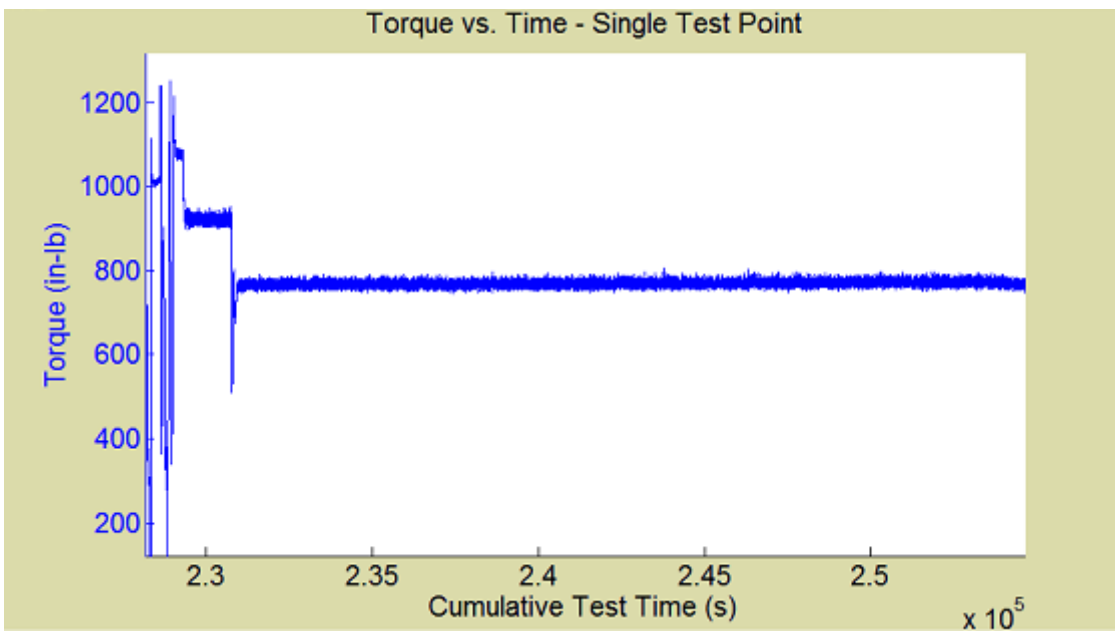


Figure 17 – Single Test Point Tail Rotor Torque Profile

4.3 Electro-Discharge Machined Notch

A fault was seeded into the OBG by implementing an EDM notch in the root-to-tip direction of the gear tooth face. EDM notch methodology employs the use of an electrode to machine the desired shape into a work piece [35]. In this case, the EDM notch removes the layer of silver-plate which coats the surface of the gear teeth and replicates the high contact stresses that may be present between the inherent gear materials once pitting damage has removed the coated layer. The EDM notch, per Sikorsky recommendations, is located on the face of the OBG spline located adjacent to the key way slot, 0.711 inches from the end of the spline. Extending in the tooth root-to-tip direction, the notch was 0.0009 inches wide, 0.0101 inches deep and 0.0249 inches long [2]. Figure 18 portrays the notch location with respect to a CAD model of the OBG.

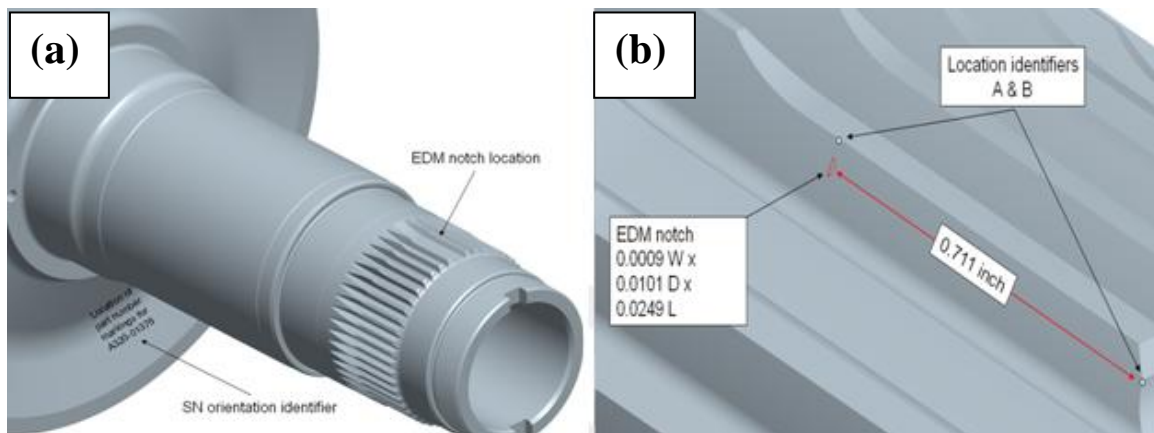


Figure 18 – OBG 3D Model with (a) Notch Location and (b) Notch Dimensions [2]

4.4 AE Data Collection

4.4.1 Data Acquisition and PZT Transducer Locations

A dual pronged approach was taken in the collection of H60 TGB OBG AE data. Six Navair transducers were connected to a PAC Micro II PCI AE data acquisition system [36] and four ERAU transducers were connected to a PAC μ DiSP / NB-8 AE data acquisition system [37]. Both systems were equipped with Mistras' AEWin software package. Navair AE sensors included three PAC WD transducers [38] and three Micro-30s transducers [39]. ERAU AE sensors consisted of four R15i transducers [40]. Figure 19 shows physical locations of the ten sensors with respect to the gearbox.

NAVAIR AE Sensors

- CH PAC WD
- CH PAC Micro-30s

ERAU AE Sensors

- CH R15I

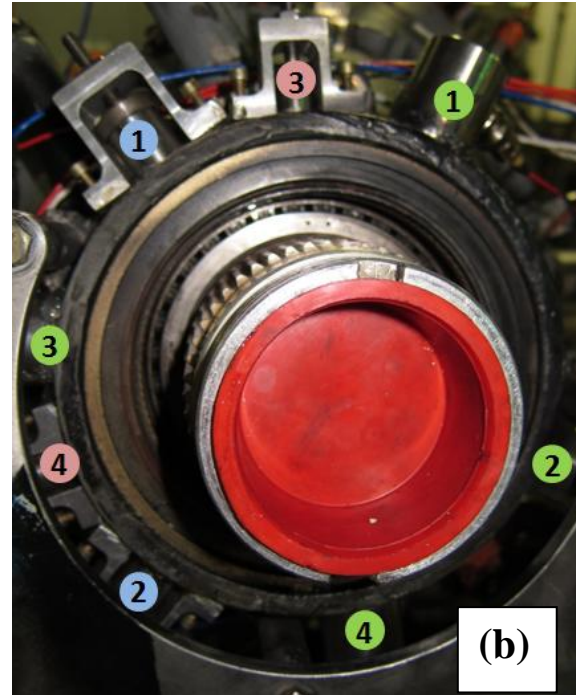
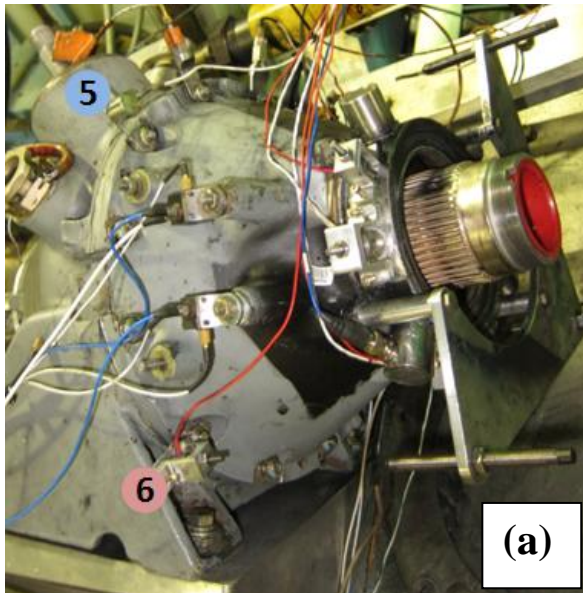


Figure 19 – AE Transducer Locations

Four of the six Navair sensors and all four ERAU sensors were secured along the outer ring of the bevel gear housing. The two remaining Navair sensors were secured to the main gearbox housing flange. All Navair AE sensors were coupled on surface with Dow Corning vacuum grease and mounted via aluminum brackets. All ERAU AE sensors were mounted onto the surface with hot glue.

4.4.2 Layout File Parameters

Generally, layout file settings were uniform for all channels with the exception of the amplitude threshold. The amplitude threshold serves as an automated filtration method during testing. If the digital signal produced by the piezoelectric conversion does not have signal amplitude greater than the threshold value, the signal features are not saved. A higher amplitude threshold eliminates noise sources which exhibit lower amplitude values than AE signals which correspond to fatigue activity. Increasing the amplitude threshold, however, potentially risks not recording valuable data such as the AE signals sourced to plastic damage and/or micro-cracking activity which would be present in the early damage state. Table 9 lists the amplitude threshold settings for each channel sensor.

Table 9 – Navair and ERAU Sensor Amplitude Threshold Settings

Navair Sensors		ERAU Sensors	
Channel (Sensor Type)	Amplitude Threshold (dB)	Channel (Sensor Type)	Amplitude Threshold (dB)
Ch1 (WD)	61	Ch1 (R15i)	45
Ch2 (WD)	52	Ch2 (R15i)	45
Ch3 (Micro 30s)	72	Ch3 (R15i)	45
Ch4 (Micro 30s)	70	Ch4 (R15i)	45
Ch2 (WD)	54		
Ch3 (Micro 30s)	57		

Table 10 lists the remainder of the layout file parameters which were uniformly set for each channel.

Table 10 – Layout File Settings Common To Navair and ERAU Sensors

Layout File Parameter	Setting
Pre-amplifier Gain	40 dB
Lower Filter	100 kHz
Upper Filter	1 MHz
Sampling Rate	2 MSPS
PDT	200 μ s
HDT	800 μ s
HLT	1000 μ s

CHAPTER 5 – Data Analysis and Research Methodologies

5.1 Summary of Collected AE Data

At the end of each test point, the AE data acquisition system saves all of the hits recorded by each channel to a single AE data, or .DTA, file. Table 11 compares the .DTA file sizes, in megabytes (MB), recorded by each set of sensors for the different test dates within the early damage testing interval. The numbers in this table represent raw, unfiltered data.

Table 11 – AE Data File Size Comparison between ERAU and Navair Sensors

Early Damage Testing Interval Test Date	ERAU Sensor Set .DTA File Size (MB)	Navair Sensor Set .DTA File Size (MB)
12/14/2012	6133	11.50
12/19/2012	4169	13.19
12/20/2012	2743	7.84
01/02/2013	5311	11.86
01/03/2013	4285	15.82
01/10/2013	2535	8.90
01/11/2013	399	17.46
01/14/2013	1084	9.28
01/16/2013	303	12.27
01/25/2013	4674	10.50
01/28/2013	2137	20.60
01/29/2013	2293	13.30
02/05/2013	511	11.37
02/06/2013	6828	21.04
02/07/2013	1735	15.04
02/11/2013	3437	10.89
02/12/2013	1763	15.42

Given the difference in amplitude thresholds and transducer types between the Navair and ERAU data sets, the number of hits and size of the .DTA files varied significantly. Generally, all ERAU sensors recorded millions of more hits than the Navair sensors and in most cases; ERAU sensors recorded multiple .DTA files worth of data for a single test date.

5.2 Data Analysis and Research Methodology Flow Chart

AE data collected from Navair and ERAU transducers was processed and analyzed to characterize early damage state detection criterion. Specific channels were selected from each data set to ensure analysis efforts were focused on sensor data which recorded sufficient and appropriate AE activity relevant to the early damage state activity emanating from the EDM notch. Prior to clustering and further analysis, pre-processing and filtering procedures were necessary to remove AE hits which were confidently declared as being sourced to noise signals. Excessive noise signals affect the capability of the ANN to detect patterns in the data sets. Though the data processing steps were similar for Navair and ERAU data sets, each required a distinct logical course of thought and action. The flow chart in Figure 20 provides a visual description of the data analysis sequence. Each step in the flow chart and applicable justifications are further described in the following sections.

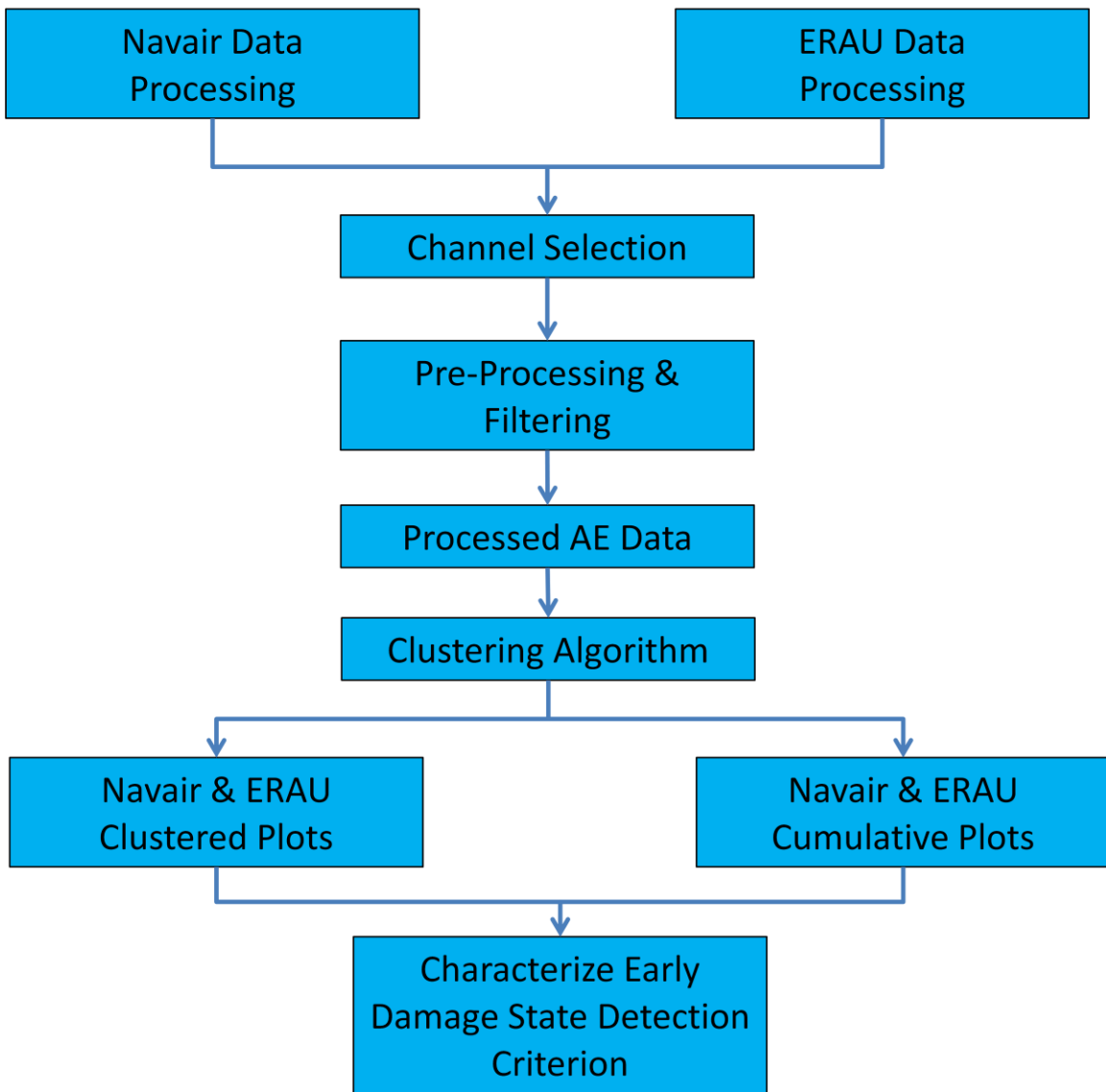


Figure 20 – Data Processing and Analysis Methodology Flowchart

5.3 Navair AE Sensor Data Processing

5.3.1 Navair Channel Selection

Though AE cracking signals are known to exhibit high amplitude and high energy, early state cracking and plastic deformation sources can still be present at relatively lower amplitude and energy values. [23] The first sign of flaw initiation from the EDM notch was observed on 12/14/2012. Navair Channel 3 and Channel 4 sensors which had amplitude thresholds of 72 dB and 70 dB, respectively, did not record any data on 12/14/2012, 12/19/2012, and 12/20/2012. Therefore, it was concluded that the amplitude thresholds of Channel 3 and Channel 4 sensors were too high to assess the first signs of early damage state AE activity. Unlike Channel 1 – Channel 4 sensors which were located on the outer ring of the OBG, Channel 5 and Channel 6 sensors were located on the gearbox housing flange and were not considered so that early damage initiation and propagation could be characterized for data recorded from sensors located as close as possible to the seeded fault.

Given the effort to determine the first signs of early state damage, Channel 1 and Channel 2 data were selected for clustering and further analysis for two reasons. First, the lower amplitude threshold values for Channel 1 and Channel 2 of 61 dB and 52 dB, respectively, were noted to record significantly more hits during the first three days of testing than Channel 3 and Channel 4 sensors. Second, Channel 1 and Channel 2 sensors were in close proximity to the EDM notch, as opposed to Channel 5 and Channel 6 sensors.

5.3.2 Navair Data Pre-processing and Filtering

One main purpose of data processing is to remove hits which can be confidently declared as noise. Figure 21 displays a side-by-side comparison of duration versus amplitude clustered plots for sample 2010 and sample 2013 OBG AE data.

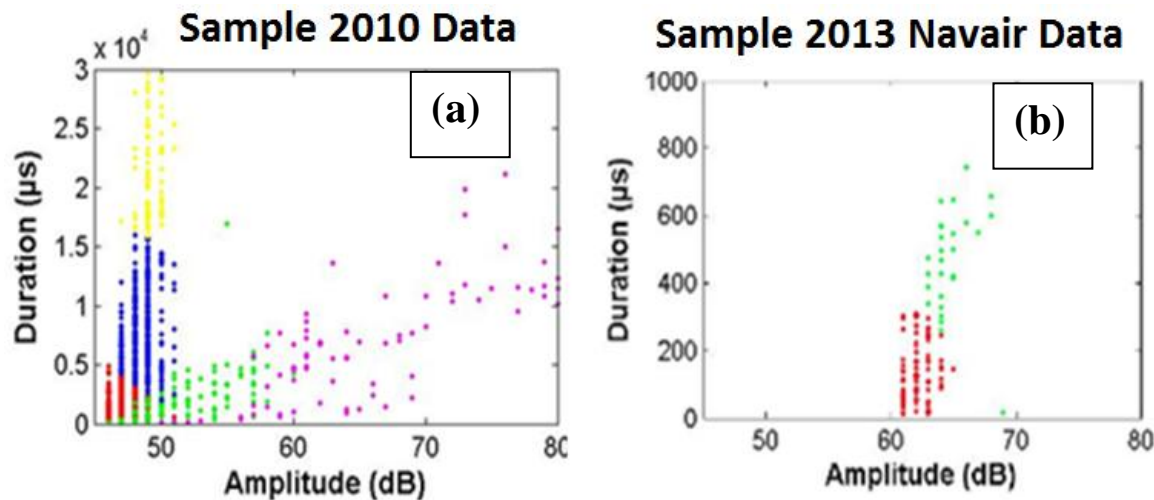


Figure 21 – Side-by-side Comparison of AE Plots for (a) 2010 H60 AE data versus (b) 2013 H60 AE data

It can be seen from Figure 21(a) that the noise signals represented by the blue and yellow clusters in the 2010 data are all enveloped with AE amplitude values less than ~52 dB. Considering the fact that with marginally higher threshold values, large quantities of noise signals would not have been recorded therefore limiting the amount of necessary preprocessing. More importantly, however, the increased amplitude thresholds risked not recording potentially valuable early damage state activity which may be present at lower amplitude thresholds. Therefore, a limited amount of processing was performed for Navair sensor data.

H60 OBG AE research conducted in 2010 conservatively concluded that data sets could be processed by removing hits with duration values greater than 100,000 μ s to remove any hits that are guaranteed to be sourced to noise signals and zero-value hits could be eliminated [1]. After data collection, analog signals are converted into digital signals. Signal features with values less than 0.5 are rounded to zero [1]. These are referred to as zero-value hits and do not represent significant AE activity. Furthermore, zero-value hits disrupt patterns in the data which may be detected by the ANN.

Figure 22 displays a sample data excerpt in which zero-value hits were recorded.

Time of Hit	AE Counts	Abs. Energy	Duration	Amplitude	Avg. Frequency
7696.017702	1	16.501137	0	61	0
7706.783068	6	2254.1377	44	64	136
7707.391478	1	2254.1377	0	61	0
7708.098195	1	2254.1377	0	61	0
7786.445515	1	254.49565	5	62	200
7811.010944	1	32.575504	0	62	0
7812.931721	2	1298.9877	42	62	48
7813.63841	3	1042.4928	19	63	158
7833.301591	1	14.84014	0	61	0
7834.514608	2	612.1972	19	62	105
7836.4861	1	612.1972	0	61	0
7836.587153	1	612.1972	0	61	0
7836.688213	1	14.85876	0	61	0

Figure 22 – Sample Data Excerpt with Zero-value Hits

For Navair AE sensor data, zero-value hits were eliminated from the data sets. As seen in Figure 21(b), every hit in the data set had duration values less than 1,000 μ s; thus a duration filter was not necessary.

5.4 ERAU AE Sensor Data Processing

5.4.1 ERAU Channel Selection

As seen in Figure 21(a), previous research using AE data collected from the OBG has revealed cracking clusters to be in the form of a band of hits with low duration and medium amplitude values. Figures 22 through 25 display a duration versus counts plot for a sample test date which exhibited a noticeable amount of relevant activity. Each plot focuses on hits with durations less than 10,000 μs to further emphasize the cracking signals. The supposed cracking cluster is highlighted in red for Channel 1 through Channel 3.

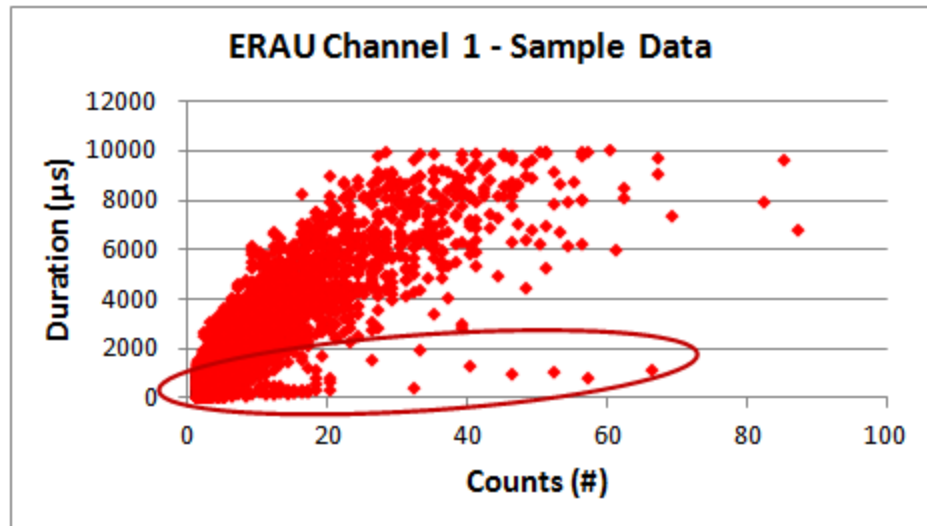


Figure 23 – Duration versus Counts plot for Sample ERAU Channel 1 Data

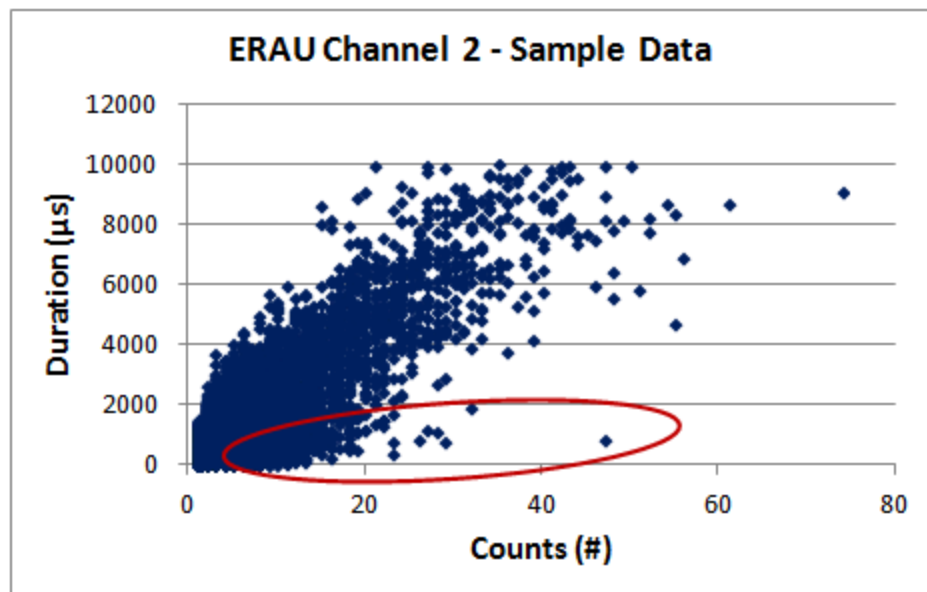


Figure 24 - Duration versus Counts plot for Sample ERAU Channel 2 Data

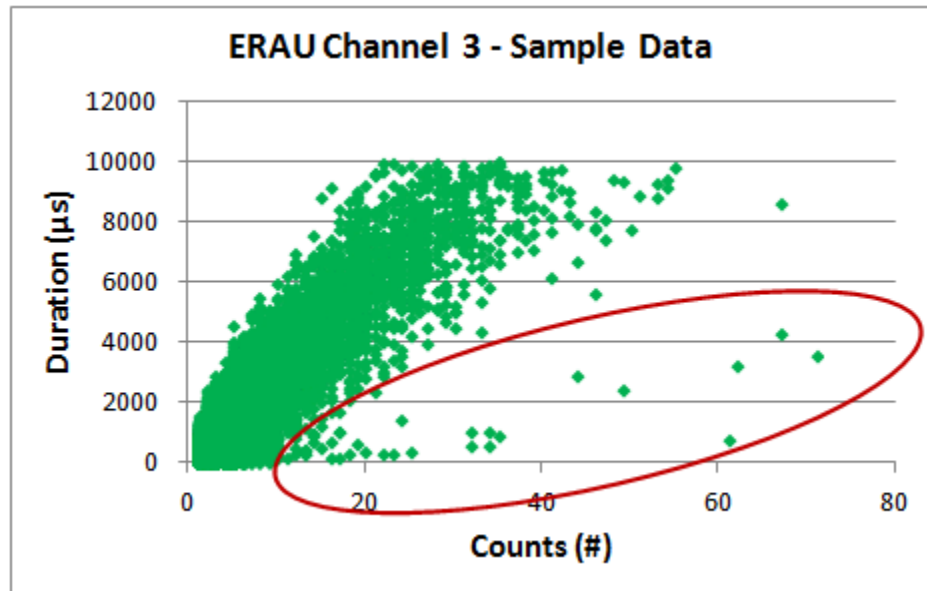


Figure 25 - Duration versus Counts plot for Sample ERAU Channel 3 Data

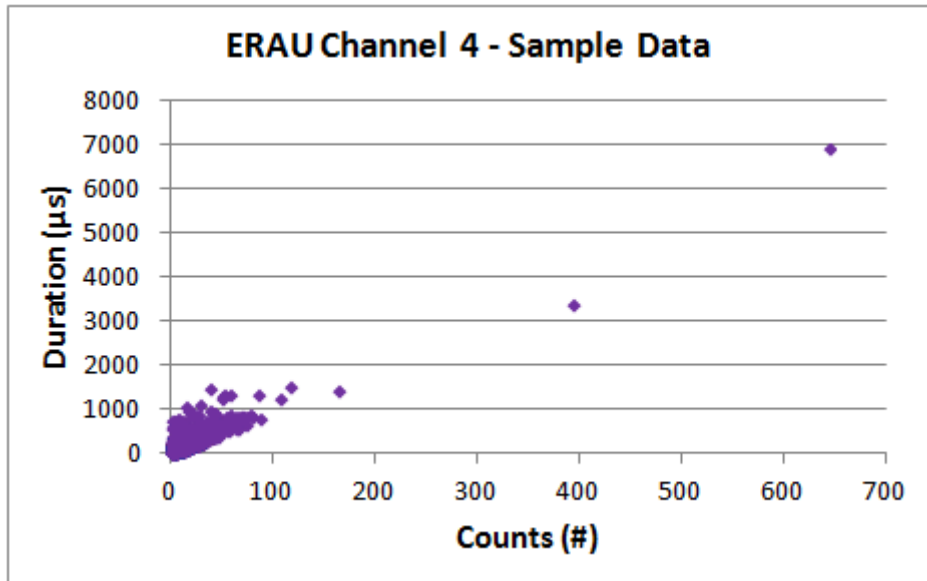


Figure 26 - Duration versus Counts plot for Sample ERAU Channel 4 Data

The number of hits enclosed within the red ellipses is on the order of approximately 50 to 100 hits for each of the channels. The total number of hits shown for each channel in Figures 23 through 26 is detailed in Table 12.

Table 12 – Summary of Number of Hits in Figure 23 through Figure 26

Sensor Channel	Number of Hits
Ch1	10,185
Ch2	54,263
Ch3	32,614
Ch4	15,750

Given the fact that Channel 4 did not record any hits with durations greater than 2,000 μ s, and does not resemble the form of Channel 1-Channel 3 data, it was excluded from the analysis. Although Channel 1 – Channel 3 sensors recorded a similar amount of hits within the cracking cluster, Channel 2 and Channel 3 were far more susceptible to noise. The large difference in the amount of noise signals compared to cracking signals for Channel 2 and Channel 3 data prevented successful clustering of the data. Instead of distinguishing between cracking signals and non-cracking signals, the small number of cracking signals were identified by the clustering algorithm as outliers to the noise clusters. Only clustering attempts using ERAU sensor Channel 1 data proved successful. Therefore only ERAU sensor Channel 1 AE data was considered for further analysis.

5.4.2 ERAU Data Pre-Processing and Filtering

Figure 27 consists of raw AE data recorded by ERAU sensor Channel 1 for a sample test date and is used to provide insight into why ERAU sensor .DTA files are orders of magnitude larger than Navair sensor .DTA files.

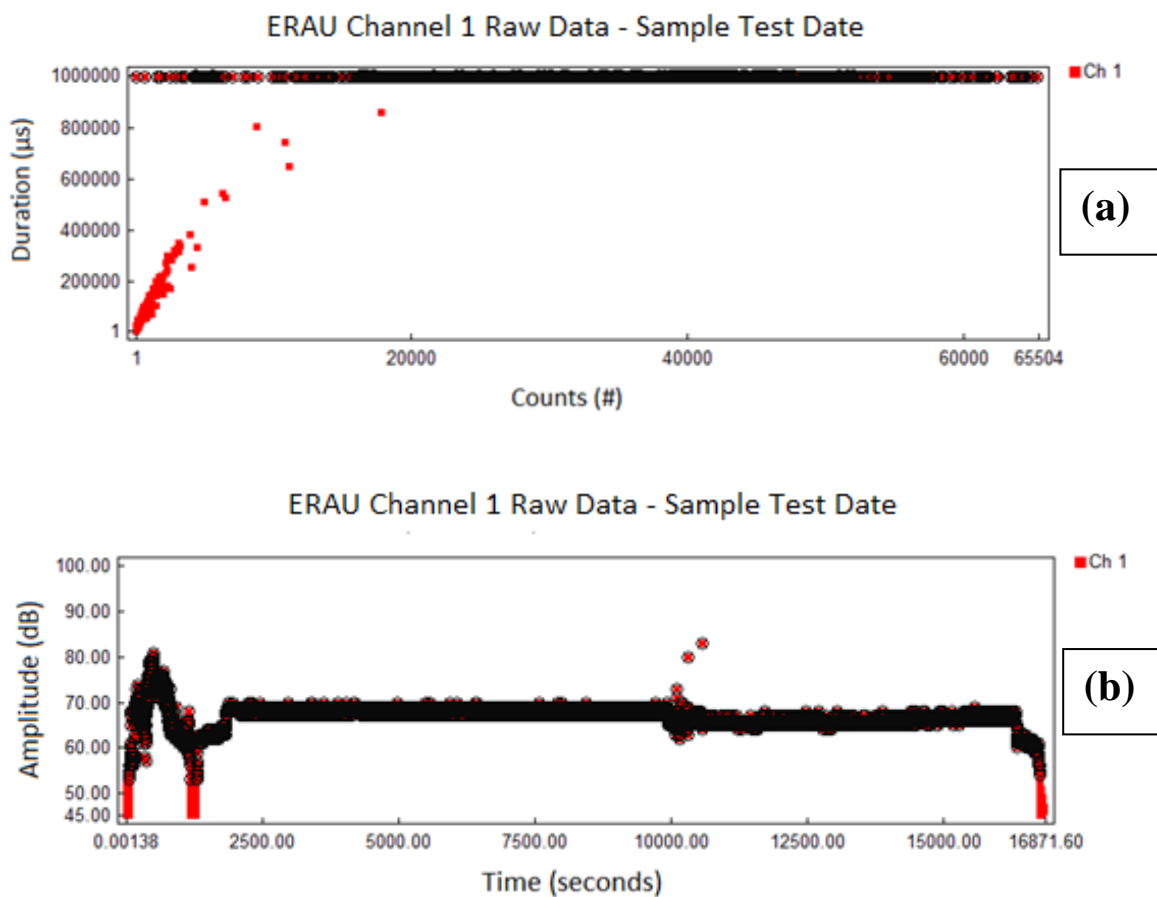


Figure 27 – (a) Duration versus Counts and (b) Amplitude versus Time plots of Raw ERAU Channel 1 Data for a Sample Test Date

Figure 27 incorporates a feature of Mistras' Noesis AE data post-processing software that links selected hits between separate graphs created using the same data. As seen in Figure 27(a), all hits with duration values greater than 1,000,000 μ s are selected. As a result,

almost all the hits in Figure 27(b) are highlighted and therefore have duration values of 1,000,000 μ s. The 1,000,000 μ s value corresponds to a duration limit within the AE data acquisition system. Any hits recorded with duration values greater than 1,000,000 μ s are still recorded but logged as having the maximum duration value.

Based upon the data in Figures 23 through 26 which were used for ERAU sensor channel selection, relevant cracking activity, enclosed by the red ellipses, coincides with a band of hits with duration values less than 10,000 μ s. This observation matches the AE behavior for cracking activity during 2010 H60 OBG testing and also proves that the hits with duration values of 1,000,000 μ s in the 2013 ERAU sensor Channel 1 data can be attributed to noise sources. The lessons learned from research conducted in 2010 were followed; hits with durations greater than 100,000 μ s and zero-value hits were filtered out of the ERAU sensor Channel 1 data sets.

AEWin's *Data File Filter* was used to create filtered .DTA files which only contained hits with signal feature values greater than zero, and duration values less than 100,000 μ s. If multiple .DTA files were recorded for each test date, AEWin's *Combine Data Files* utility was used to combine all of the filtered .DTA files into a single .DTA file which was processed and ready for analysis.

5.5 Data Clustering Algorithm

Processed Navair and ERAU data sets were analyzed to develop clustered plots. Clustered plots are produced by using an ANN to detect distinct patterns in the data sets and therefore provide insight into the source mechanisms of AE hit signals; namely to distinguish between cracking and non-cracking AE sources. Four AE signal parameters,

energy, duration, amplitude and average frequency, are considered. These were the four AE signal parameters, as suggested by Shishino in 2012, which yield the most appropriately clustered AE plots. For the scope of research efforts presented in this thesis, the AE energy signal parameter, Absolute Energy, was used as an alternative to the MARSE. Absolute Energy is the square of the digital voltage readings divided by a resistance value common to the impedance of the data acquisition device preamplifier. The parameter for Absolute Energy is recorded in units of atto-Joules (aJ) and more closely resembles the true energy of the AE event [41]. One aJ is equal to 10^{-18} J. A sample clustered AE plot with seven clusters is shown below. The AE plot consists of three subplots; AE counts versus duration, amplitude versus energy, and duration versus amplitude.

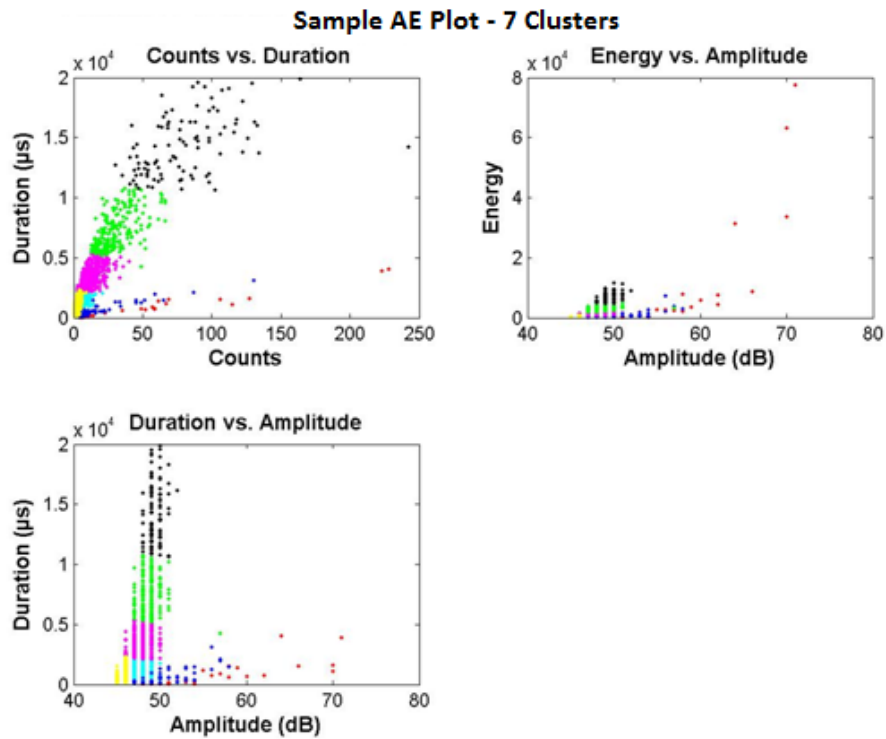


Figure 28 – Sample AE Plot for 2013 H60 AE Data Using Seven Clusters

Lessons learned from previous H60 TGB OBG research and the characteristics of failure mechanisms in metal specimens, as seen in Table 4, are used to determine the source mechanisms for each cluster. Table 4 is shown again as Table 7 below for convenience.

Table 13 - Characteristics of AE Parameters Associated with Failure Mechanisms in Metals [7]

Mechanism	Amplitude	Duration	Energy
Fatigue Cracking	Medium to High	Low to Medium	High
Plastic Deformation	Low	Short	Low
Noise	Low to Medium	Long	Medium

For the example shown in Figure 28, red and blue clusters exhibit lower duration values, medium to high amplitude and high energy values and represent cracking signals. Cyan, green, and black clusters consist of long duration and low amplitude values and correspond to noise. The yellow cluster is plastic deformation.

After data is recorded and processed, an extensive analysis method is executed with sensor data recorded during each test date. Once clustered AE plots have successfully been developed and verified for each test date, a general progression of the quantity and magnitude of the AE hits clustered as cracking events can be monitored.

5.5.1 Artificial Neural Networks

The objective of a clustered AE plot is to provide a graphical representation of the AE parameters classified by their source mechanism. The clustering algorithm satisfies this objective by organizing the output of an ANN. An artificial neural network is a mathematical algorithm that functions similar to the human brain. Multiple layers of processing elements (PE's), otherwise known as artificial neurons, are linked together using weight functions. The weight functions, which functionally resemble coefficients in an equation, can be trained to identify complex patterns within a data set. [22] In general, a network will consist of an input layer, one or more hidden layers, and an output layer. Data is presented to the network in the input layer, processed in the hidden layers and organized in the output layer [21].

To illustrate how ANNs work, consider the following analogy: When operating a vehicle, that driver must always be alert as a variety of stimuli is being perceived by the brain at any given instant. If a ball were to bounce across the street, the brain is responsible for linking the presence of that ball to the possibility of a child chasing after the ball. In this case, the brain has learned and detected a pattern similar to the way an ANN links AE hit events to each other based upon their signal characteristics. The ANN used in the ERAU algorithm is the Kohonen SOM.

5.5.2 Kohonen Self-Organizing Map

The Kohonen SOM, along with the input and output layers, is structurally comprised of a one-dimensional or two-dimensional hidden layer referred to as the Kohonen layer. The number of processing elements within the Kohonen layer represents the number of

possible classifications, or clusters, for the data set. All neurons within the Kohonen layer are not connected to another but are connected to each neuron within the input and output layers. Each connection has an associated weight. Mathematically, the SOM operates by minimizing the Euclidean distance between the weights and the input vectors for each PE in the Kohonen layer. [21] An intricate two-dimensional KSOM is represented in Figure 29.

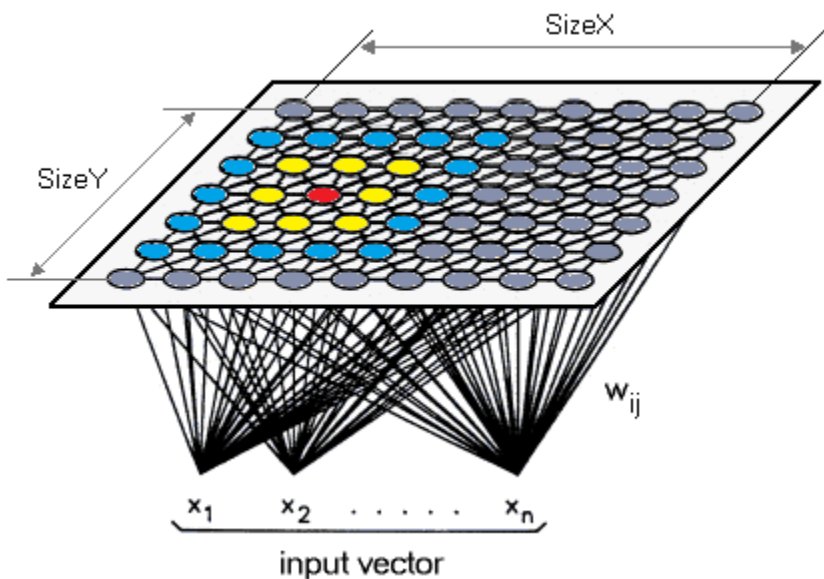


Figure 29 – Intricate Kohonen SOM [42]

For x_n neurons in the input layer, a Kohonen layer of SizeX by SizeY neurons processes the various parameters of the input vector. As input parameters are mapped to the Kohonen Layer, the weights of all connections are updated. The SOM iteratively updates neuron weights by determining a winning neuron noted by the red neuron in Figure 29. This approach in turn directly affects the weights of the yellow and blue neuron weights

in proximity of the winning neuron. The red, yellow, and blue neurons represent a neighborhood or cluster of mapped input parameters with like characteristics.

The KSOM incorporated in this research is far simpler. The network includes four input neurons to represent Absolute Energy, Duration, Amplitude, and Average Frequency AE signal parameters. Due to the high amplitude thresholds, only two neurons are set in the Kohonen layer. The objective is to distinguish between AE sources; namely noise, plastic deformation, and cracking. NeuralWorks Professional II/Plus, a pattern recognition ANN software, is used to construct the KSOM and analyze data. The output layer is a binary ‘yes/no’ output to indicate whether each input vector belongs to the specific neuron within the Kohonen Layer. A simple schematic of the aforementioned KSOM with two neurons in the Kohonen Layer is illustrated in Figure 30.

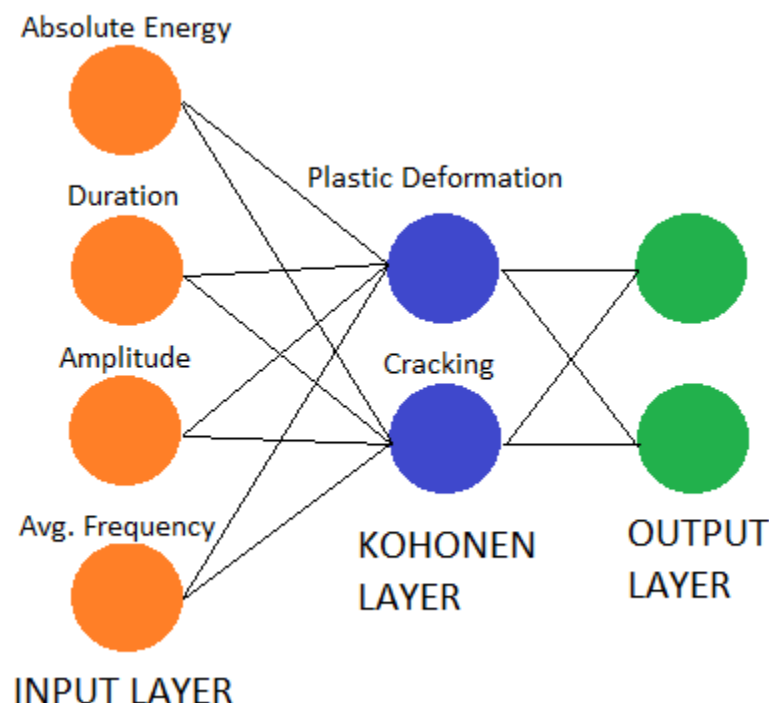


Figure 30 – Simplified Kohonen SOM Layout for 2013 H60 AE Analysis

A KSOM configuration as shown in Figure 30 would represent the ANN used to analyze most of the AE data collected by Navair sensors. The lower amplitude threshold of data collected by ERAU sensors and accompanied noise signals mandates more clusters for proper cluster separation. To determine the optimal number of clusters, visual inspection of each AE plot was performed in conjunction with a verification algorithm.

5.5.3 AE Plot Verification

A verification method ensures the appropriate number of clusters is used in the analysis of each test date. Suppose a user wishes to separate the data into clusters, the ANN will distinguish as many different patterns in the data as the number of selected clusters. It is the responsibility of the user, via verification algorithms and visual inspection of the AE plots, to determine the optimal number of clusters which properly separates the data. Figure 31 below is a side-by-side comparison of clustering results for sample duration versus counts subplot using three and four clusters. The band of hits designated to the blue cluster in Figure 31(b) was partially distributed between the red and blue clusters in Figure 31(a). That is, clustering with three clusters did not yield proper separation between the various sources.

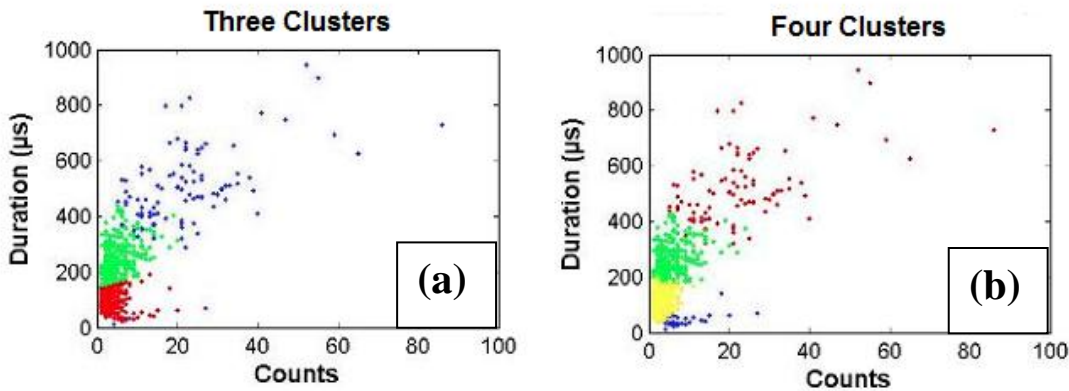


Figure 31 – Visual Inspection of a Sample AE Plot for (a) Three Clusters and (b) Four Clusters

The visual inspection procedure, as illustrated by Figure 31, can quickly assess the separation of potential cracking hits from other hits in the data set. As the user continues to increase the number of clusters beyond four, however, the blue cluster in Figure 31(b), or other clusters would become too separated. For this reason, a verification algorithm must be used in conjunction with visual inspection to determine the optimal number of clusters for each data set. The verification algorithm incorporates mathematical formulae to determine criterions which rate separation between the clusters. As the number of clusters is varied, the criterions can be plotted together and compared using a voting value. A larger voting value implies more successful clustering of the data. The three mathematical algorithms used are the Rij criterion, Silhouette criterion, and Tou criterion. For the same sample data set shown in Figure 31 above, a sample verification plot is shown in Figure 32 below which compares voting values for two, three, and four clusters.

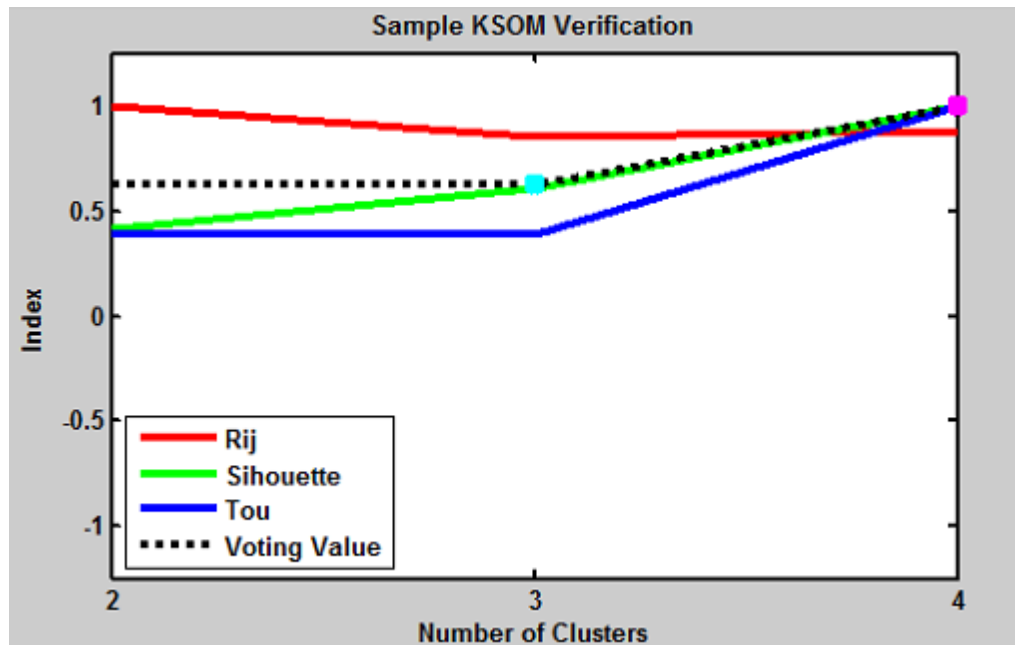


Figure 32 – Sample Verification Algorithm Output for Two, Three, and Four Clusters

The highest voting value, and thus optimal number of clusters, is found to be four. This matches the results of the sample visual inspection. Throughout the course of this research, visual inspection was used in conjunction with the verification algorithm to develop accurately separated clustered AE plots.

5.6 Approach for Early Damage State AE Data Behavior Characterization

5.6.1 Clustered Plot Inspection

The primary objective of clustered AE plot inspection is to distinguish AE events which are likely to correspond to cracking activity and characterize the signal parameters which correspond to these events. This operates hand-in-hand with the underlying objective of any AE data analysis method. The quantity and AE parameter magnitudes of the cracking

cluster can be monitored as testing progresses. Similarities and differences between Navair and ERAU sensor data are discussed.

5.6.2 Cumulative Plot Inspection

The development of cumulative test time plots, most notably; the log-log plot of cumulative AE hit count versus cumulative test time provides an additional approach of interpreting AE data. As seen in Figure 10, a sequence of jumps in the cumulative AE hit count throughout cyclic loading is observed followed by a seemingly exponential increase until the specimen fails. Cumulative AE hit count versus test time plots for the 12/14/2012 through 02/12/2013 early damage state testing interval were developed to further characterize early damage state detection criterion.

CHAPTER 6 - Results

6.1 Early Damage State Replica Cross Section

The early damage state testing interval extends to a point after testing began such that a crack had initiated from both ends of the EDM notch. Figure 33 below is a cross-sectional view of a molded replica taken from the OBG. The figures include a red line which corresponds to the surface length of the crack and multiple hash marks which indicate the crack front at different replicas molded throughout the early damage state testing interval. Note the grey material is the replica mold material. The white portion would correspond to the OBG geometry. All replica cross section views were provided by Navair engineers.

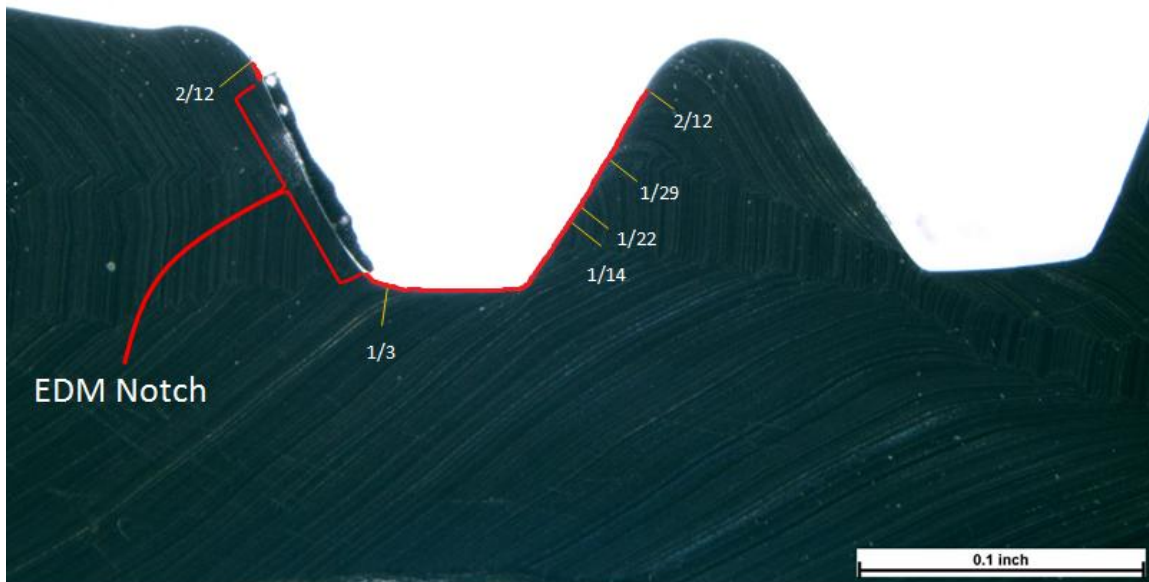


Figure 33 – Early Damage Testing Interval Replica Cross Section

As of February 12, 2013, the crack had initiated on both ends of the EDM notch and thus corresponds to the end of the early damage state testing interval.

6.2 Navair Data Clustered Plots Results

Navair sensor Channel 1 and sensor Channel 2 clustered AE plots for selected test dates from the early damage testing interval are presented in this section to display crack initiation from the EDM notch and/or early state crack propagation. Due to the higher thresholds, a limited amount of data is present for many of the test dates, specifically for the first few days of testing. Most of the plots in this section were analyzed using two clusters to either distinguish between cracking hits and non-cracking hits. Note the value ranges on plot axes differs between test dates. This is to provide a proper scale of the data points within each plot. Arrows are used to point out stand-alone data points which may not be easily visible. All Navair Channel 1 and Channel 2 clustered AE plots, in chronological order; can be found in the Appendix.

6.2.1 Channel 1 Clustered AE Plots

The Navair sensor Channel 1, 12/14/2012 clustered AE Plot is shown in Figure 34.

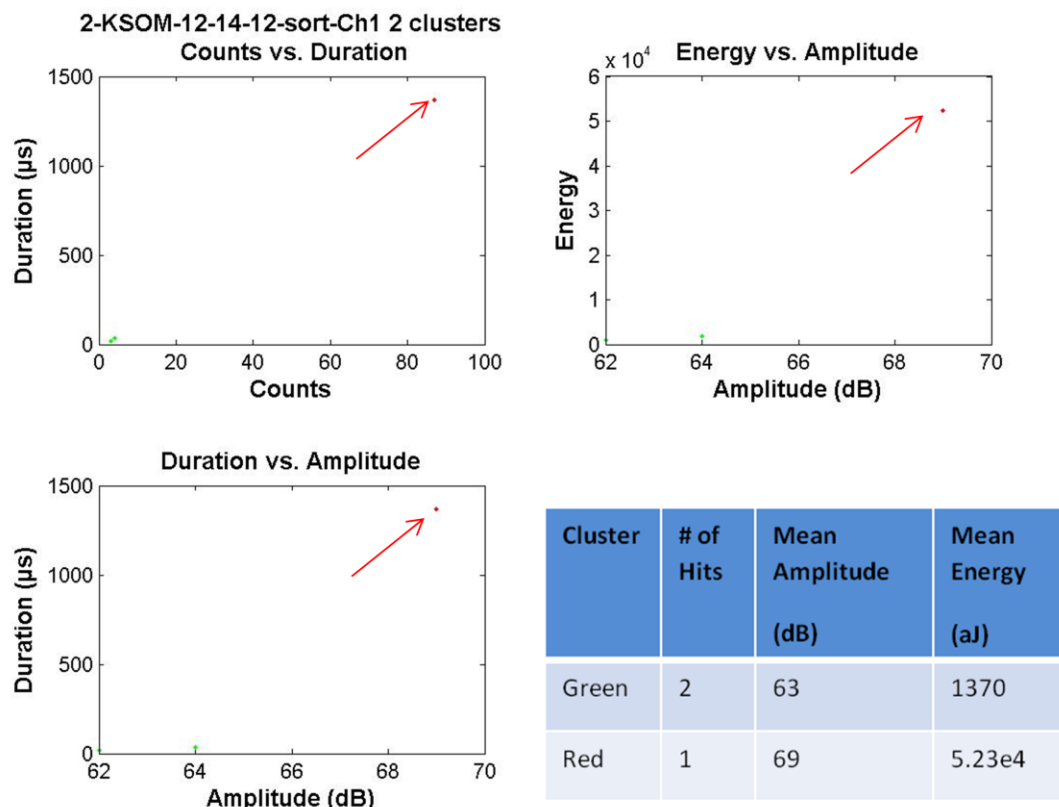


Figure 34 – Clustered AE Plot for 12/14/2012 Navair Sensor Channel 1 Data

The 12/14/2012 Navair sensor Channel 1 data recorded a total of three AE hits with one having a significantly larger energy and amplitude values than the other two. The difference in AE parameters between the one red hit and the two green hits was detected by the ANN. 12/14/2012, the first testing date, displays the first signs of crack initiation at End A of the EDM notch tip. As noted by Miller et al. [23], the high energy hits resemble the ‘pop-in’ of a microcrack emerging from the regions of larger stress concentration at the EDM notch tips.

The Navair sensor Channel 1, 01/11/2013 clustered AE Plot is shown in Figure 35.

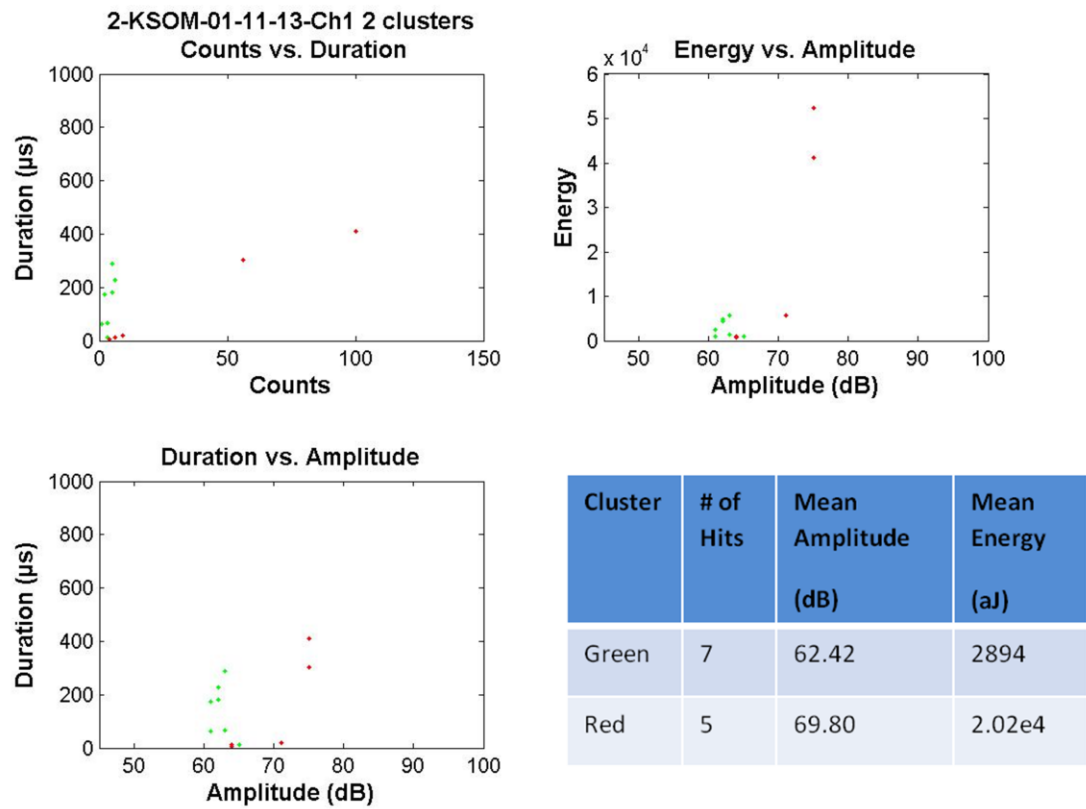


Figure 35 - Clustered AE Plot for 01/11/2013 Navair Sensor Channel 1 Data

Following a period of inactivity on 12/19/2012 and 12/20/2012 testing, AE behavior similar to that of 12/14/2012 data was observed for 01/02/2013 and 01/03/2013 test dates. Following limited activity on 01/10/2013, the 01/11/2013 AE plot indicates similar behavior as previous test dates while also demonstrating an increase in the quantity of hits and amplitude levels which were designated to the red cluster. Though the mean energy of the red cluster is of the same order of magnitude as the mean energy of the red cluster for the 12/14/2012 data, three hits display amplitude values greater than 70 dB.

The Navair sensor Channel 1, 01/14/2013 clustered AE Plot is shown in Figure 36.

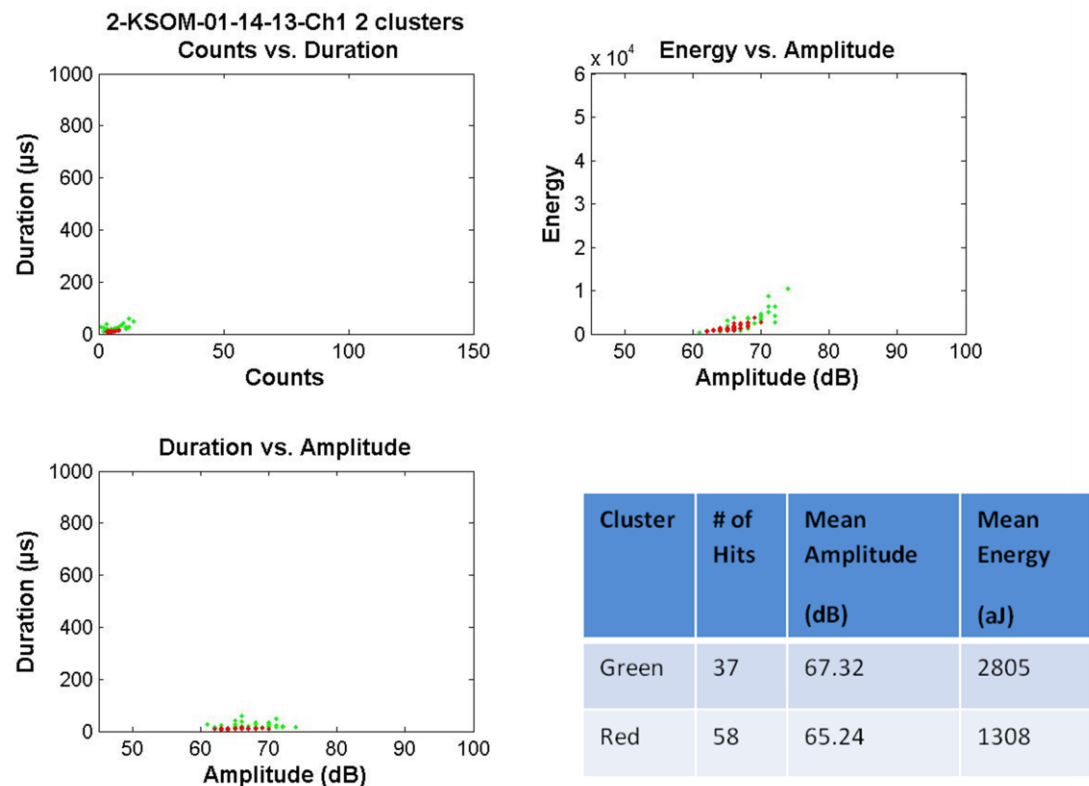


Figure 36 - Clustered AE Plot for 01/14/2013 Navair Sensor Channel 1 Data

Unlike previous test dates which indicate fewer hits but exhibit higher energy levels, the 01/14/2013 AE plot displays a burst of total activity which generally features lower energy levels.

The Navair sensor Channel 1, 01/28/2013 clustered AE Plot is shown in Figure 37.

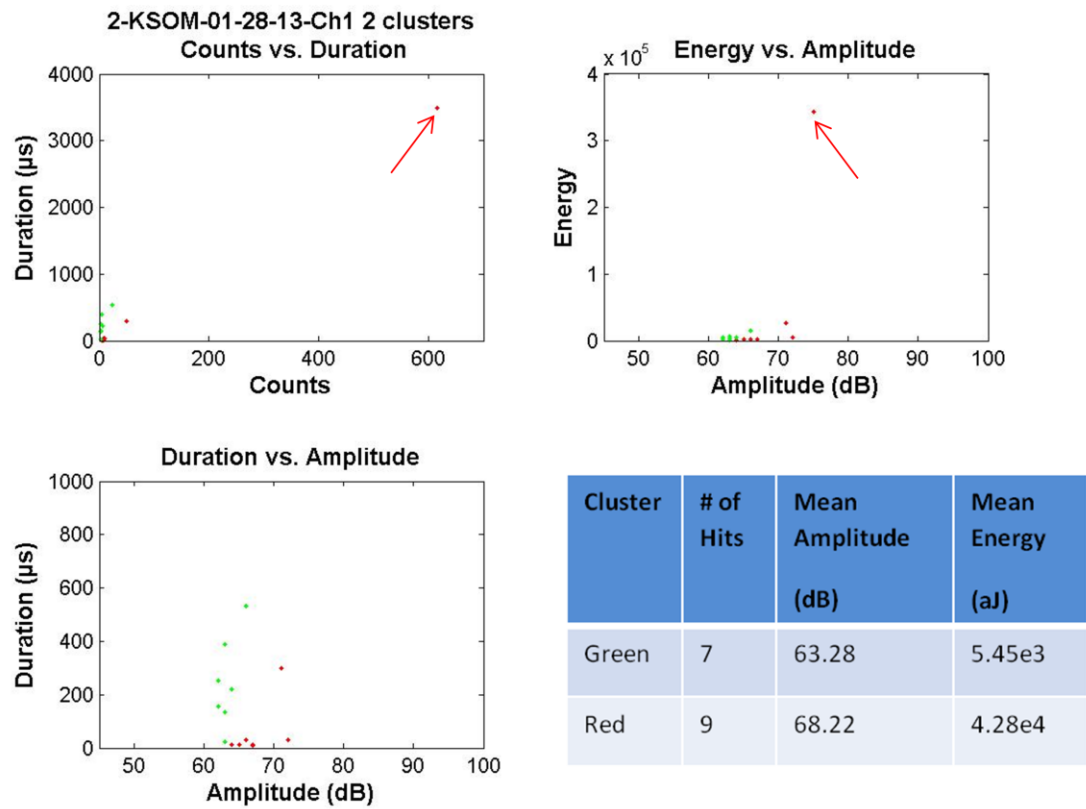


Figure 37- Clustered AE Plot for 01/28/2013 Navair Sensor Channel 1 Data

Following test dates with limited activity on 01/16/2013 and 01/25/2013, the 01/28/2013 data recorded a noteworthy data point with energy levels that dwarf all other data points shown thus far. Similar to the presence of lone high energy hits in the 01/11/2013 AE plot which followed limited activity on 01/10/2013, test dates which feature high energy levels following test dates of limited activity has become a recurrent observation with Navair sensor Channel 1 data. Furthermore, the energy magnitudes of the lone high energy hits have progressively increased from test date to test date.

The Navair sensor Channel 1, 01/29/2013 clustered AE Plot is shown in Figure 38.

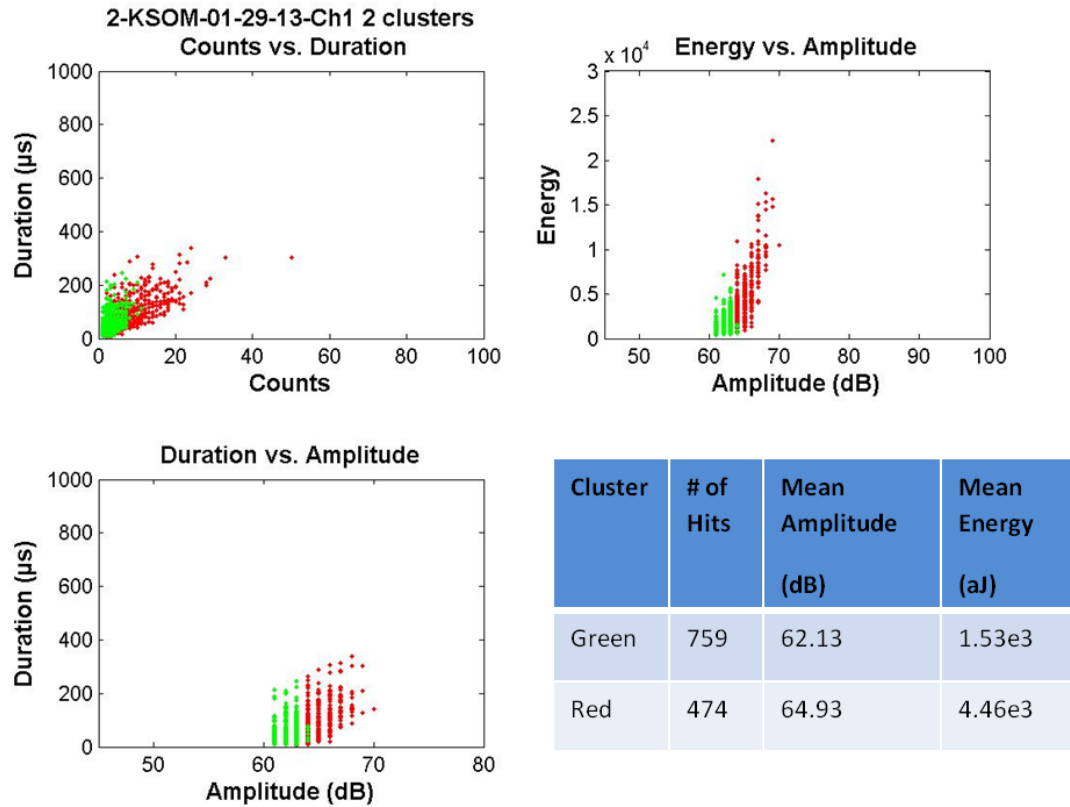


Figure 38 - Clustered AE Plot for 01/29/2013 Navair Sensor Channel 1 Data

The 01/29/2013 AE plot displays the second burst of heavy AE activity. Similar to the burst of activity on 01/14/2014 which followed the presence of high energy hits on 01/11/2013, bursts of heavy activity following test dates which feature lone high energy hits have become a recurrent observation.

The Navair sensor Channel 1, 02/05/2013 clustered AE Plot is shown in Figure 39.

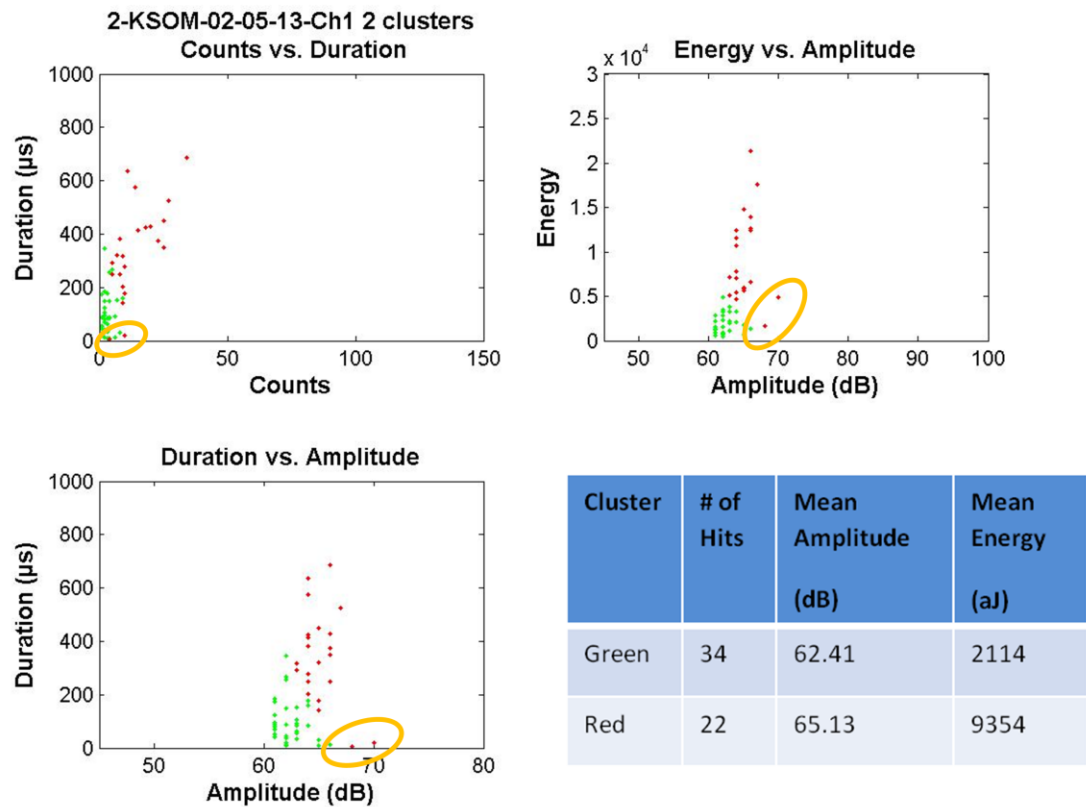


Figure 39 - Clustered AE Plot for 02/05/2013 Navair Sensor Channel 1 Data

The most apparent observation from the 02/05/2013 data is the two data points circled in orange which exhibit energy levels similar to hits in the red cluster seen in the 01/11/2013 AE plot. These two points are also seemingly different from the other hits in the red cluster yet the ANN still grouped them together. When clustering was attempted with three and four clusters, the green cluster was further separated and the two hits remained linked to the hits currently clustered as red in the figure above. Evidently, the two hits contain a similar pattern and trend that was detectable by the ANN. The two circled hits present evidence of crack initiation at End B of the EDM notch.

The Navair sensor Channel 1, 02/07/2013 AE plot seen in Figure 40 below, shows a progression from the 02/05/2013 AE plot and suggests further propagation of the crack front at both ends of the EDM notch.

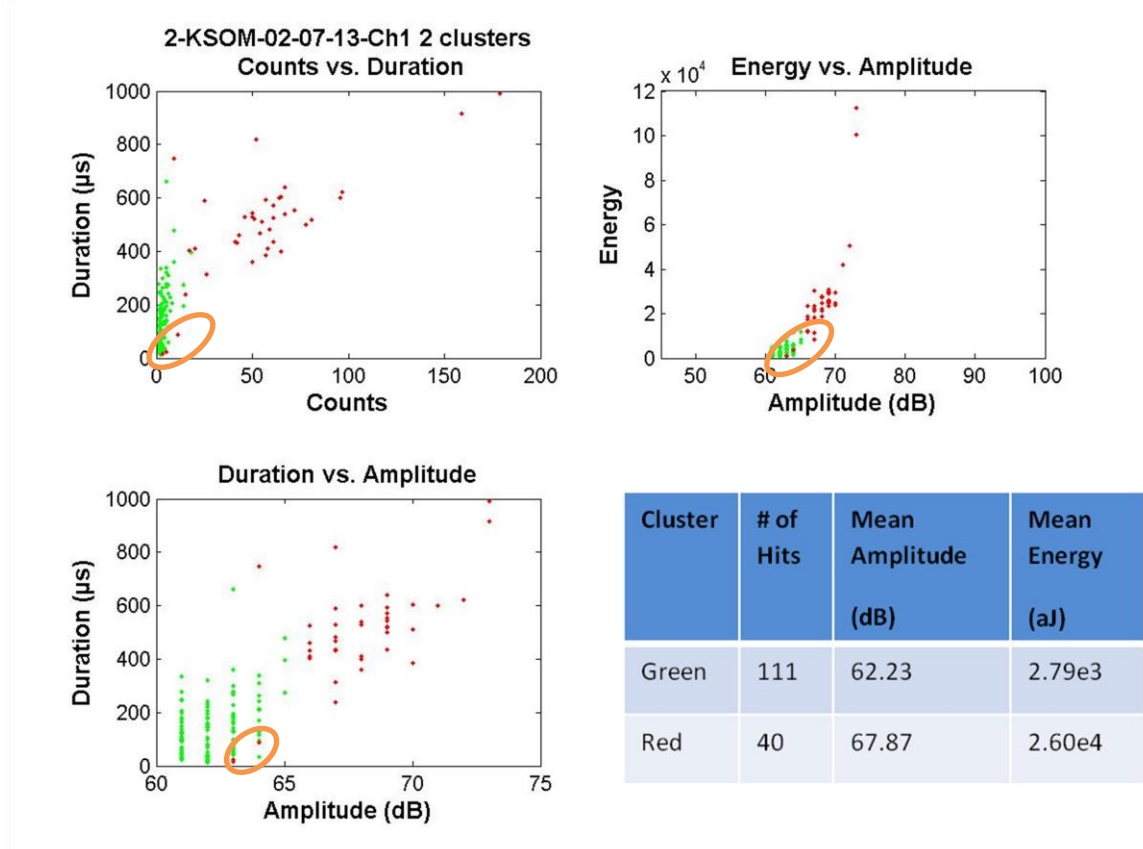


Figure 40 - Clustered AE Plot for 02/07/2013 Navair Sensor Channel 1 Data

6.2.2 Channel 2 Clustered AE Plots

The Navair sensor Channel 2, 12/14/2012 clustered AE Plot is shown in Figure 41.

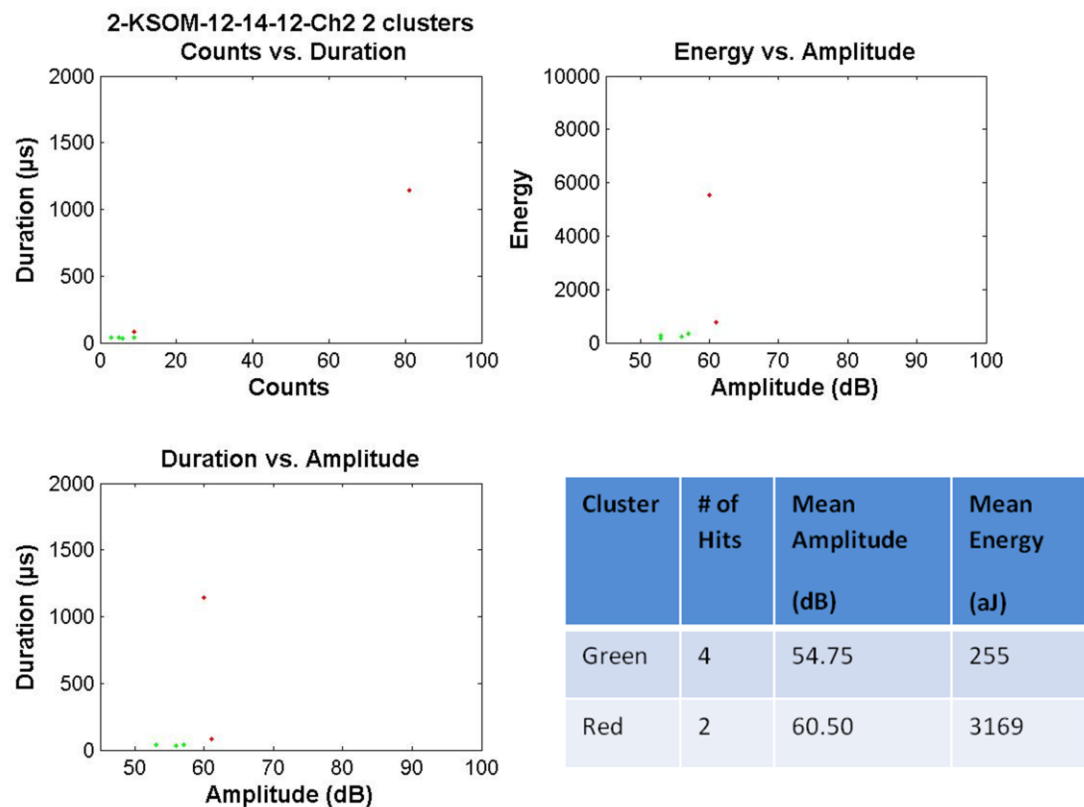


Figure 41 - Clustered AE Plot for 12/14/2012 Navair Sensor Channel 2 Data

As opposed to the Navair sensor Channel 1, 12/14/2012 data, the lower amplitude threshold of Navair sensor Channel 2 is apparent as more hits are recorded in the green cluster of the 12/14/2012 AE Plot. Again, a single hit in the red cluster displays a much higher energy value than all other hits. This agrees with the Navair sensor Channel 1 results, suggesting crack initiation at End A of the EDM notch.

The Navair sensor Channel 2, 01/03/2013 clustered AE Plot is shown in Figure 42.

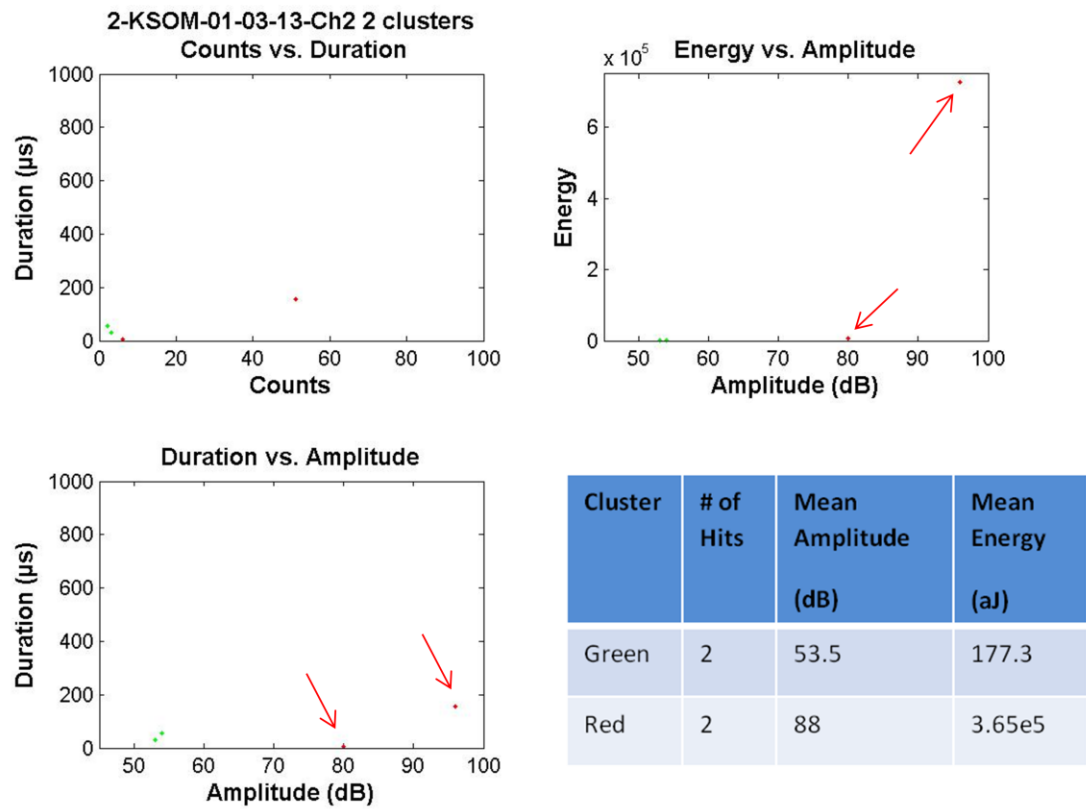


Figure 42 - Clustered AE Plot for 01/03/2013 Navair Sensor Channel 2 Data

Although only four total hits were recorded by Navair sensor Channel 2 on 01/03/2013, two hits had amplitude values above 80 dB with one of those hits exhibiting extremely high energy. Despite the fact that Navair sensor Channel 2 amplitude and energy values are much higher than Navair sensor Channel 1 amplitude and energy values for 01/03/2013 data, the presence of lone hits with significantly high energy is consistent between both channels.

The Navair sensor Channel 2, 01/10/2013 clustered AE Plot is shown in Figure 43.

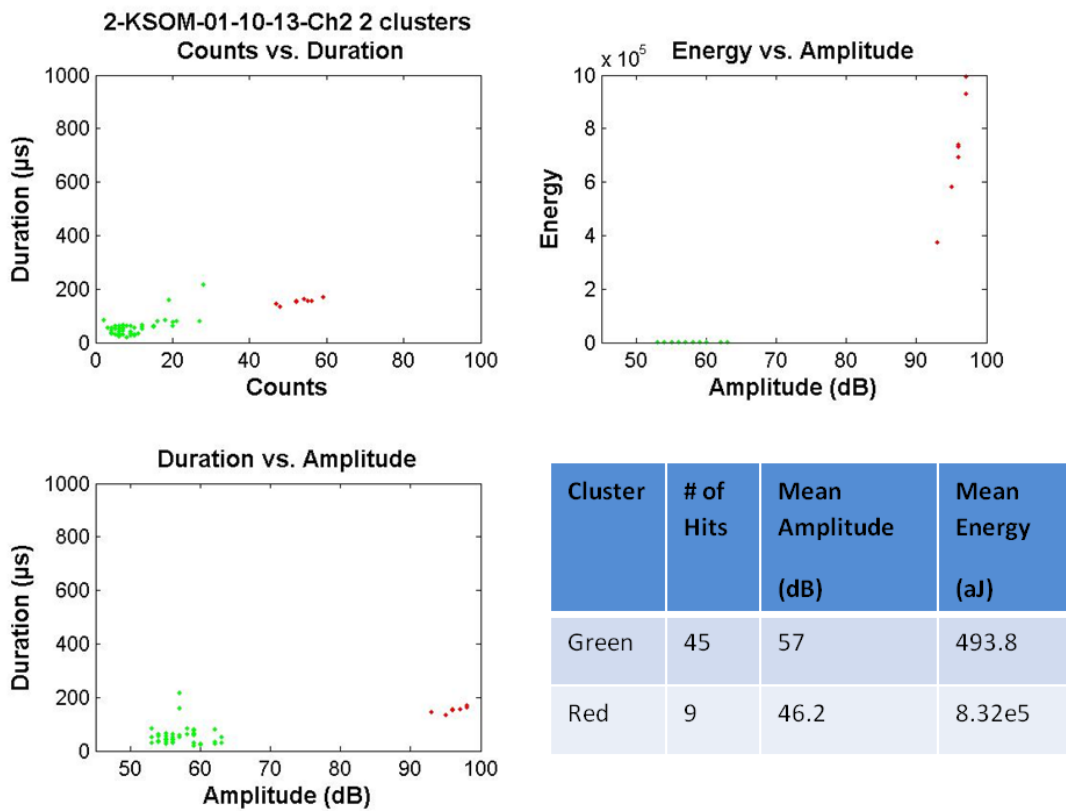


Figure 43 - Clustered AE Plot for 01/10/2013 Navair Sensor Channel 2 Data

The 01/10/2013 Navair sensor Channel 2 data recorded a handful of hits with higher energy and extremely high amplitude values. Though the red hits follow a similar trend as the green hits in the duration versus counts and duration versus amplitude subplots, they are noticeably different in the energy versus amplitude subplot. Considering the fact that digital conversion of an AE wave can have maximum amplitudes of 100 dB, the hits within the red cluster which display amplitude values greater than 90 dB are nearing the saturation point of the AE sensor. The high energy and low duration values of these hits are characteristic of cracking events. Similar AE behavior is present for 01/14/2013

Navair sensor Channel 2 data and 01/28/13 Navair sensor Channal 2 data as seen in Figures 44 and 45 below.

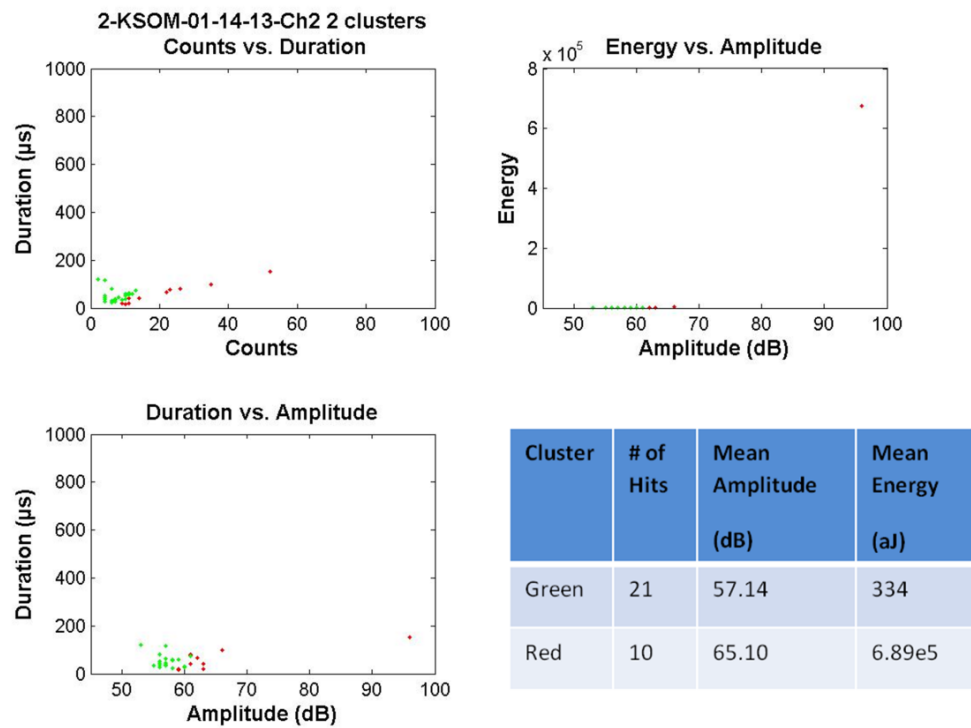


Figure 44 - Clustered AE Plot for 01/14/2013 Navair Sensor Channel 2 Data

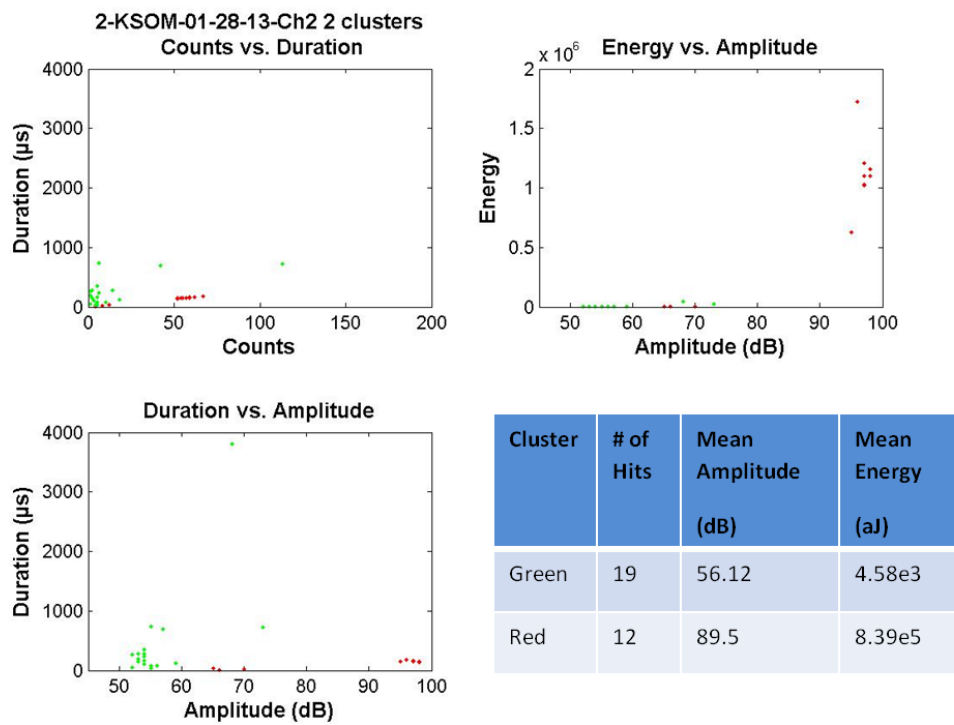


Figure 45 - Clustered AE Plot for 01/28/2013 Navair Sensor Channel 2 Data

The Navair sensor Channel 2, 01/29/2013 clustered AE Plot is shown in Figure 46.

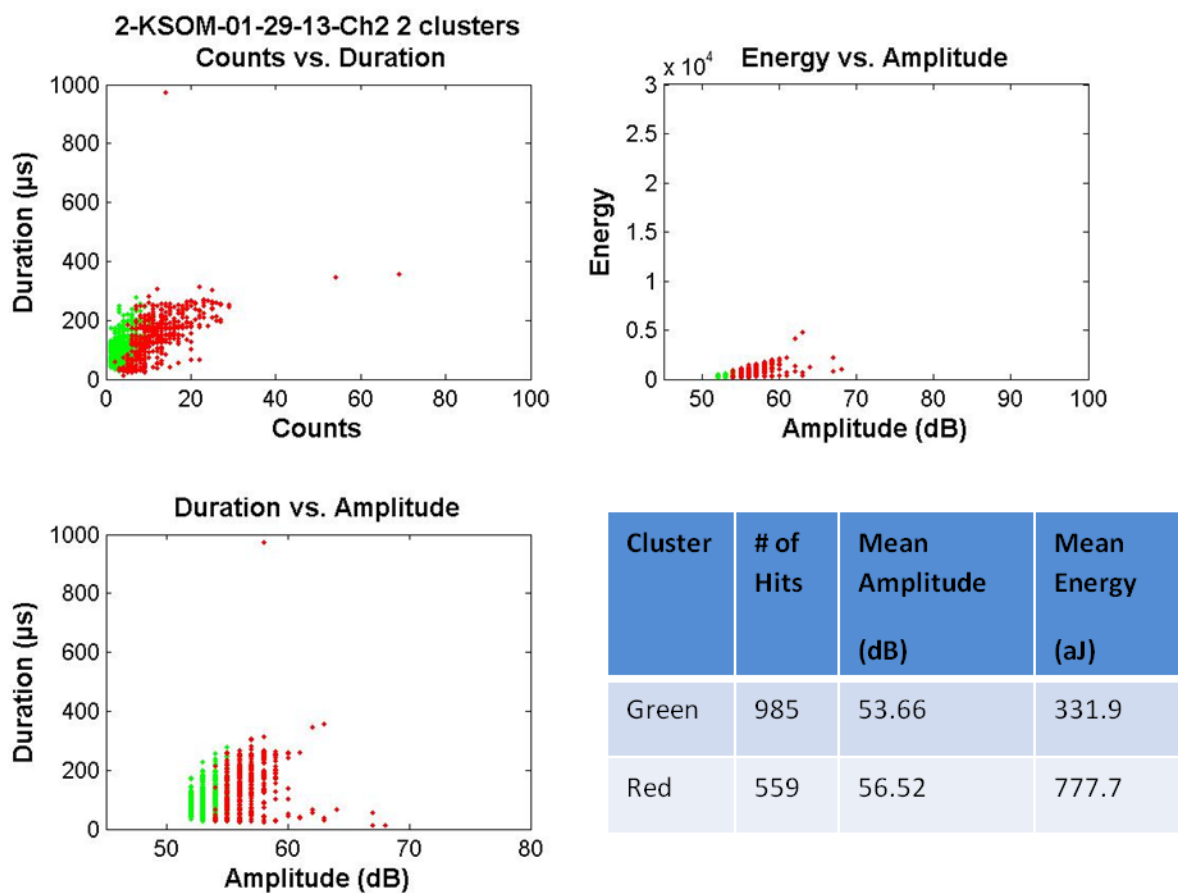


Figure 46 - Clustered AE Plot for 01/29/2013 Navair Sensor Channel 2 Data

Similar to Navair sensor Channel 1, 01/29/2013 data, Navair sensor Channel 2, 01/29/2013 data recorded a burst in AE activity.

The Navair sensor Channel 2, 02/05/2013 clustered AE Plot is shown in Figure 47.

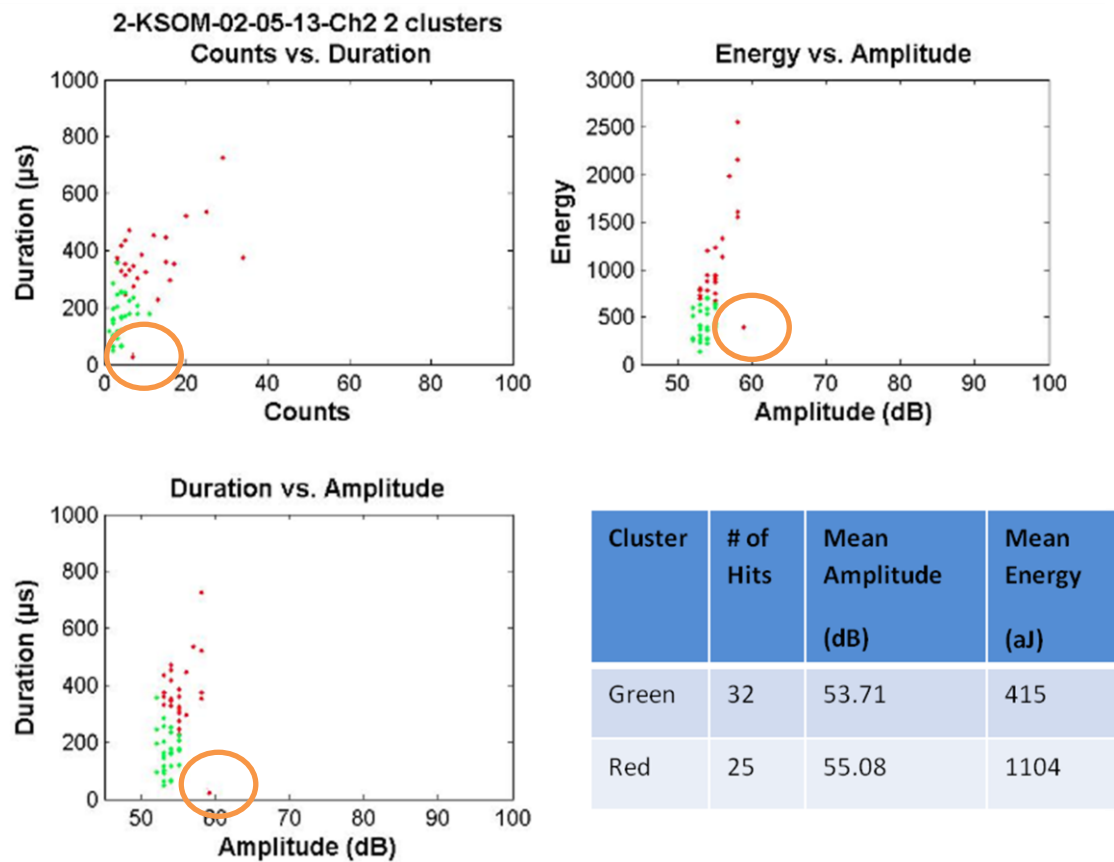


Figure 47 - Clustered AE Plot for 02/05/2013 Navair Sensor Channel 2 Data

In the Navair sensor Channel 2, 02/05/2013 data, a single hit is present, circled in orange, which displays lower energy levels than other hits in the red cluster. This hit corresponds to the initiation of a crack at End B of the EDM notch. Navair sensor Channel 2, 02/05/2013 data, similar to Navair sensor Channel 1, 02/05/2013 data, suggests crack initiation on End B of the EDM notch while the crack on End A of the EDM notch continued to propagate.

The Navair sensor Channel 2, 02/11/2013 clustered AE Plot is shown in Figure 48.

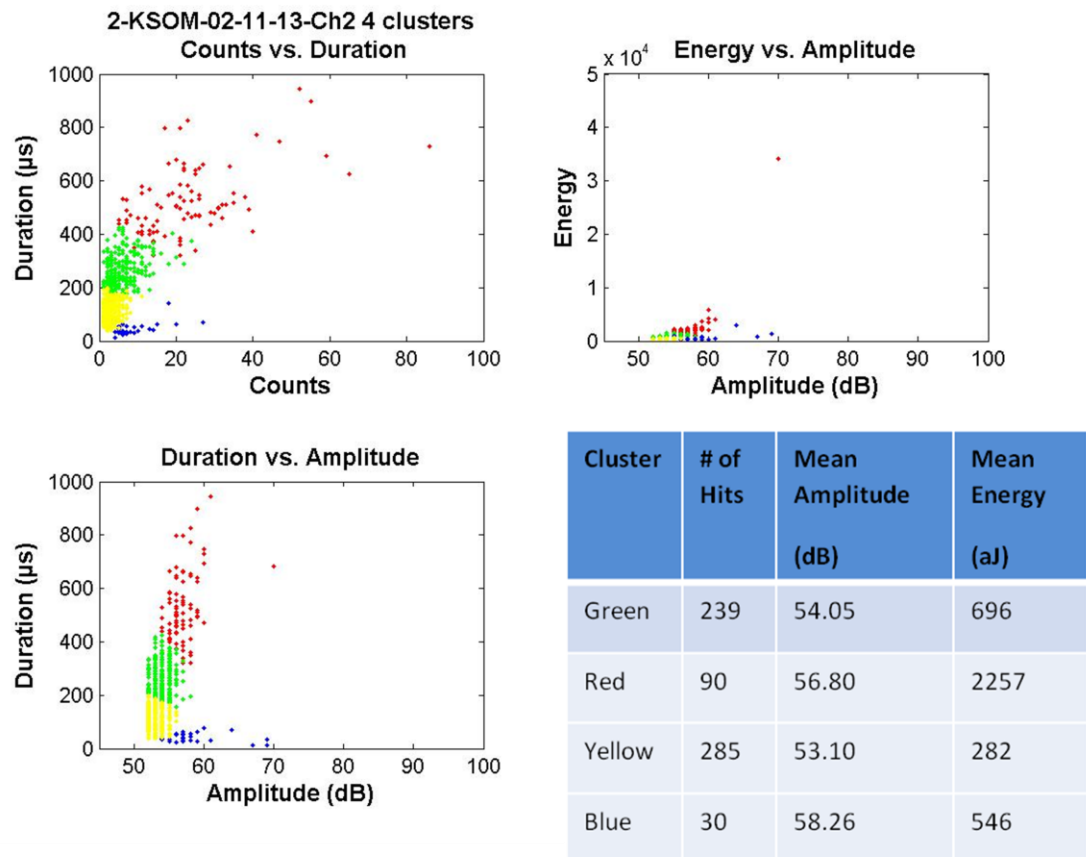


Figure 48 - Clustered AE Plot for 02/11/2013 Navair Sensor Channel 2 Data

For 02/11/2013 Navair sensor Channel 2 data, four clusters were required to fully separate the blue cluster from the other hits. For this AE plot, the red cluster is sourced to cracking on End A of the notch and the blue cluster is sourced to cracking on End B of the notch.

6.3 ERAU Data Clustered Plots Results

ERAU sensor Channel 1 clustered AE plots for selected test dates from the early damage testing interval are presented in this section to display crack initiation from the EDM

notch and/or early state crack propagation. Unfortunately ERAU sensor Channel 1 malfunctioned during February 5th – February 12th testing. Note the value ranges on plot axes differs between test dates. This is to provide a proper scale of the data points within each plot. Arrows are used to point out stand-alone data points which may not be easily visible. Unlike Navair data, the lower amplitude threshold allowed additional sources to be detected by the AE transducer. All plots presented within this section consist of five, six, or seven clusters. In some instances multiple cracking sources were present; thus requiring more clusters to achieve proper separation. Typically one or two cracking sources, represented by red and blue clusters, were present for each test date. Yellow clusters represent plastic deformation hits. Cyan, magenta, green, and black correspond to noise and/or other multiple hit data. Different numbers of clusters were incorporated for different testing dates. ERAU sensor Channel 1 clustered AE plots, in chronological order; can be found in the Appendix.

The ERAU sensor Channel 1, 12/14/2012 clustered AE plot is shown in Figure 49.

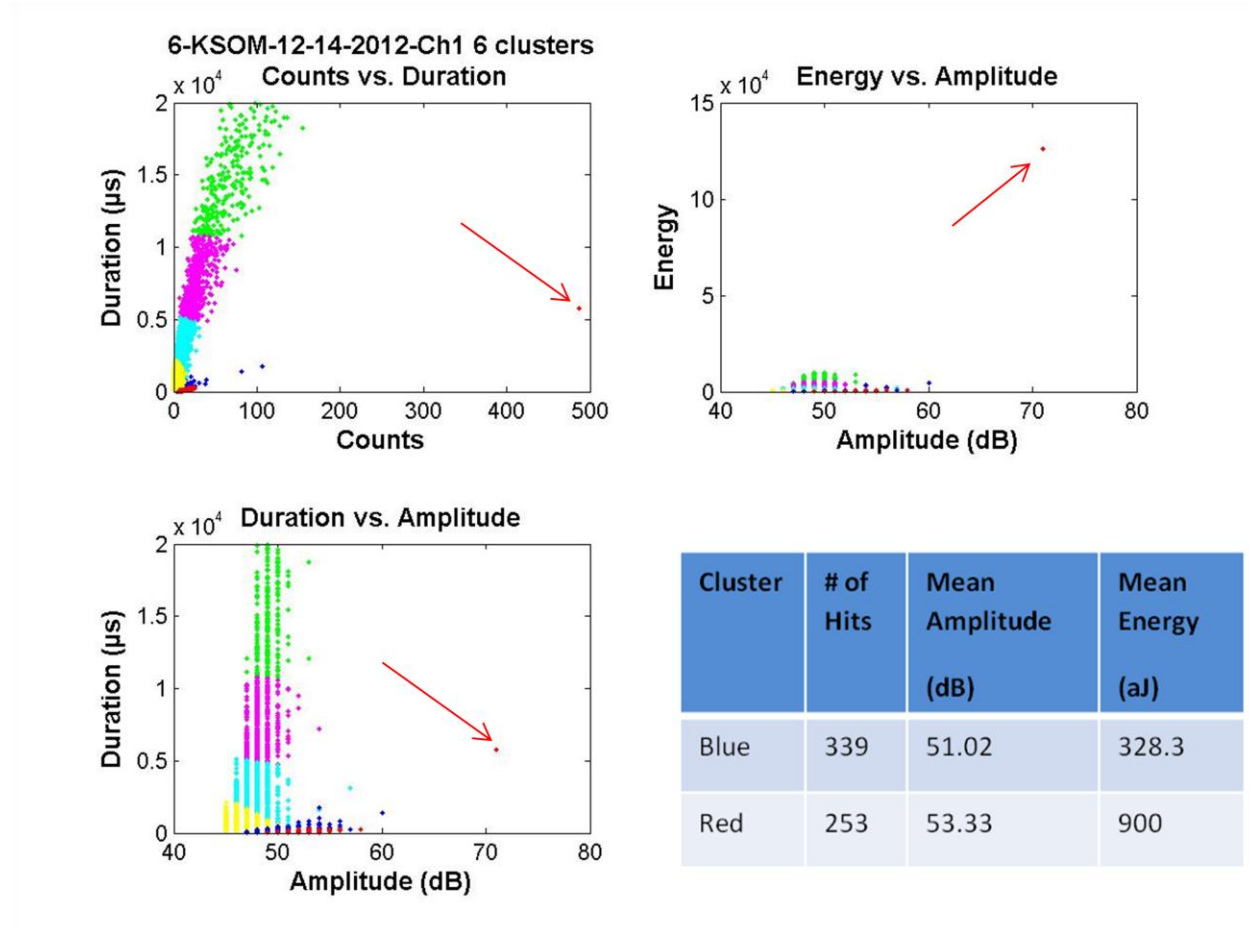


Figure 49 - Clustered AE Plot for 12/14/2012 ERAU Sensor Channel 1 Data

It is important to first note the number of hits in the blue and red clusters is marginally greater than the Navair sensors due to the reduced amplitude threshold. In the 12/14/2013 AE plot, a large number of AE hits in the blue cluster are observed with low amplitude and energy values. The exception is the lone red hit with an energy value of $\sim 1.3e5$ aJ. This hit agrees with the ‘pop-in’ activity at End A of the EDM notch also indicated by the Navair sensor data. As testing progressed, the number of hits in the cracking clusters tends to diminish.

The ERAU sensor Channel 1, 01/03/2013 clustered AE plot is shown in Figure 50.

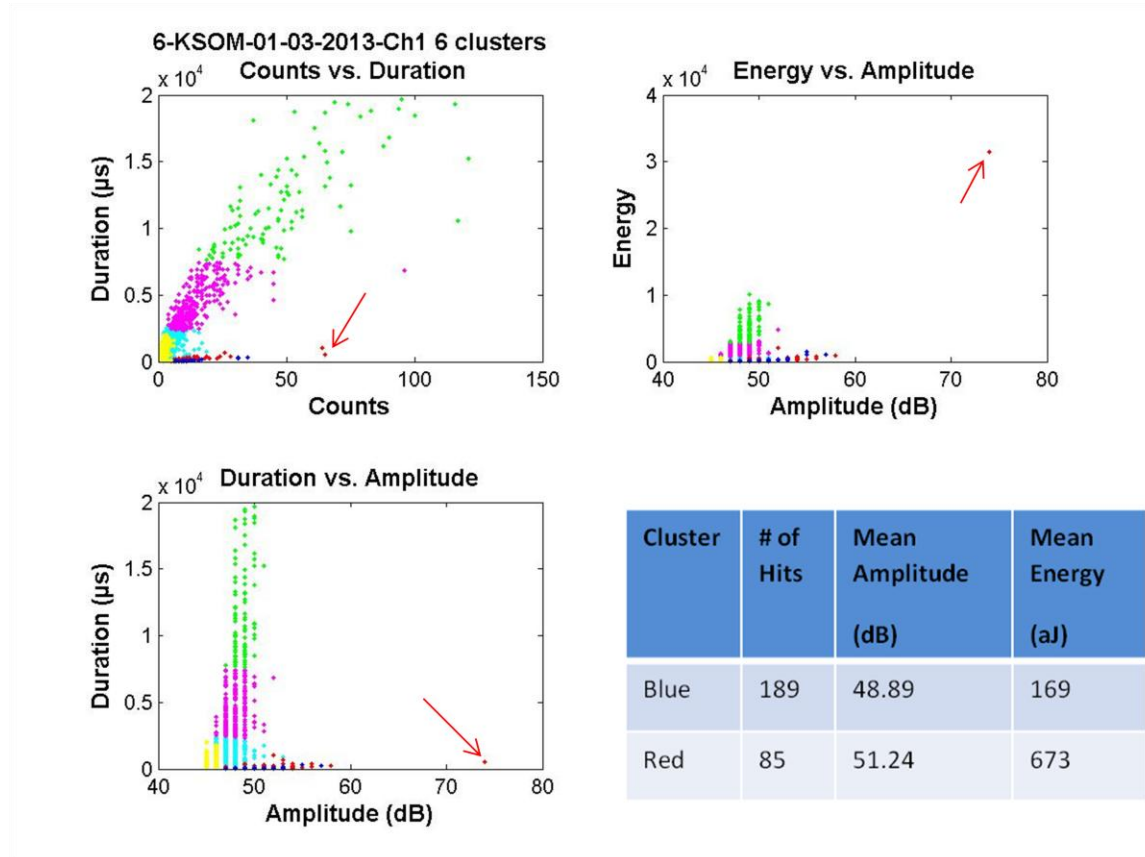


Figure 50 - Clustered AE Plot for 01/03/2013 ERAU Sensor Channel 1 Data

For the 01/03/2013 ERAU sensor Channel 1 data, a decrease in the total number of hits in the red and blue clusters was observed. The presence of a lone high energy hit, grouped to the red cluster, was also observed. The high energy hit seen above is consistent with the 01/03/2013 data seen in both Navair sensor Channel 1 and sensor Channel 2 data.

The ERAU sensor Channel 1, 01/11/2013 clustered AE plot is shown in Figure 51.

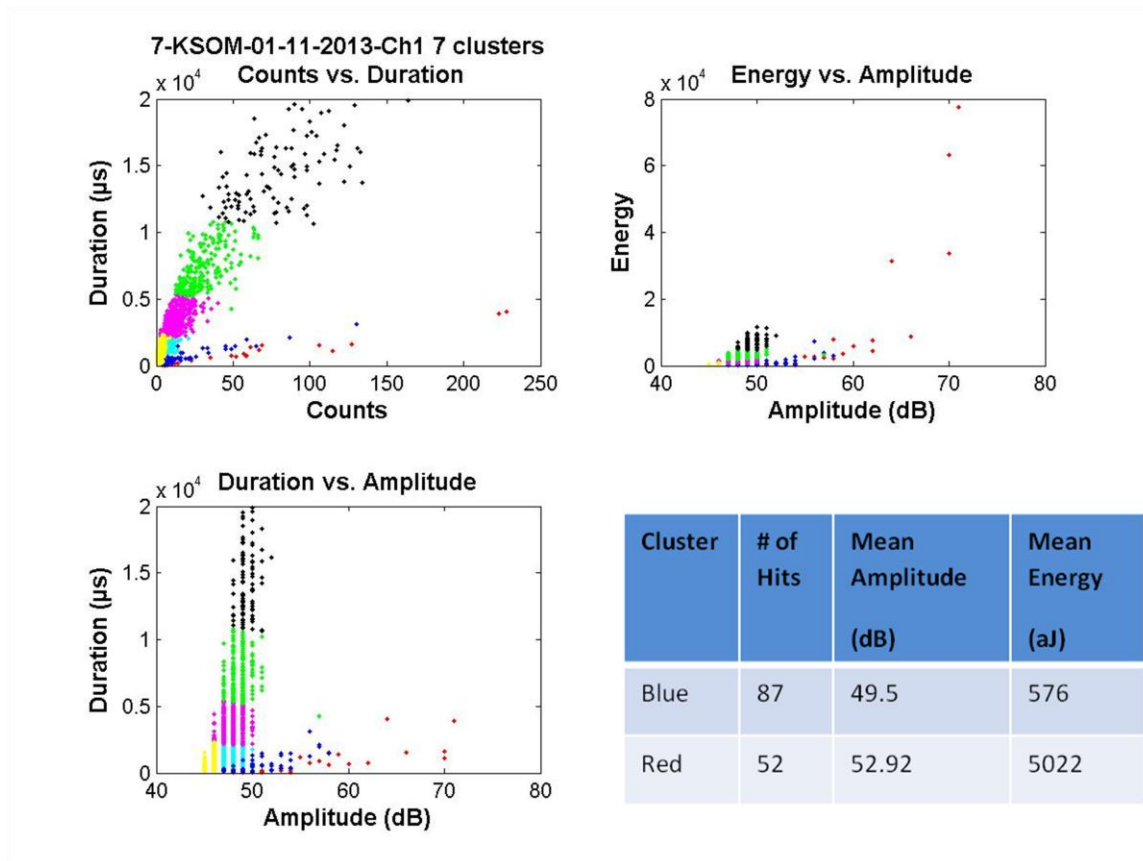


Figure 51 - Clustered AE Plot for 01/11/2013 ERAU Sensor Channel 1 Data

Following a period of relatively little activity during 01/10/2013 testing, 01/11/2013 ERAU Channel 1 data recorded cracking activity across a wide range of amplitudes with a number of high energy hits. Similar to the 01/03/2013 ERAU sensor Channel 1 data, a further decrease in the total number of hits in the red and blue clusters was observed.

Following 01/11/2013 testing, the AE plots for ERAU Channel 1 recorded fewer and fewer hits within the red and blue cracking clusters. A burst of activity for 01/14/2013 and 01/29/2013 data, and the presence of extremely high energy hits for 01/28/2013 data

were not observed with the ERAU sensor Channel 1 data as was seen with the Navair sensors.

6.4 Cumulative Hit Count Plots

6.4.1 Navair Sensor Channel 1 and Channel 2

Given the increased amplitude thresholds and lack of noise signals for Navair sensor data compared to ERAU sensor data, the development of cumulative plots for Navair data is composed of all the hits shown in the clustered plots. Therefore most of the hits in the cumulative hit count profile will be composed of hits sourced to cracking activity or plastic deformation. The log-log scale of cumulative hit count versus total test time through February 12th testing for Navair sensor Channel 1 is shown in Figure 52.

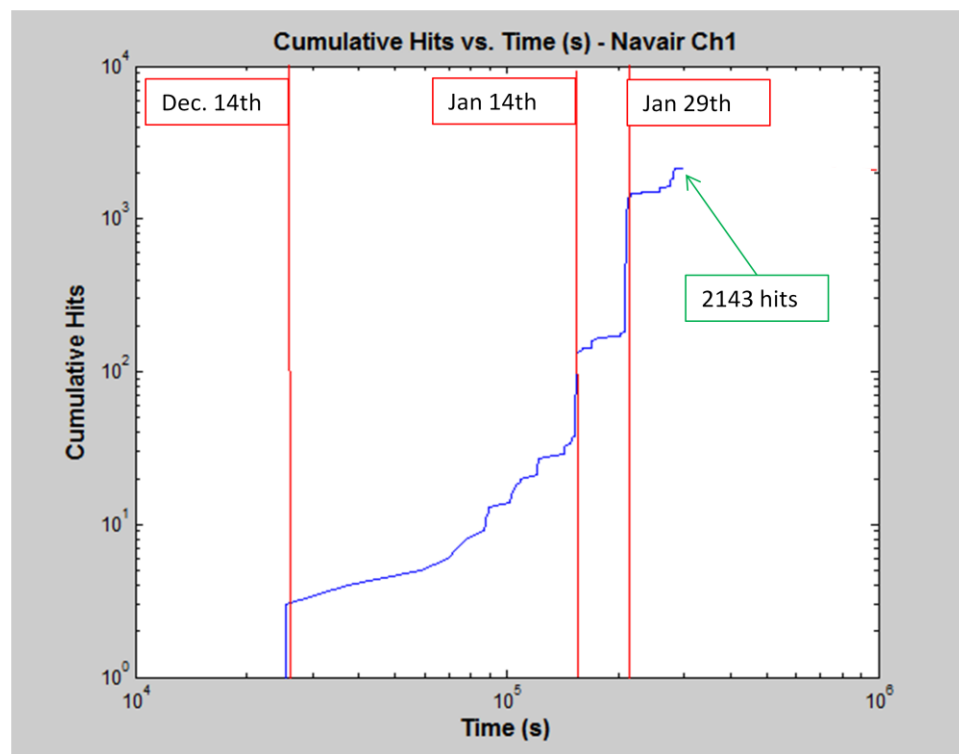


Figure 52 – Cumulative Hit Count Profile for Navair Sensor Channel 1 Data

Similarly, the log-log scale of cumulative hit count versus total test time through February 12th testing for Navair sensor Channel 2 is shown in Figure 53.

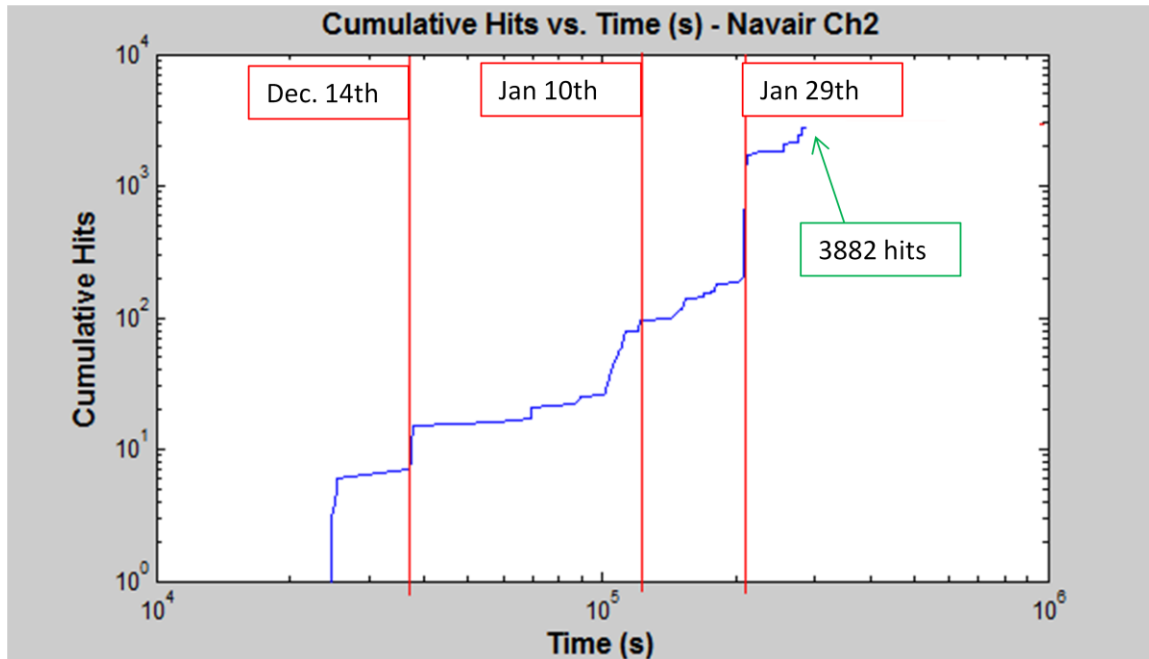


Figure 53 – Cumulative Hit Count Profile for Navair Sensor Channel 2 Data

Two apparent differences exist between the Navair sensor Channel 1 and Navair sensor Channel 2 cumulative plots; specifically two jumps in activity recorded on 12/14/2012 for Navair sensor Channel 2 data as compared to only one jump on 12/14/2012 for Navair sensor Channel 1 data, and the difference in location of the second jump in activity. Despite these differences, the cumulative hit count profiles of Figures 52 and 53 generally agree with each other as they both include a series of jumps and yield a similar magnitude in the total hit count. Furthermore, the observation of a series of jumps in the cumulative hit count profile as testing progresses matches the former investigation of crack growth in cyclically loaded specimens per Figure 10 as discussed in Section 3.3 of the literature review chapter of the thesis.

6.4.2 ERAU Sensor Channel 1

Unlike Navair sensor data, the large quantity of noise signals common to AET of rotary components and other non-cracking events would significantly affect the form of a cumulative AE hit count plot; specifically the appearance of successive jumps on the log-log scale as testing progresses. To circumvent this issue, red and blue cracking clusters as seen in the ERAU sensor Channel 1 clustered plots are extracted and compiled to obtain a cumulative AE hit count profile for cracking events alone. Figure 54 displays the resulting profile.

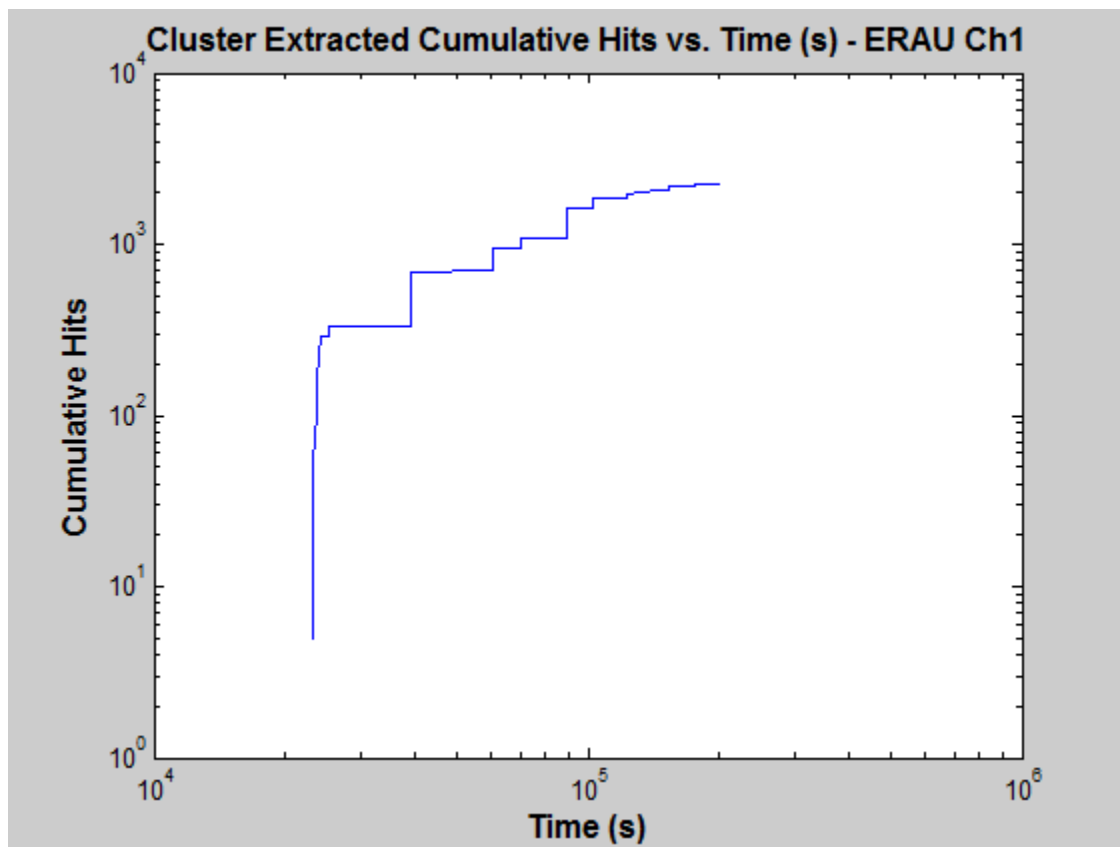


Figure 54 – Cumulative Hit Count Profile for ERAU Sensor Channel 1 Data

As opposed to cumulative plots developed for Navair sensor data, the size of the jumps in the cumulative hit count for ERAU data decrease as testing progresses. From the ERAU sensor Channel 1 clustered plot inspection, this agrees with the fact that the number of hits in cracking clusters decreased as testing progressed. Though the above figure does not match the former investigation of crack growth in cyclically loaded specimens per Figure 10, it does provide additional insight. Unlike the Navair sensor data, ERAU sensor Channel 1 cumulative hit count plots were compiled using AE sensors with a wider amplitude range and only AE hits which were sourced to cracking activity and therefore provides a more comprehensive display of cracking activity throughout the early damage state testing interval.

CHAPTER 7 – Conclusions and Recommendations

7.1 Conclusions

In response to incident failures of the tail gearbox to an array of Sikorsky H60 variations, Navair was contracted to investigate the crack growth of a crack propagating from the output bevel gear splines. The ground test stand, located in Patuxtent River, MD, was capable of replicating a bi-loading scenario to simulate in-flight tail rotor torque and hub moment load ranges. An electro-discharge machined notch was implemented in the root-to-tip direction of the gear tooth face to prompt initiation of a crack which propagates in a circumferential fashion about adjacent gear splines. Two separate data acquisition devices with Navair and ERAU piezoelectric transducers were used to monitor acoustic activity emanating from the flaw.

An interval of testing was defined as the early damage state testing interval which extended from the beginning of testing, 12/14/2012, up until a crack was observed on both ends of the EDM notch on 02/12/2013. Data sets from three AE sensors, two Navair and one ERAU, were analyzed to characterize early damage state crack initiation and propagation emanating from the EDM notch. To distinguish cracking activity from other AE sources, an algorithm developed at the ERAU Structure Health Monitoring and Nondestructive Evaluation Laboratory was applied to all data sets to create clustered AE plots. Upon extensive data preprocessing and filtering, the Kohonen Self-Organizing Map artificial neural network was used to identify patterns within the data and distinguish between the various AE sources. Visual and mathematical verification of the clustered AE plots produced by the ERAU algorithm was performed to determine the optimal

artificial neural network configuration. Cracking clusters were extracted and compiled to produce cumulative plots of relevant cracking activity throughout the early damage state testing interval.

The analysis of Navair sensor Channel 1 and Channel 2 data provided four primary observations:

- 1) A series of test dates throughout the early damage testing interval, most notably 12/14/2012, 01/03/2013, 01/11/2013, and 01/28/2013, feature AE hits with energy and amplitude levels significantly higher than other hits in the data set. This activity represents sudden and severe initiation of a crack from a previously stable configuration and agrees with the “pop-in” initiation activity observed by Miller et al [23].
- 2) The AE activity described in observation 1) occurs after test dates which feature limited activity.
- 3) Bursts in AE activity are observed in test dates immediately following those which feature the AE activity described in observation 1). This is most notable on 01/14/2013 and 01/29/2013 testing.
- 4) AE hits which resemble crack initiation on End A of the notch on 12/14/2012 and 01/03/2013 are observed in the 02/05/2013 AE Plot and indicate crack initiation on End B of the notch. Propagation of the crack front at End B of the EDM notch is noticeable on 02/07/2013 and 02/11/2013.
- 5) The cumulative AE hit count plots display a series of jumps in the cumulative hit count profile. These jumps appear to gradually increase in size on the log-log scale.

These results agree with the former investigation of crack growth in cyclically loaded specimens.

The analysis of ERAU sensor Channel 1 data, similar to Navair channel data noted the following observation:

- 1) High amplitude and high energy, “pop-in” activity, was observed in the AE Plots for 12/14/2012, 01/03/2013 and 01/11/2013 test dates.

Unlike Navair sensor data, however, ERAU sensor Channel 1 data did not indicate any “pop-in” activity on 01/28/2013. Bursts of activity on 01/14/2013 and 01/29/2013 were not present. The lack of ERAU Channel 1 data for February testing further limits the conclusions that can be drawn.

7.2 Recommendations

The extent of this thesis only applies to three out of ten total AE sensors and a period of testing such that a flaw had initiated on both ends of the EDM notch. A more in-depth analysis of additional channels and test dates beyond the early damage state testing interval is recommended. In the instance the H60 TGB OBG experiment is repeated, or a similar experiment using rotary components is devised, a study of the AE methods used to collect Navair and ERAU data should be conducted. The reason for this would be two-fold. First, an amplitude threshold between the setting for ERAU channels and range of settings for Navair channels should be determined. An amplitude threshold of 45 dB allows too many noise signals to be recorded where as threshold settings as high as 62 and 70 risk losing valuable data. This would also prevent the collection of data similar to

that of ERAU sensor Channel 1 in which an excessive amount of noise signals were recorded.

Due to the fact that noise increases as AET of rotating machinery progresses, a floating or smart threshold should be explored which manually or automatically increases the threshold setting as testing progresses. Since multiple AE transducer types were used in this experiment, the layout file settings and other data collection techniques should be customized for each sensor channel. These efforts would assist in ensuring proper collection of AE data and would streamline data analysis.

A thorough review of signal and information processing will allow further development of the clustering algorithm to streamline data processing and analysis and ultimately pave the way to real time data processing. One possible alternative to the current data processing and analysis algorithm could include change-point detection methodology. Change point detection is concerned with the detection of statistical changes in data while minimizing the detection delay subject to false alarm constraints. This option could be valuable in detecting variations to the baseline noise signal common to rotary component operation. A Lycoming T53 test stand, designed and assembled at ERAU could be utilized to conduct in-house experiments to assess a typical baseline noise signal common to rotary component operation. Comparative studies of gearbox data collection using AE transducers could also be performed. The Lycoming T-53 test stand is documented in Appendix C.

REFERENCES

- [1] J. Shishino. “Acoustic Emission Signal Classification for Gearbox Failure Detection.” Embry-Riddle Aeronautical University. Daytona Beach, FL. 2012.
- [2] Naval Air Warfare Center Aircraft Division, “H-60 Tail Gearbox Output Bevel Gear Spline Crack Growth Test,” Patuxtent River, MD. 2008.
- [3] Sikorsky Aircraft Corporation, “Blackhawk – Three Unforgettable Decades.” [Online]. 2007.
- [4] Sikorsky Aircraft Corporation. “MH60 Seahawk Overview.” [Online]. 2007.
- [5] United States Army Aviation Warfighting Center. “UH-60A Powertrain/Rotor System Student Handout.” Fort Rucker, AL. 2008.
- [6] Sikorsky Aircraft Corporation. “Materials Engineering Report: MER-SU1101241-Rev1.” 2011.
- [7] R. K. Miller; E. v. Hill and P.O. Moore. *Nondestructive Testing Handbook Volume 6 – Acoustic Emission Testing, 3rd Edition*. Columbus, OH. American Society for Nondestructive Testing. 2005.
- [8] B. Muravin. “Acoustic Emission Science and Technology.” Journal of Building and Infrastructure Engineering of the Israeli Association of Engineers and Architects. 2009.
- [9] S. Knoeller and B. J. Ingold. “Selecting a Nondestructive Testing Method, Part VII: Acoustic Emission Testing.” AMMTIAC Quarterly. Volume 5, Number 2. Rome, NY. 2010.
- [10] H. E. Boyer. *Metals Handbook, 8th Edition, Volume 11: Nondestructive Inspection and Quality Control.* American Society for Metals. 1976.
- [11] R. Cotta and L. Levy. “Fail Safe Insurance for KC-135.” *Aviation*. 1979.
- [12] C. L. Rovik. “Classification of In-flight Fatigue Cracks in Aircraft Structures using Acoustic Emission and Neural Networks.” Embry-Riddle Aeronautical University. Daytona Beach, FL. 1998

- [13] NDT Resource Center. “AE Signal Parameters.” [Online].
- [14] D. Xu, J. Chang, J. Li, et al. “Dislocation of Deformation Twinning: Confining Pressure Makes a Difference.” Materials Science and Engineering. 2004.
- [15] NDT Resource Center. “Fracture Toughness” [Online].
- [16] A. Hassan, D. Siegel and J. Lee. “A systematic Methodology for Gearbox Health Assessment and Fault Classification. International Journal of Prognostics and Health Management. 2011.
- [17] D. Jelaska, S. Glodez, J. Kramberger and S. Podrug. “Numerical Modeling of Gear Tooth Root Fatigue Behaviour.” University of Split. Split, Croatia. 2007.
- [18] B. Abersek and J. Flaske. “Stress Intensity Factor for Cracked Gear Tooth.” Theoretical and Applied Fracture Mechanics. Volume 20. 1994.
- [19] V. Spitas, C. Spitas, G. Papadopoulos and T. Costopoulos. “Experimental Evaluation of Stress Intensity Factors in Spur Gear Teeth.” Fracture of Nano and Engineering Materials and Structures. 2006.
- [20] A. K. Eriki, R. Ravichandra and M. E. Mustaffa. “Spur Gear Crack Propagation Path Analysis using Finite Element Method.” Proceedings of the International Multi-Conference of Engineers and Computer Scientists, Volume II. Hong Kong. 2012.
- [21] M. D. Dorfman. “Ultimate Strength Prediction in Fiberglass/Epoxy Beams Subjected to Three-Point Bending using Acoustic Emission and Neural Networks.” Embry-Riddle Aeronautical University. Daytona Beach, FL. 2004.
- [22] A. Korcak. “Fatigue Life Prediction in Bridge Steel using Acoustic Emission Amplitude Histograms and Back Propagation Neural Networks.” Embry-Riddle Aeronautical University. Daytona Beach, FL. 2010.
- [23] R. K. Miller, M. Carlos and R. D. Finlayson. “Helicopter Drivetrain Damage Detection and Classification using Acoustic Emission and a Kinematic Variable.” Journal of the American Helicopter Society. 1999.

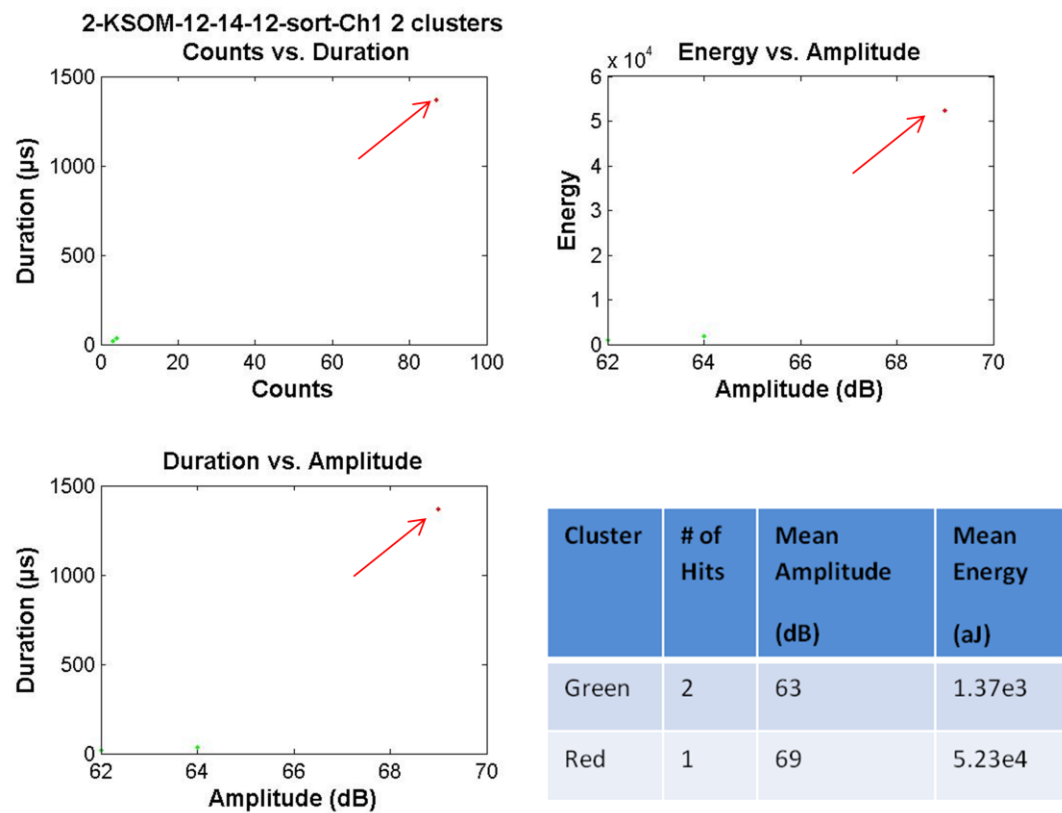
- [24] M. Huang, L. Jiang, P. K. Liaw, et al. "Using Acoustic Emission in Fatigue and Fracture Materials Research." *Journal of the Minerals, Metals, and Materials Society*. Volume 50. Number 11. 1998.
- [25] H. L. Ewalds and R. J. Wanhill. *Fracture Mechanics*. Edward Arnold Publication. London, UK. 1989.
- [26] N. Nemati. "Acoustic Emission Assessment of Steel Bridge Details Subjected to Fatigue." PhD Thesis. University of Miami. Miami, FL. 2012.
- [27] D. O. Harris and H. L. Dunegan. "Continuous Monitoring of Fatigue Crack-Growth by Acoustic Emission Techniques. *Journal of the Society for Experimental Stress Analysis*. Volume 14. Number 2. 1974
- [28] A. A. Pollock. "Material Brittleness and the Energetics of Acoustic Emission." *Proceedings of the SEM Annual Conference*. Indianapolis, IN. 2010.
- [29] D. O. Harris and R. L. Bell. "The Measurement and Significance of Energy in Acoustic Emission Testing." *Experimental Mechanics*. Volume 17. Issue 9. 1977.
- [30] T. C. Lindley, I. G. Palmer and C. E. Richards. "Acoustic Emission Monitoring of Fatigue Crack Growth." *Journal of Materials Science and Engineering*. Volume 32. 1978.
- [31] A. Berkovits and D. Fang. "Study of Fatigue Crack Characteristics by Acoustic Emission." *Engineering Fracture Mechanics*. Volume 51. Number 3. 1995.
- [32] T. M. Roberts and M. Talebzadeh. "Acoustic Emission Monitoring of Fatigue Crack Propagation. *Journal of Constructional Steel Research*. Volume 59. 2003.
- [33] J. Yu, P. Ziehl and J. Caicedo. "Acoustic Emission Monitoring and Fatigue Prediction of Steel Bridge Components." *Proceedings of SPIE Conference*. Volume 8694. 2013.
- [34] Rexnord Industries, LLC, Gear Group. "Failure Analysis: Gears, Shafts, Bearings and Seals." Milwaukee, WI. 1978.
- [35] PH Tool. "What is EDM?" [Online].
- [36] Mistras Group. "32-Channel Micro-II AE System Product Data Sheet." [Online.]

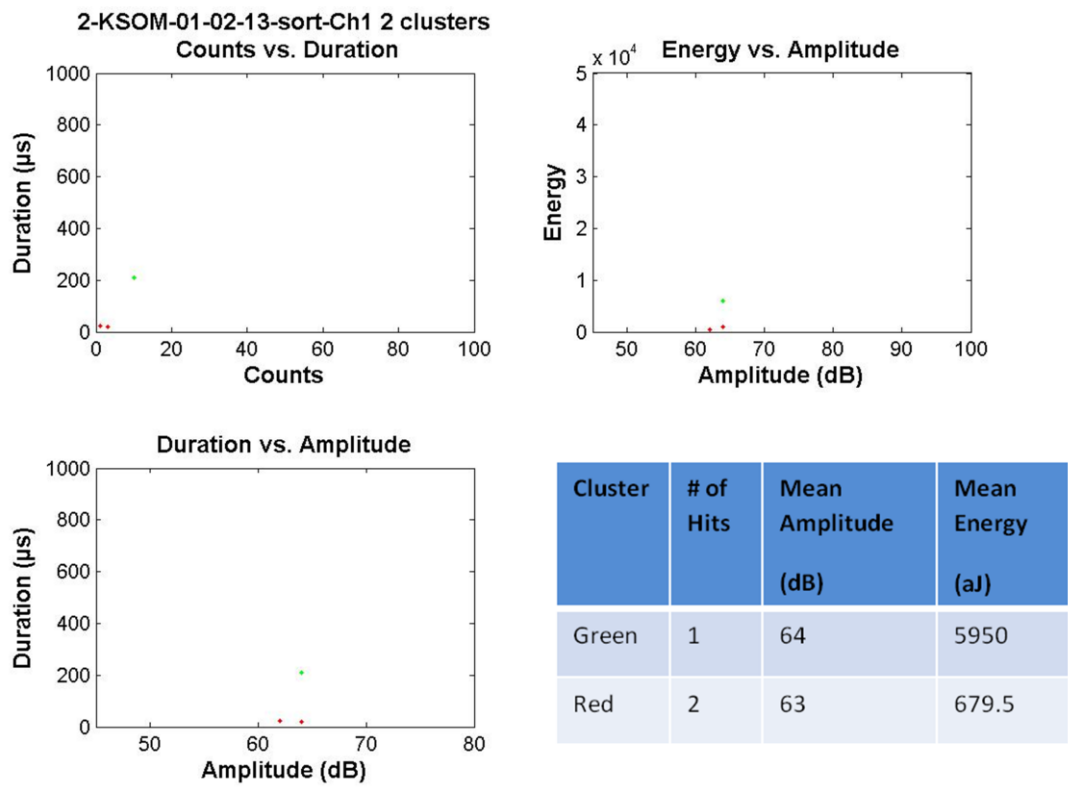
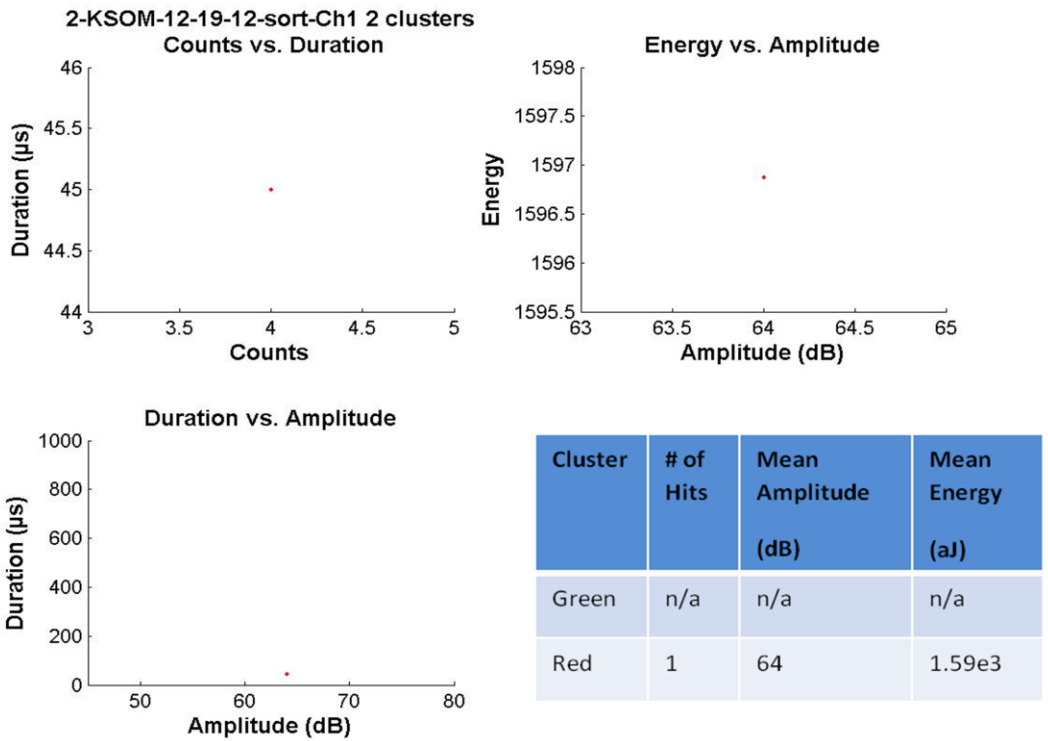
- [37] Mistras Group. “μDiSP Product Data Sheet - Notebook Based Portable DSP Workstation for Advanced Acoustic Emission Testing.” [Online].
- [38] Mistras Group. “WD Sensor Product Data Sheet” [Online].
- [39] Mistras Group. “Micro30 Sensor Product Data Sheet” [Online].
- [40] Mistras Group. “R15I-AST Sensor Product Data Sheet” [Online].
- [41] A. A. Pollock. “AE Signal Features: Energy, Signal Strength, Absolute Energy and RMS.” Mistras Group Acoustic Emission Tech Notes. 2012.
- [42] StackOverflow. “MATLAB with Self-Organizing Map (SOM)” [Online].

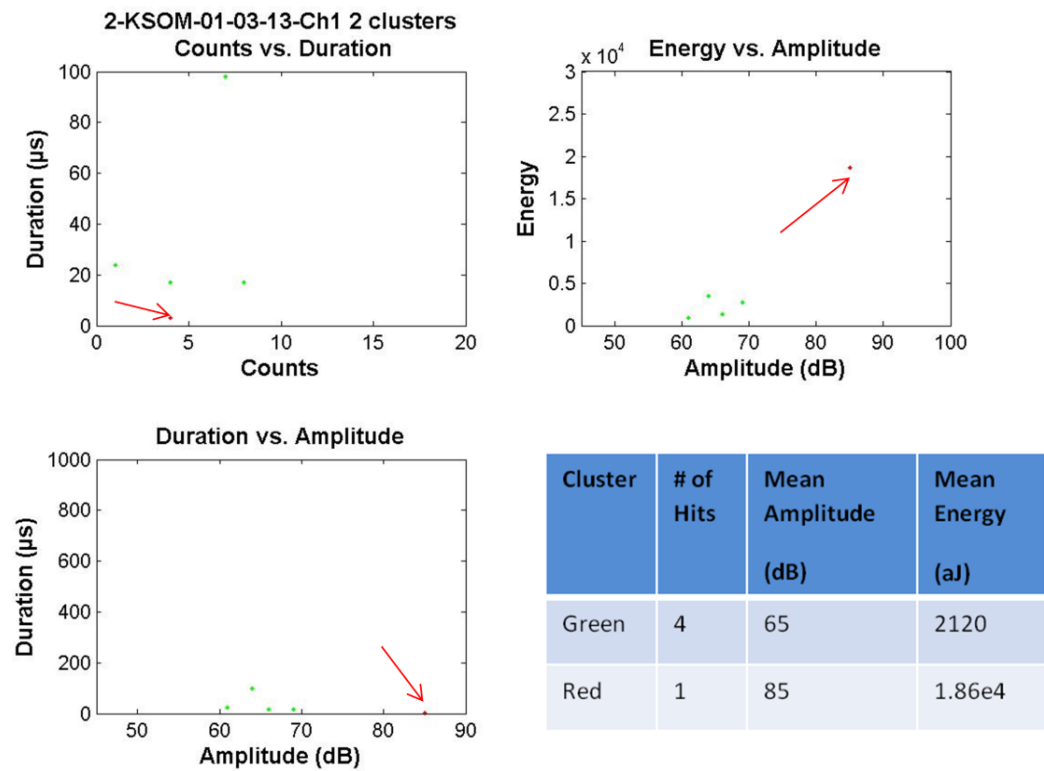
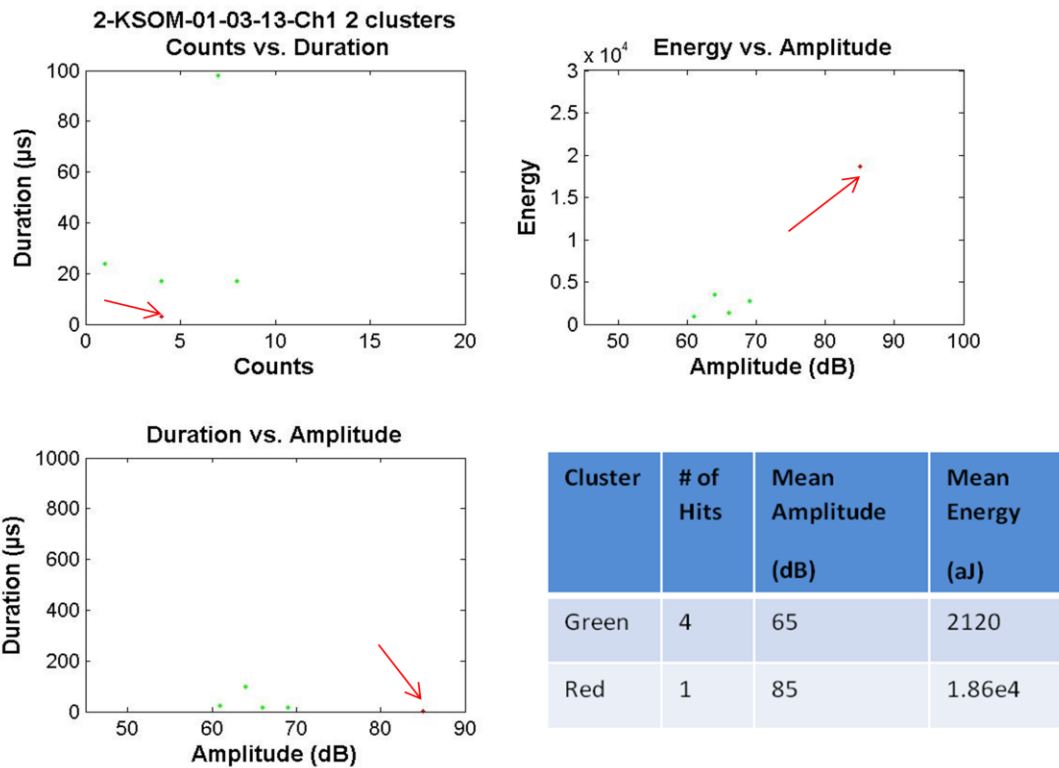
APPENDICES

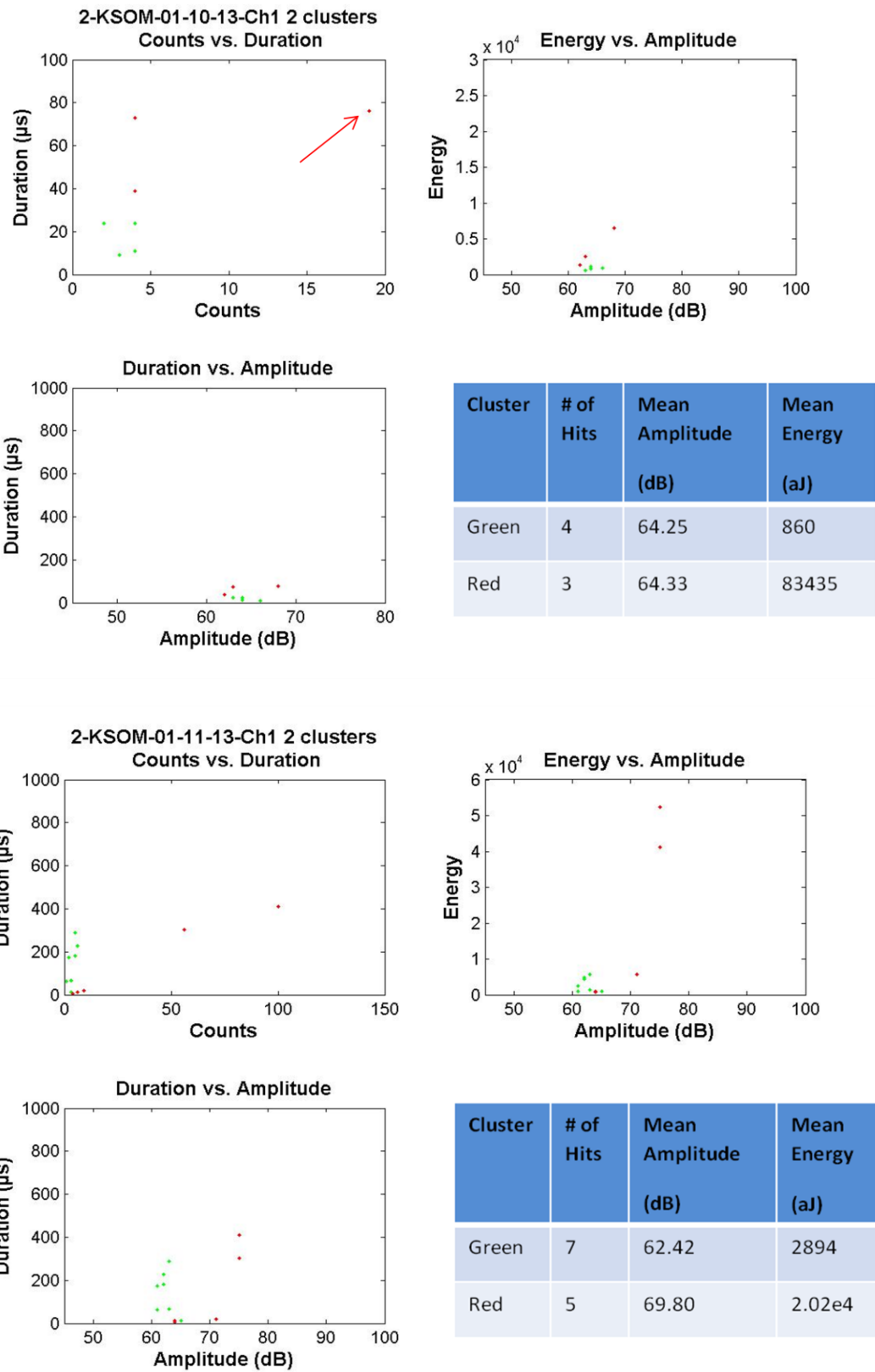
APPENDIX A – Clustered AE Plots

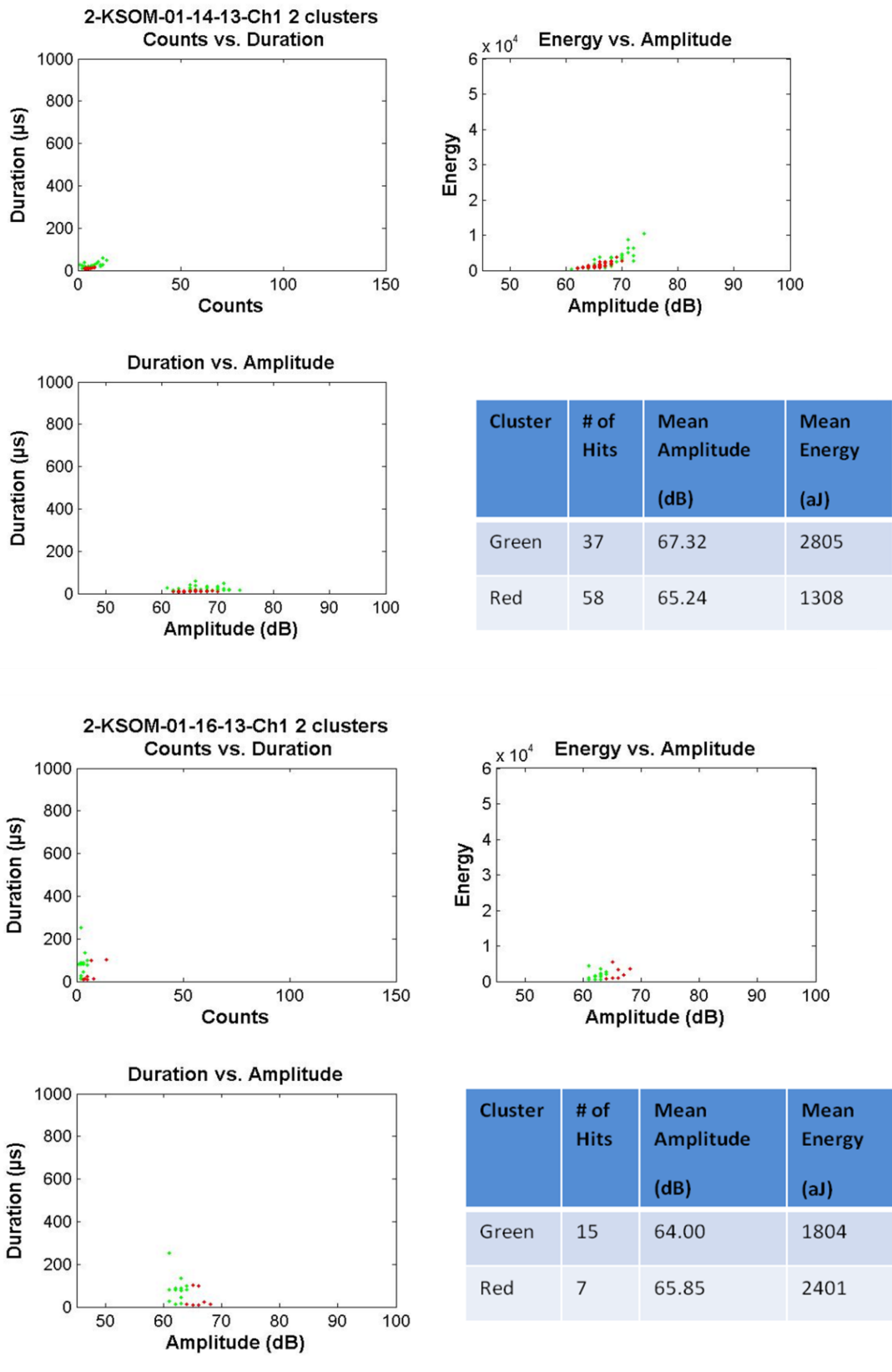
A.1 Navair Sensor Channel 1 Clustered AE Plots

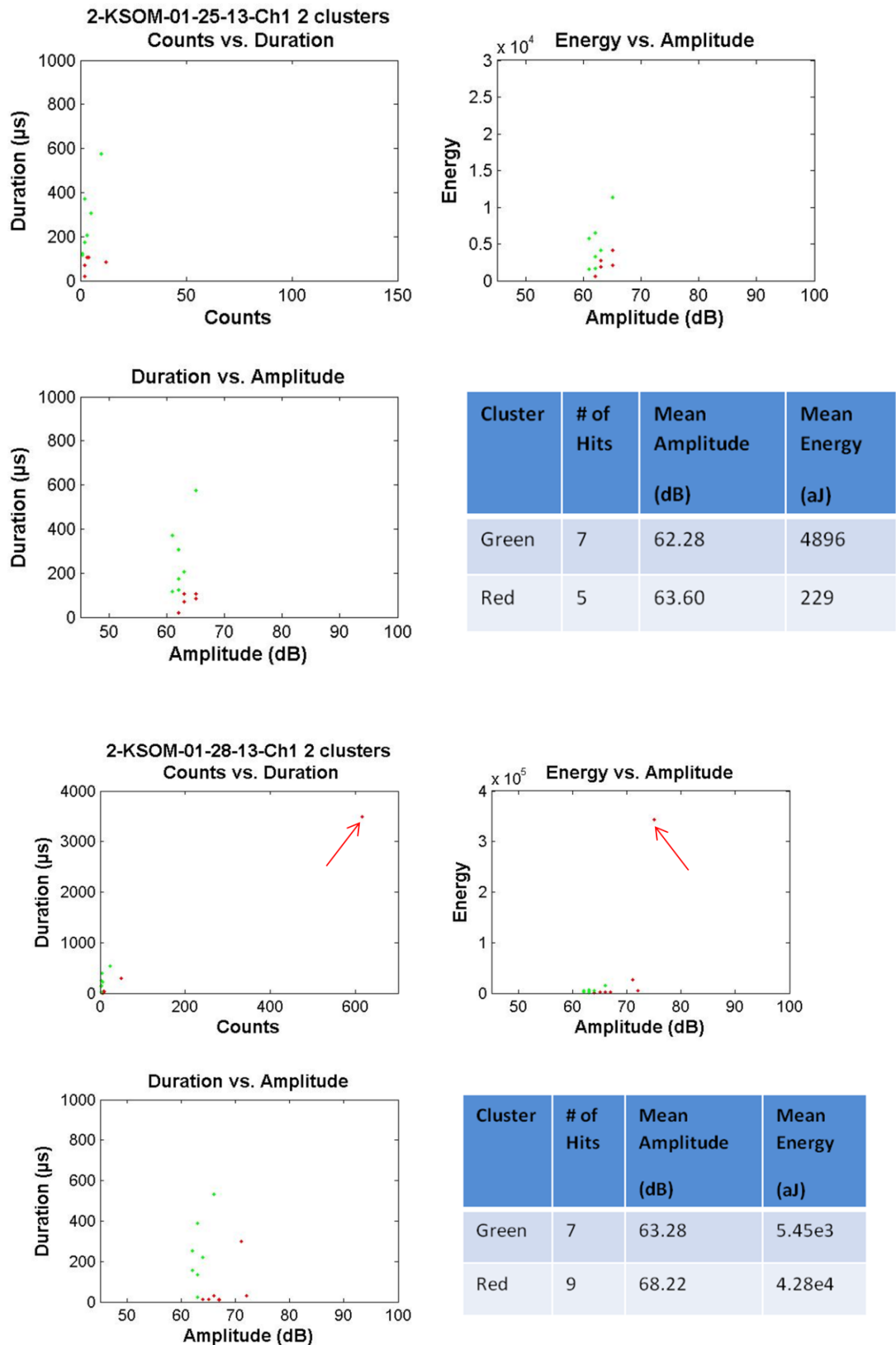


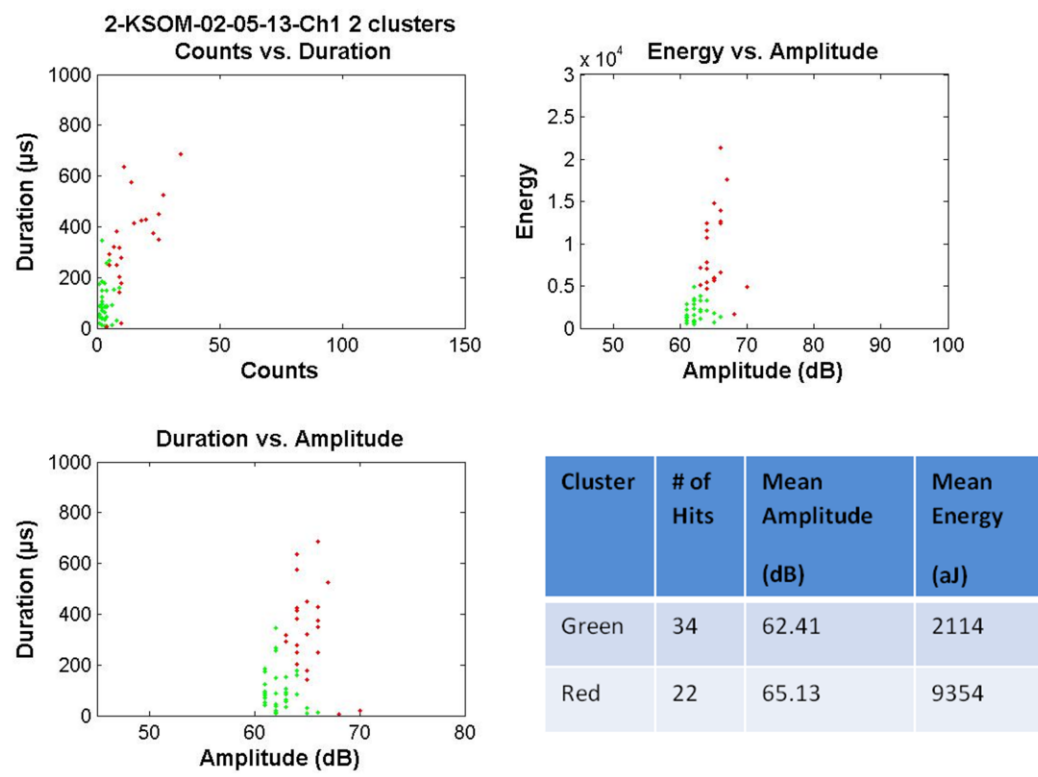
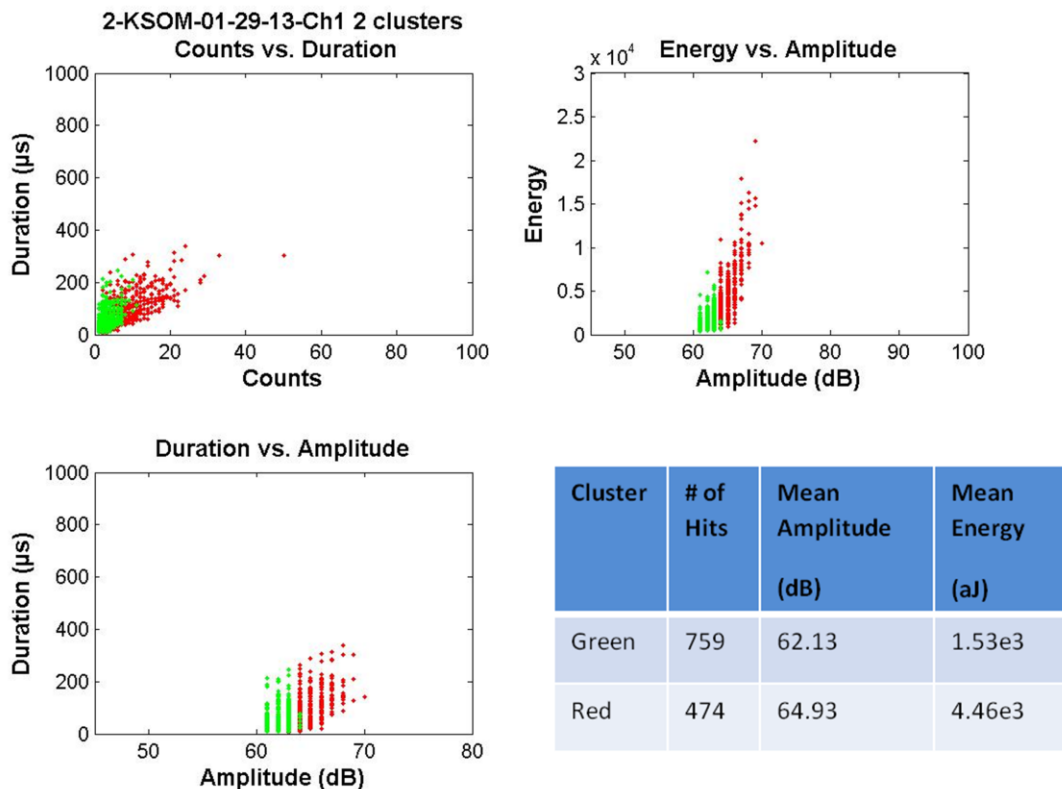


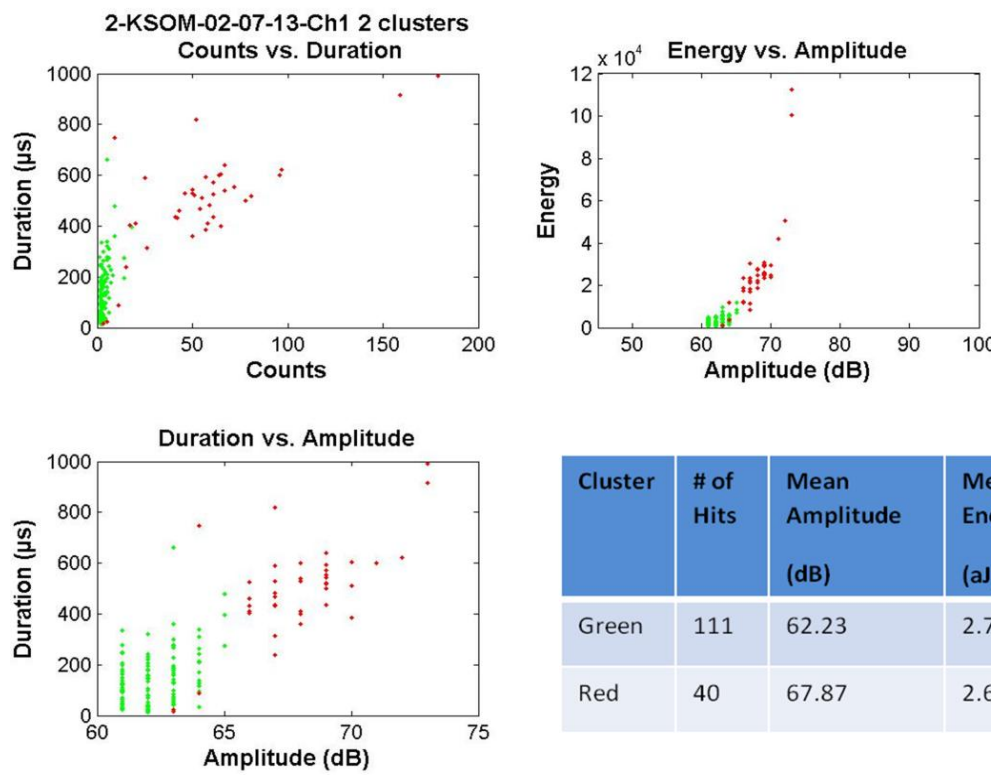
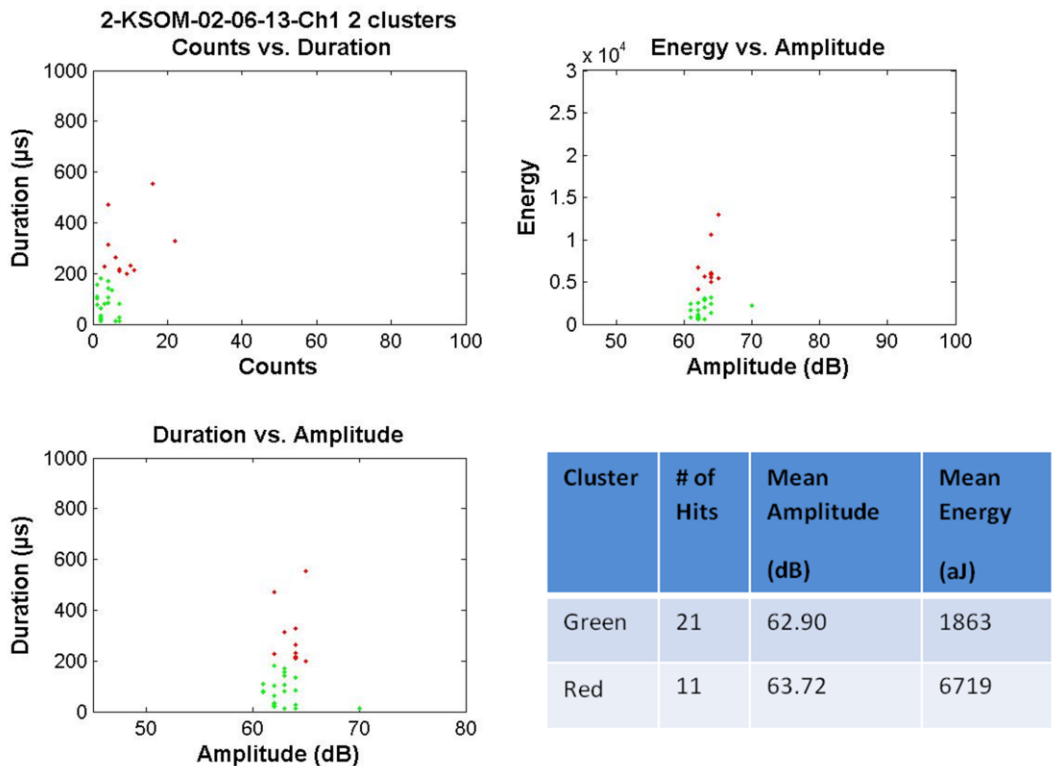


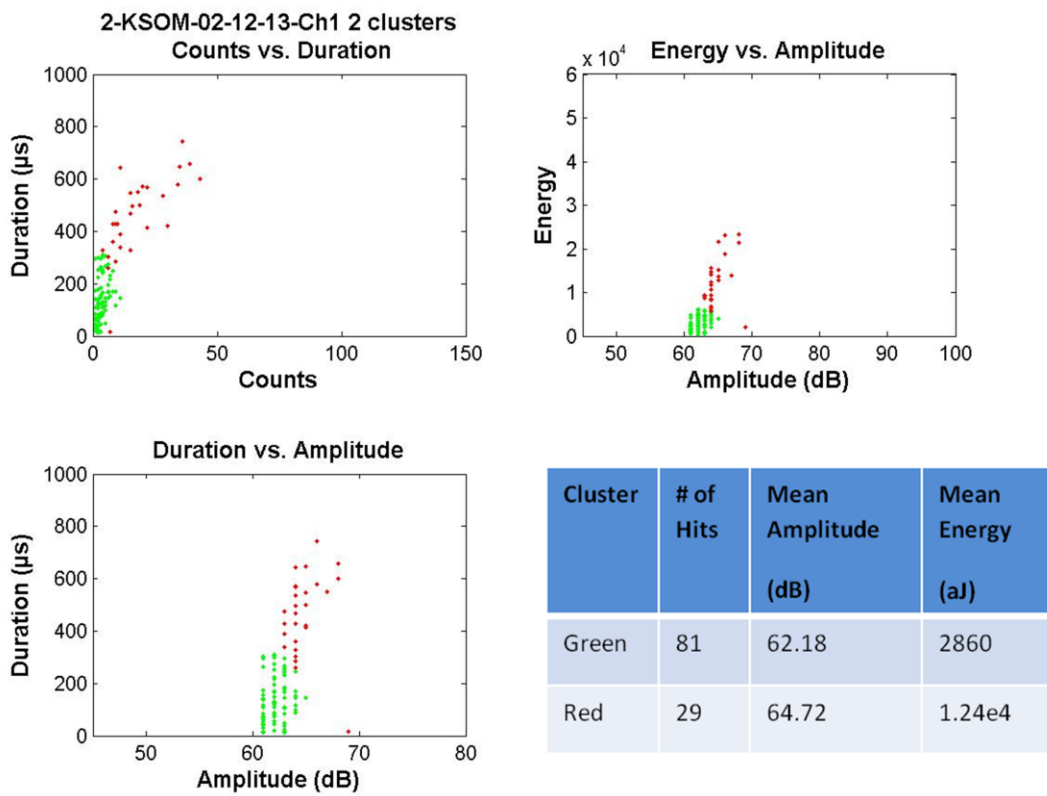
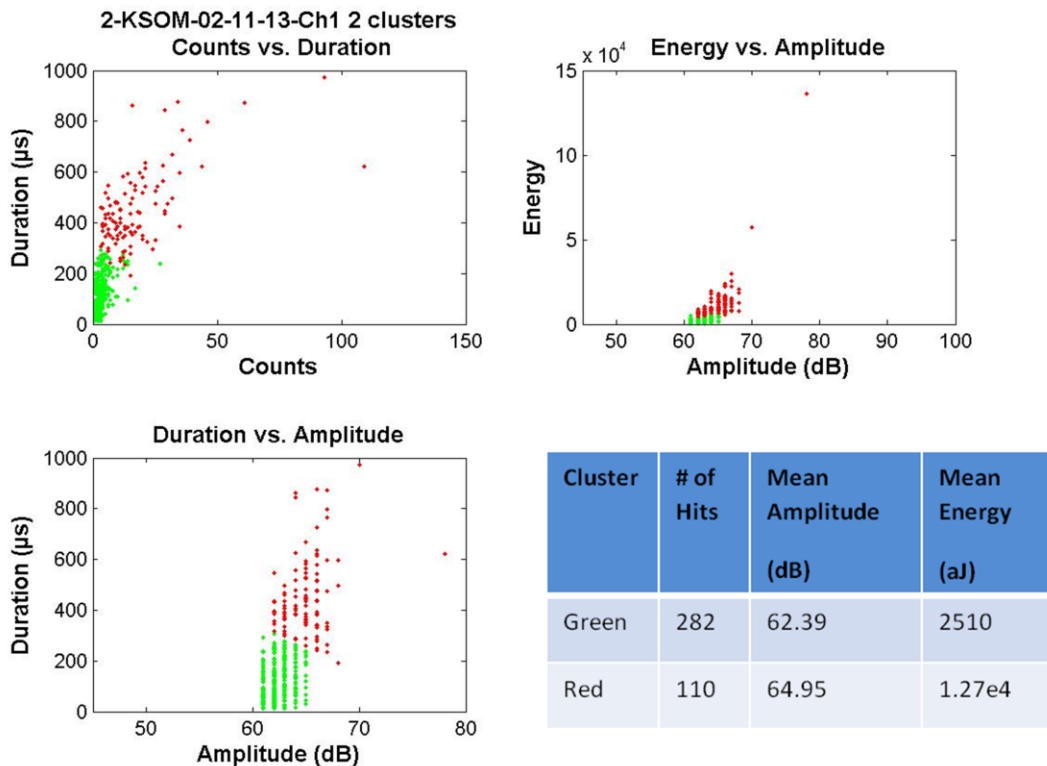




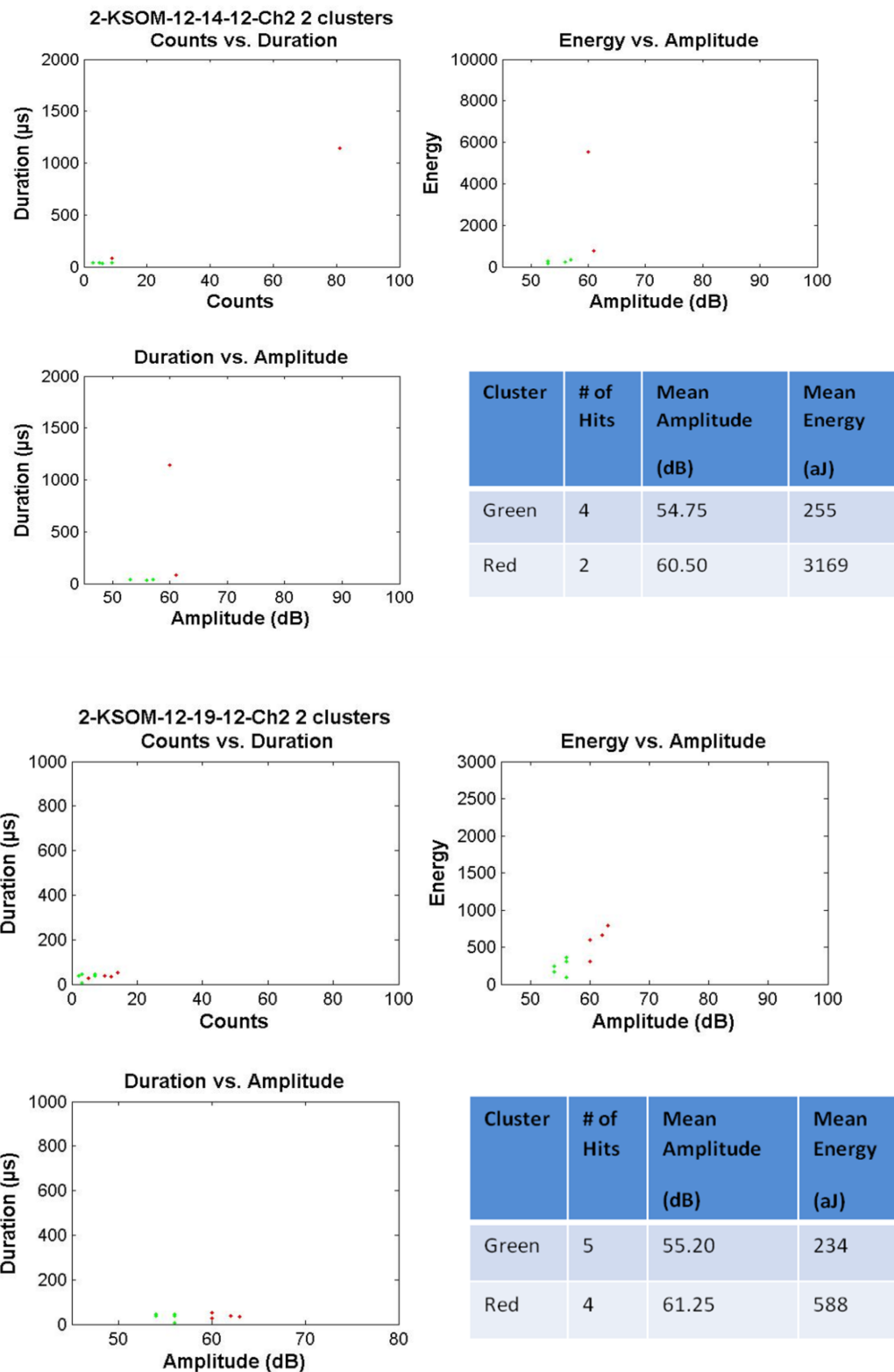


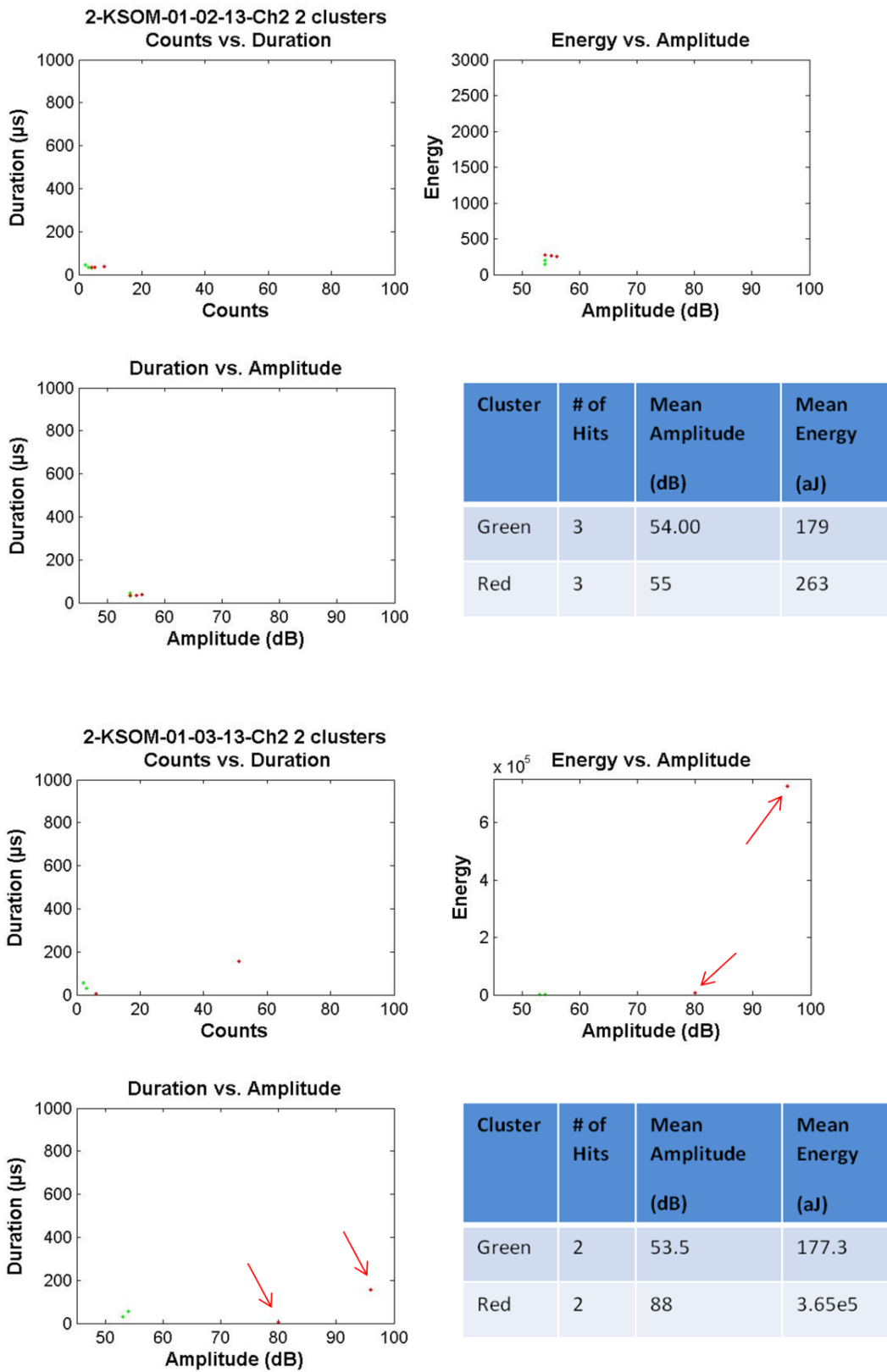


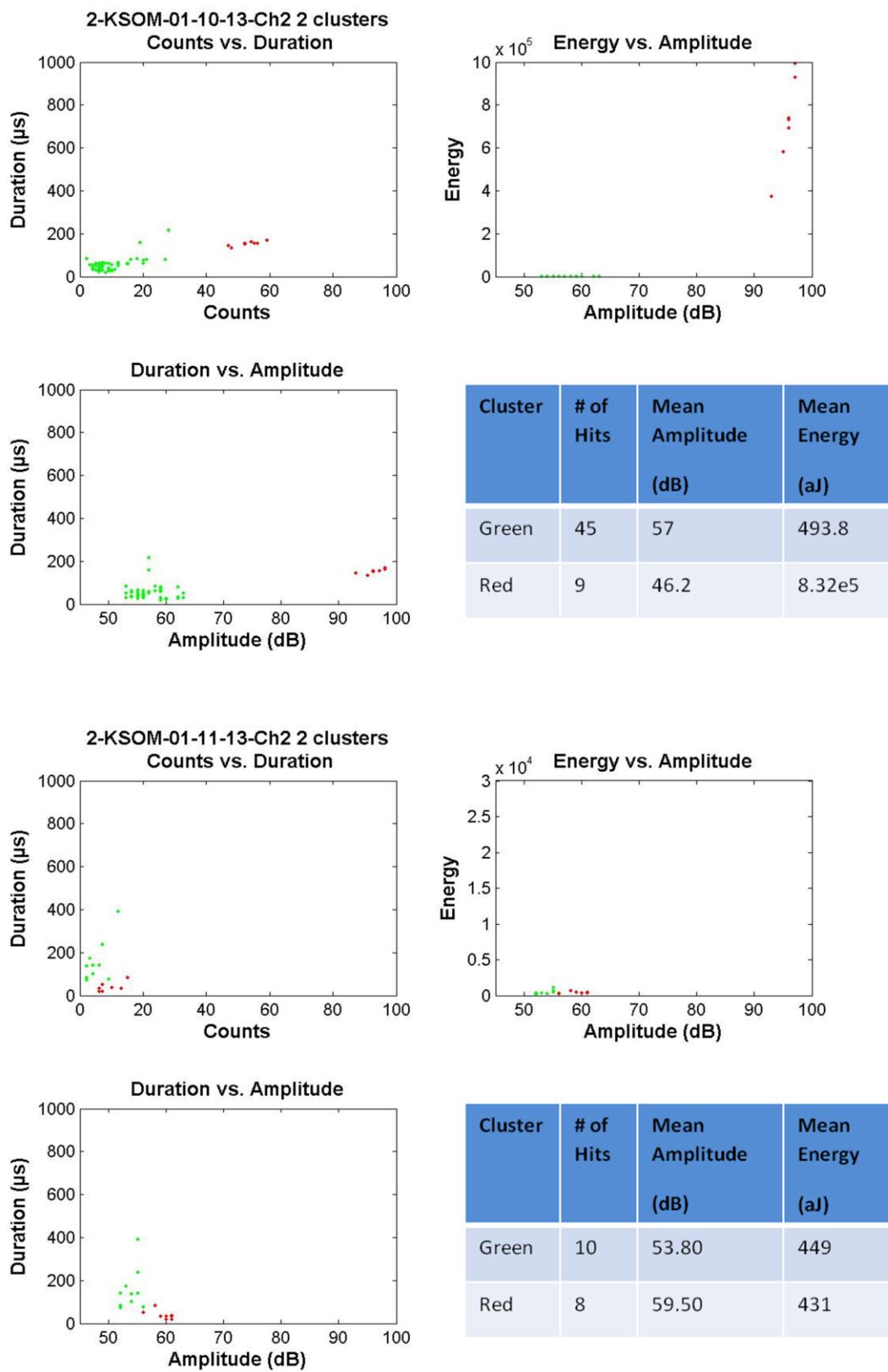


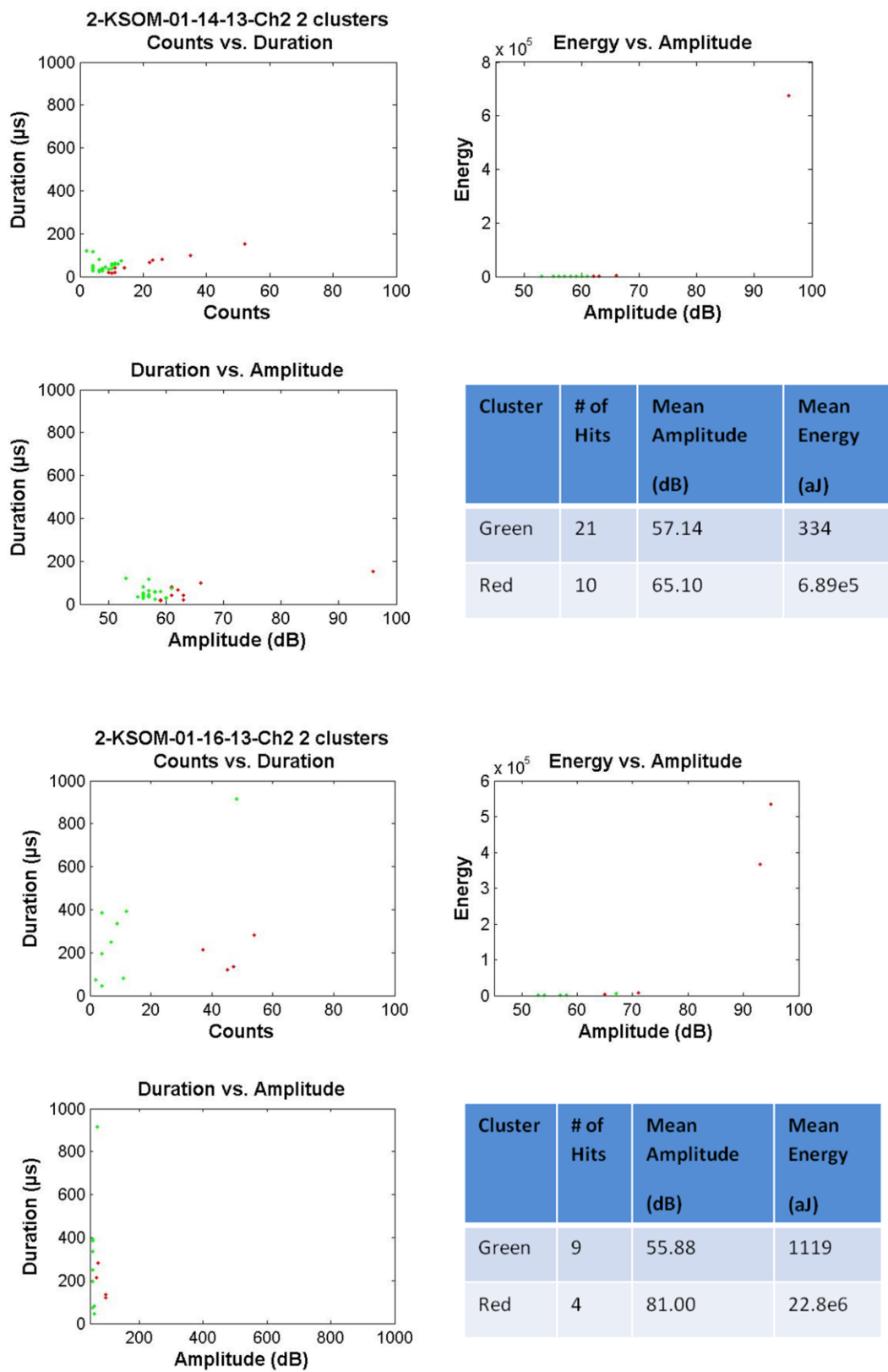


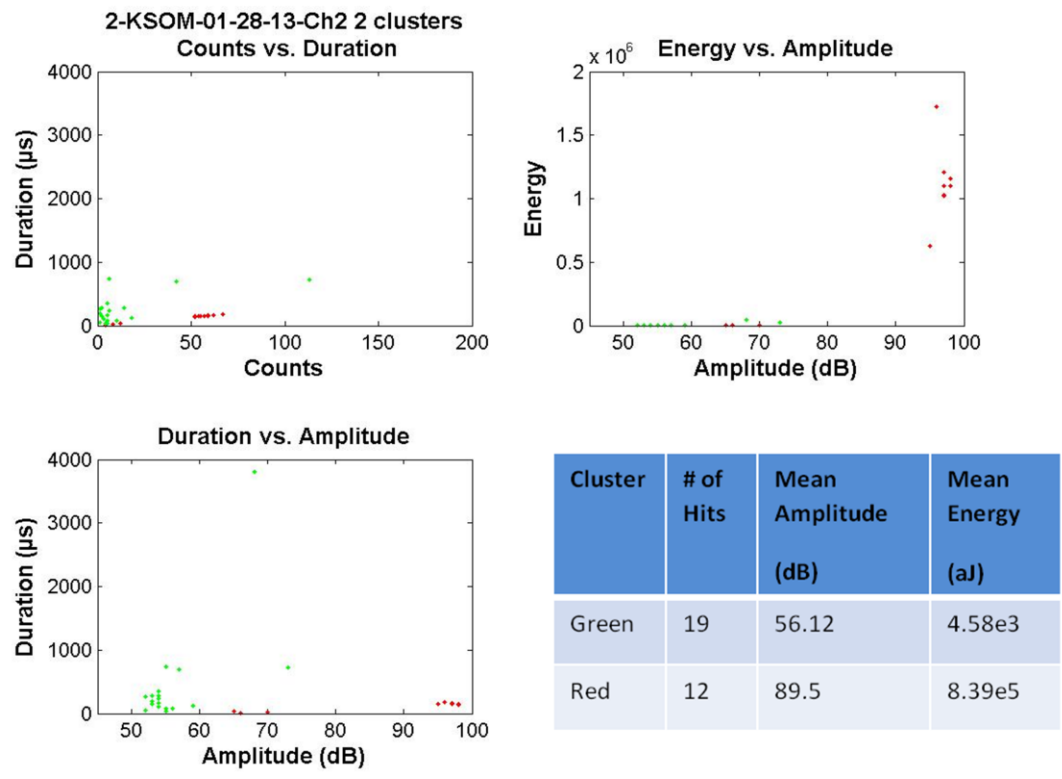
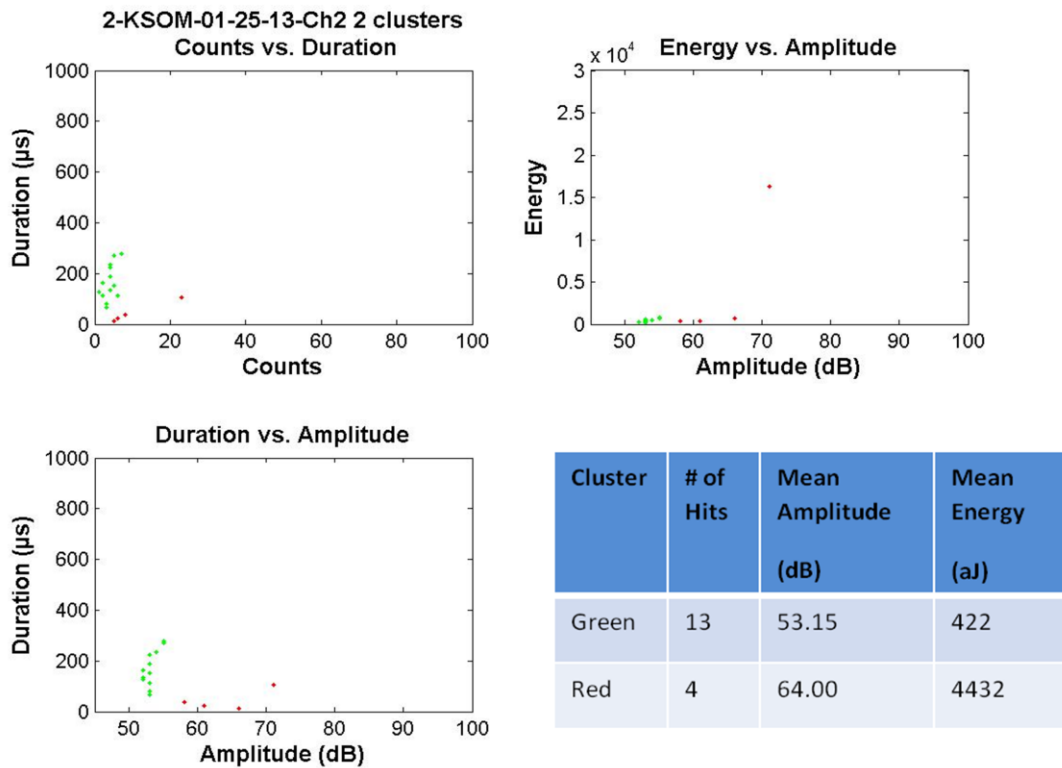
A.2 Navair Sensor Channel 2 Clustered AE Plots

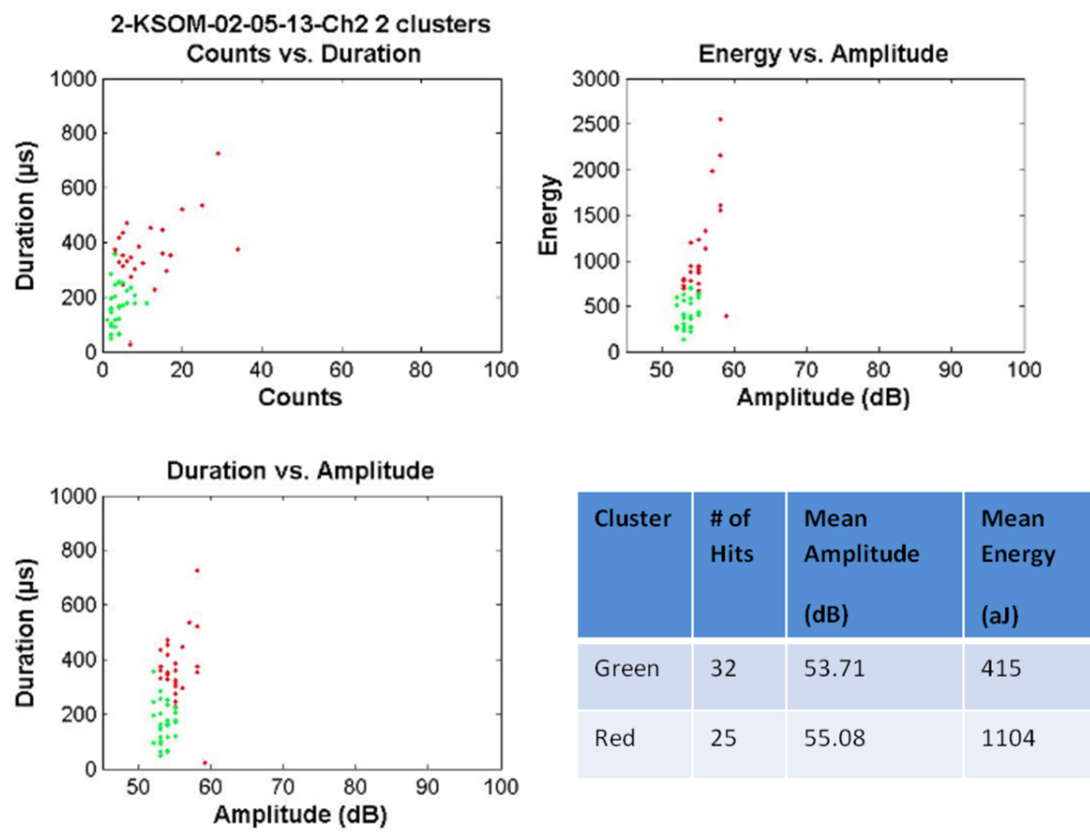
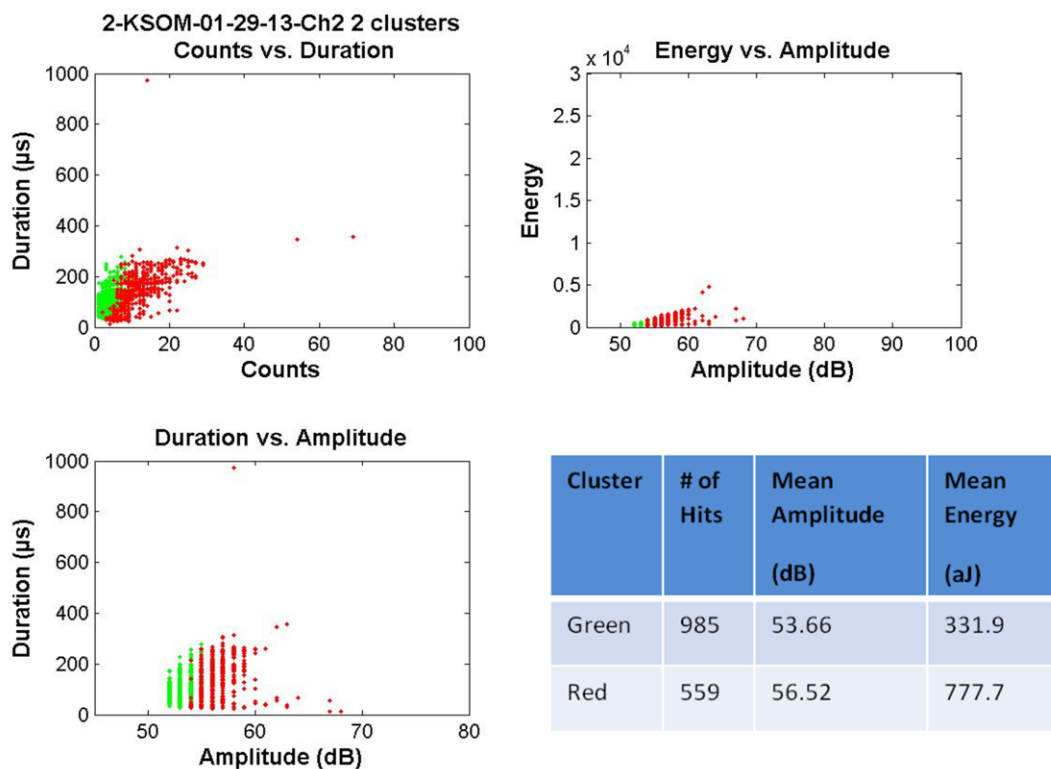


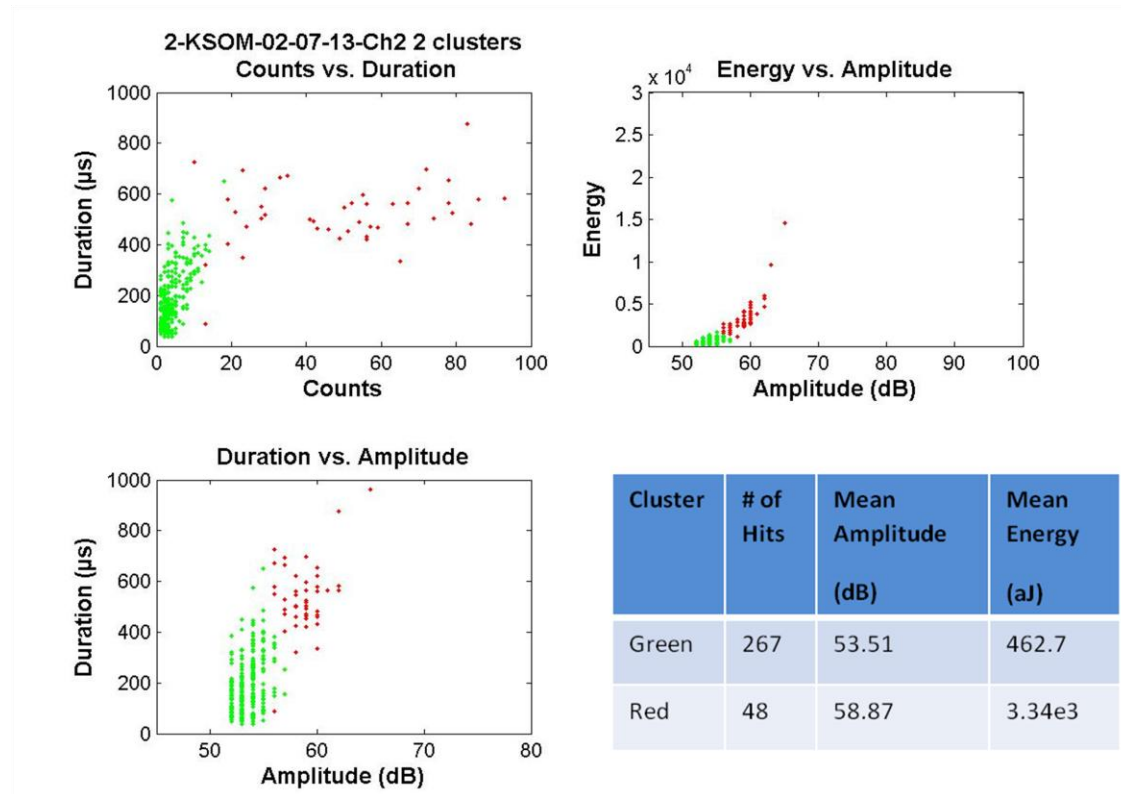
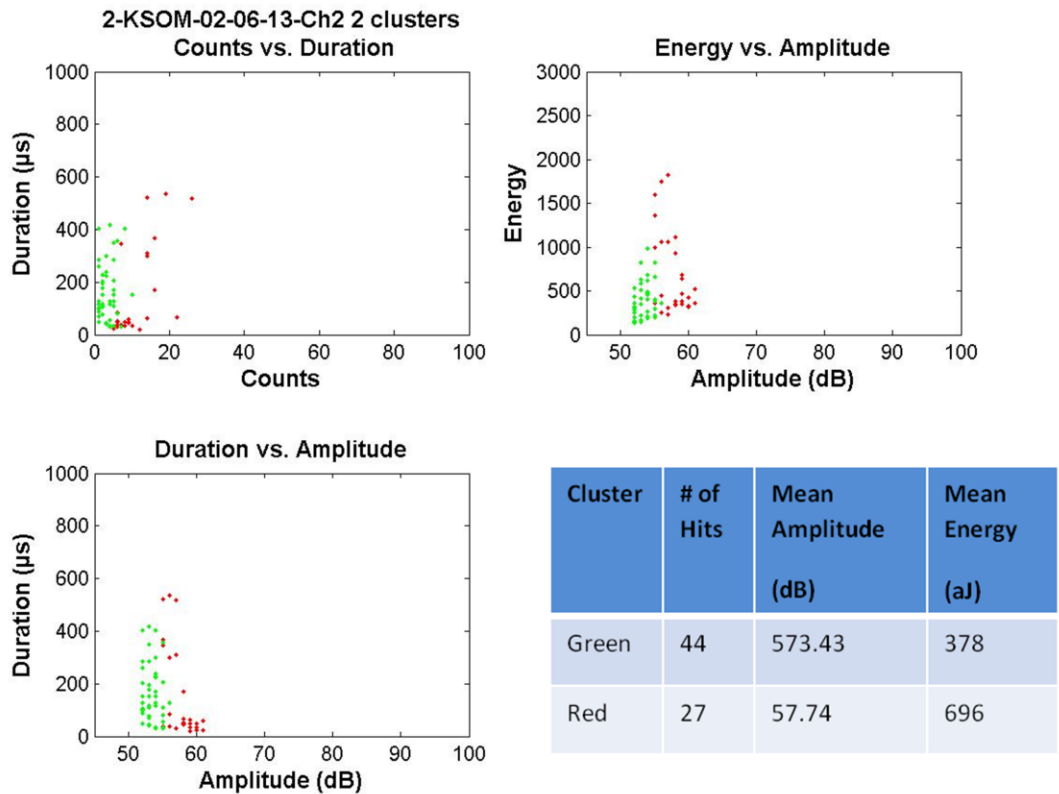


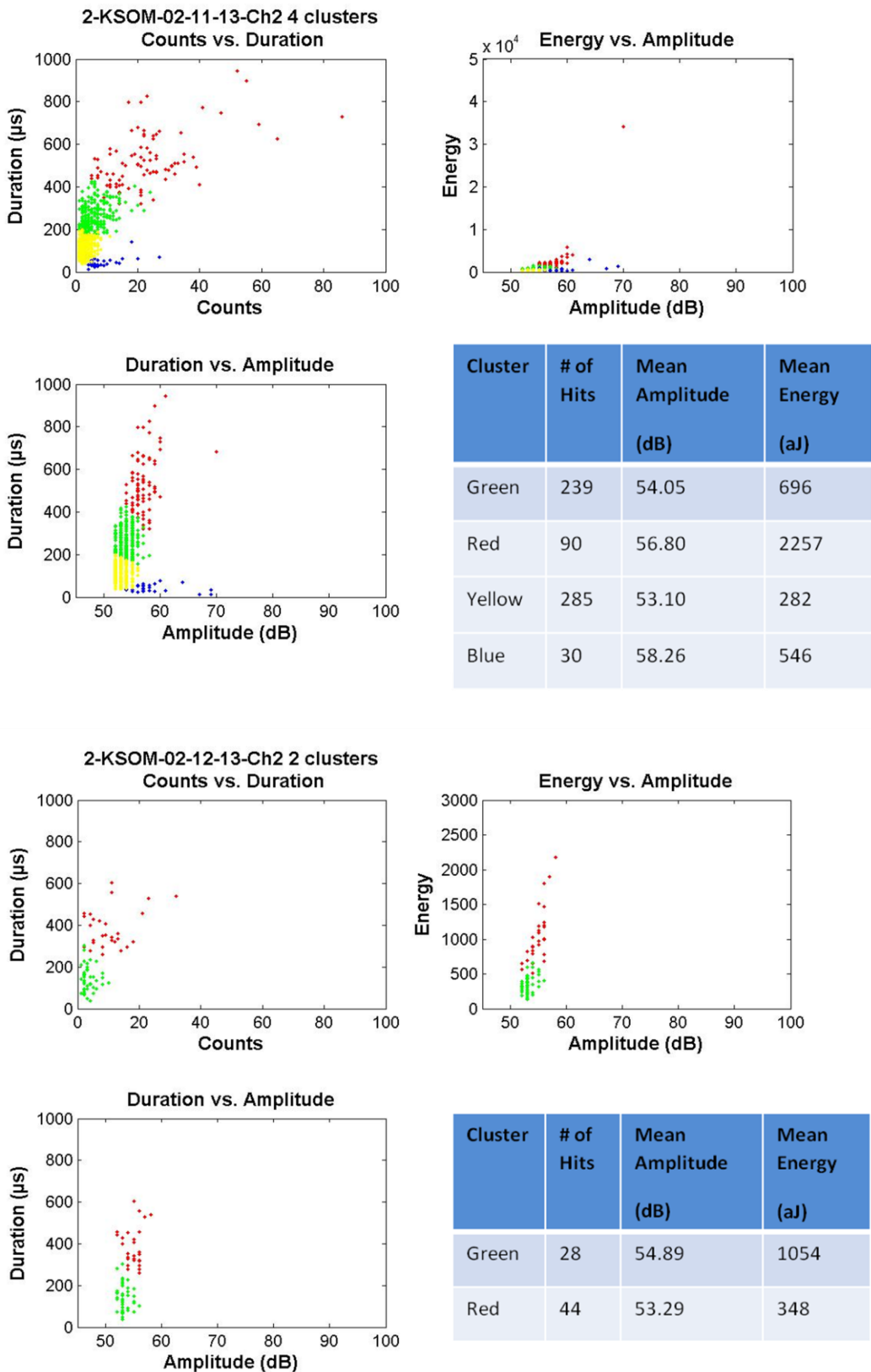




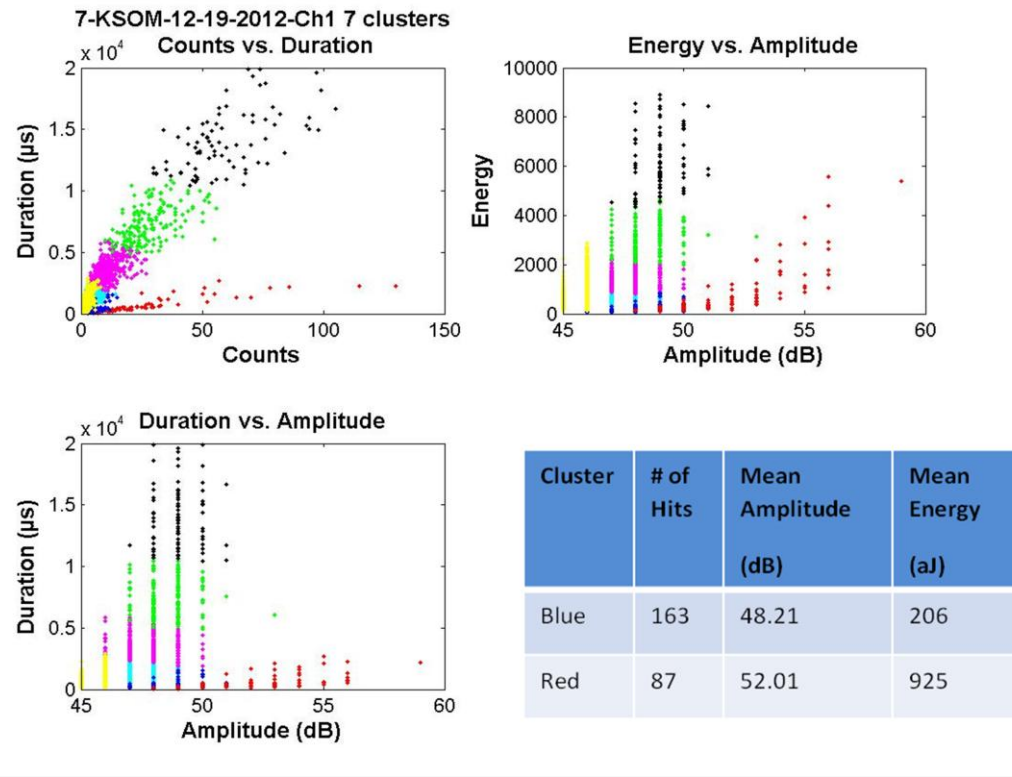
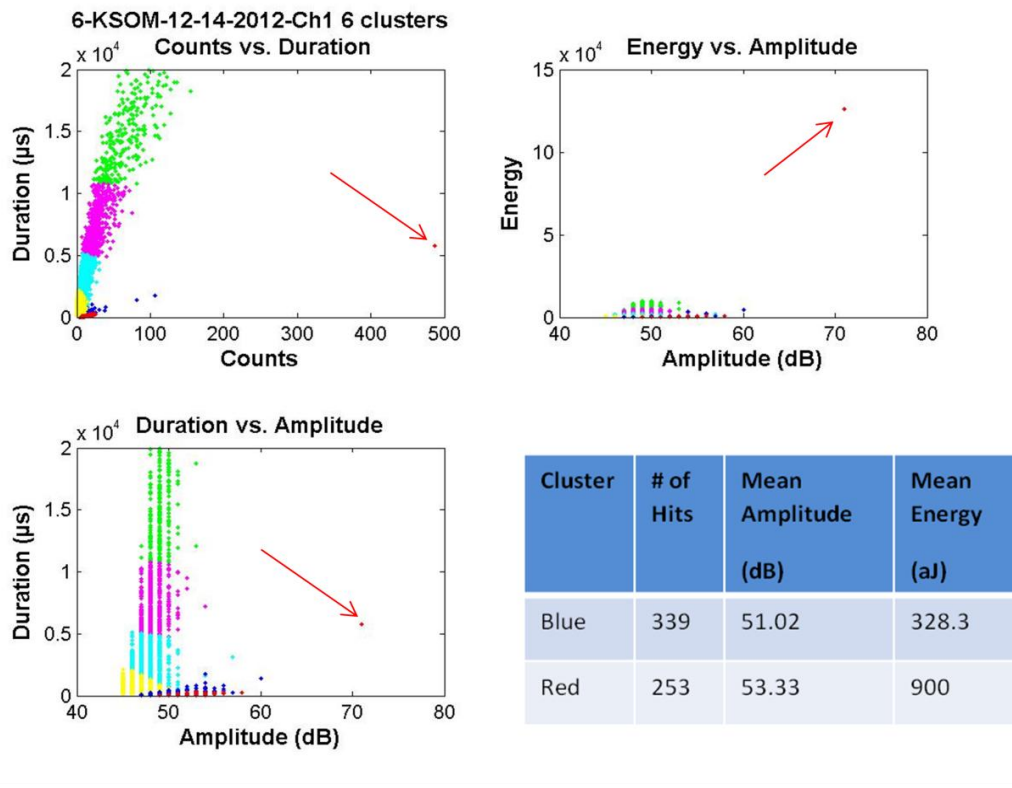


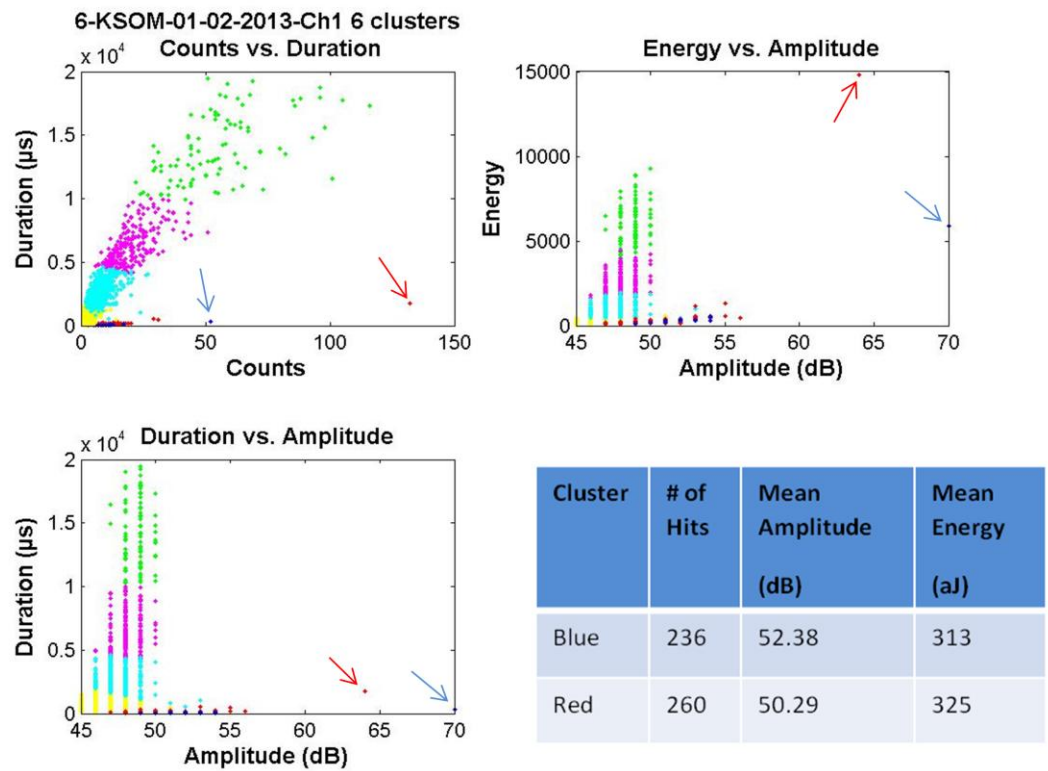
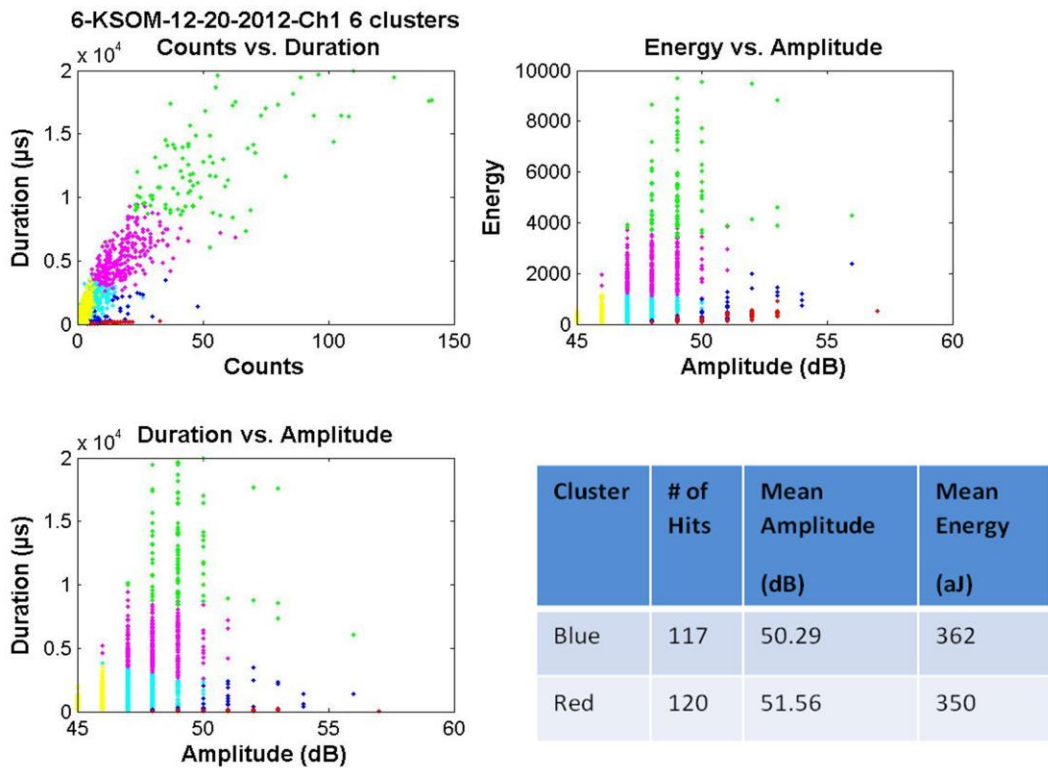


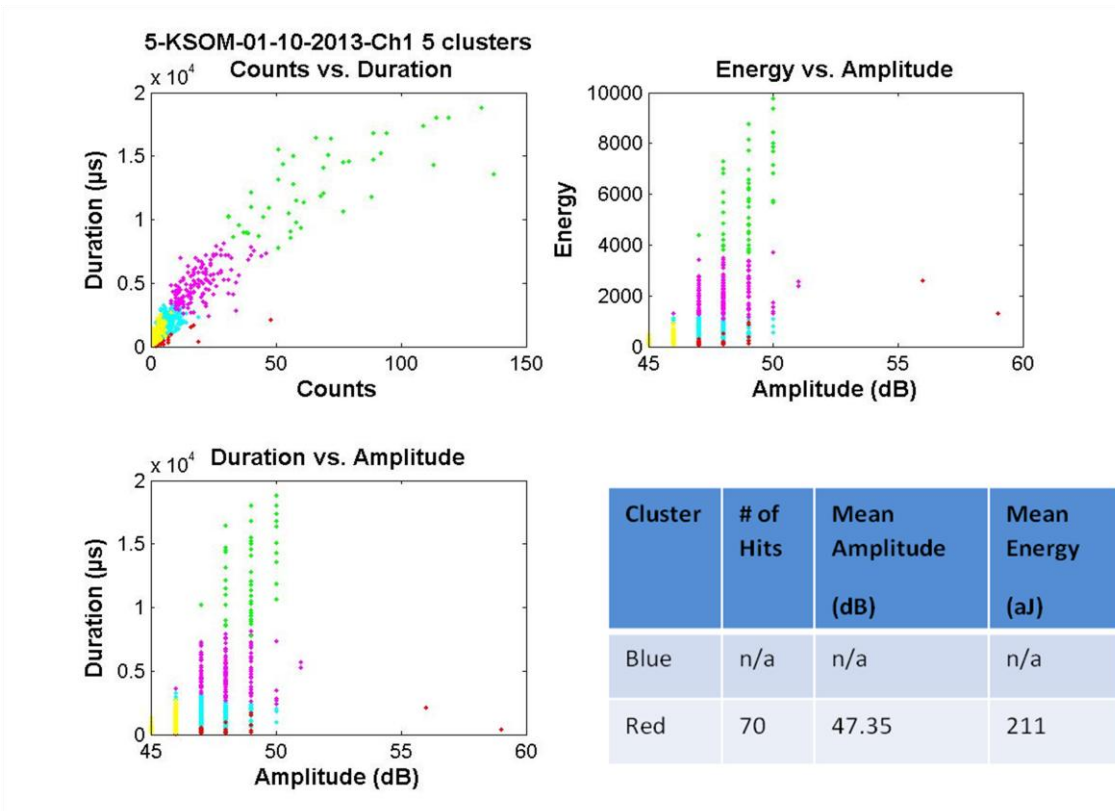
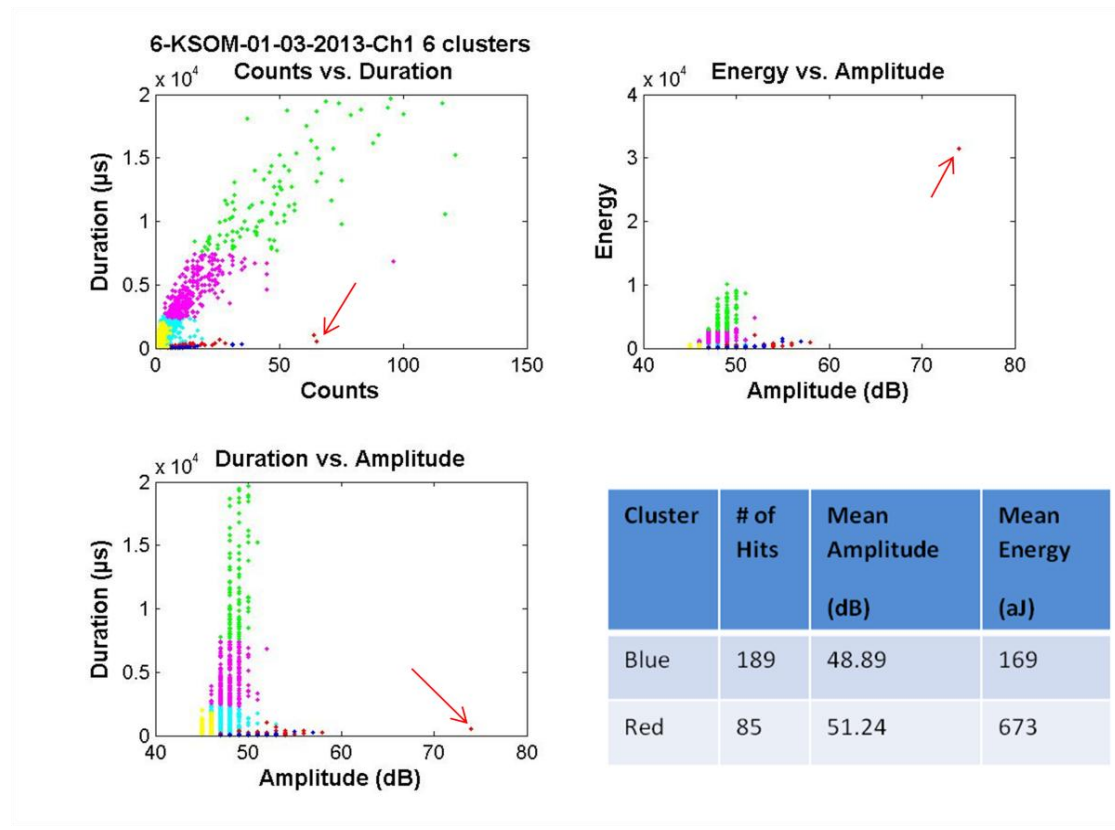


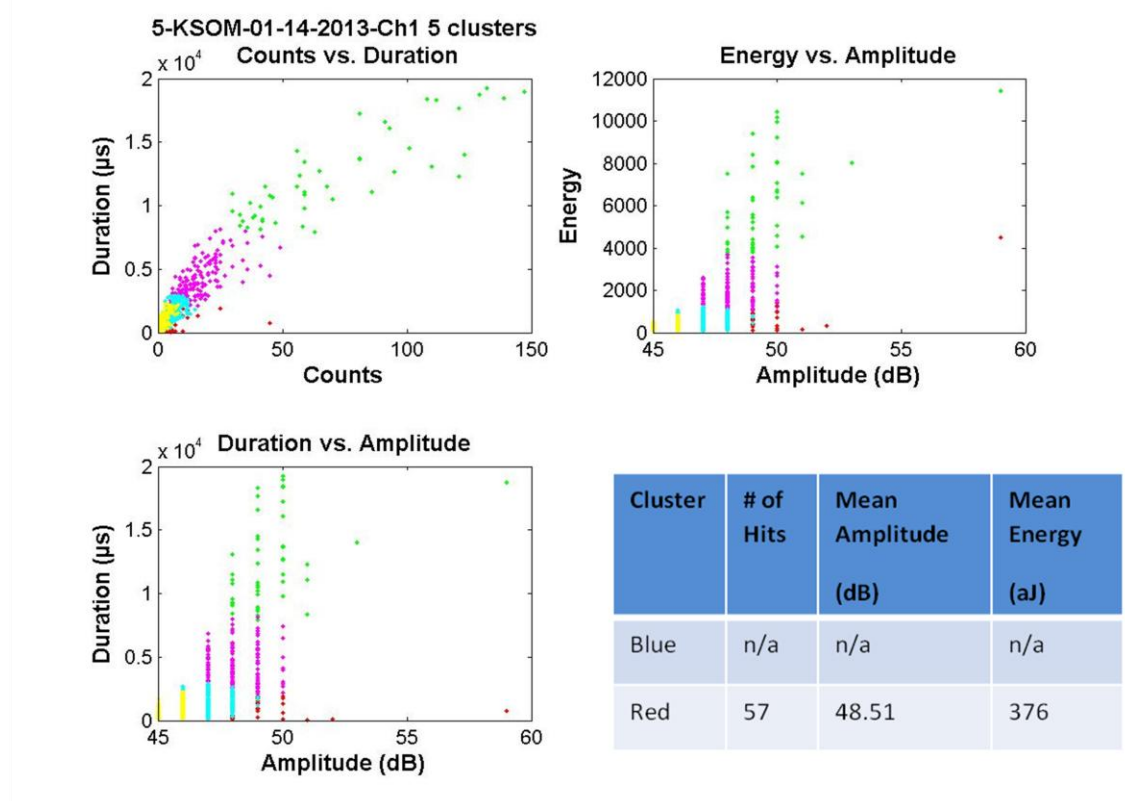
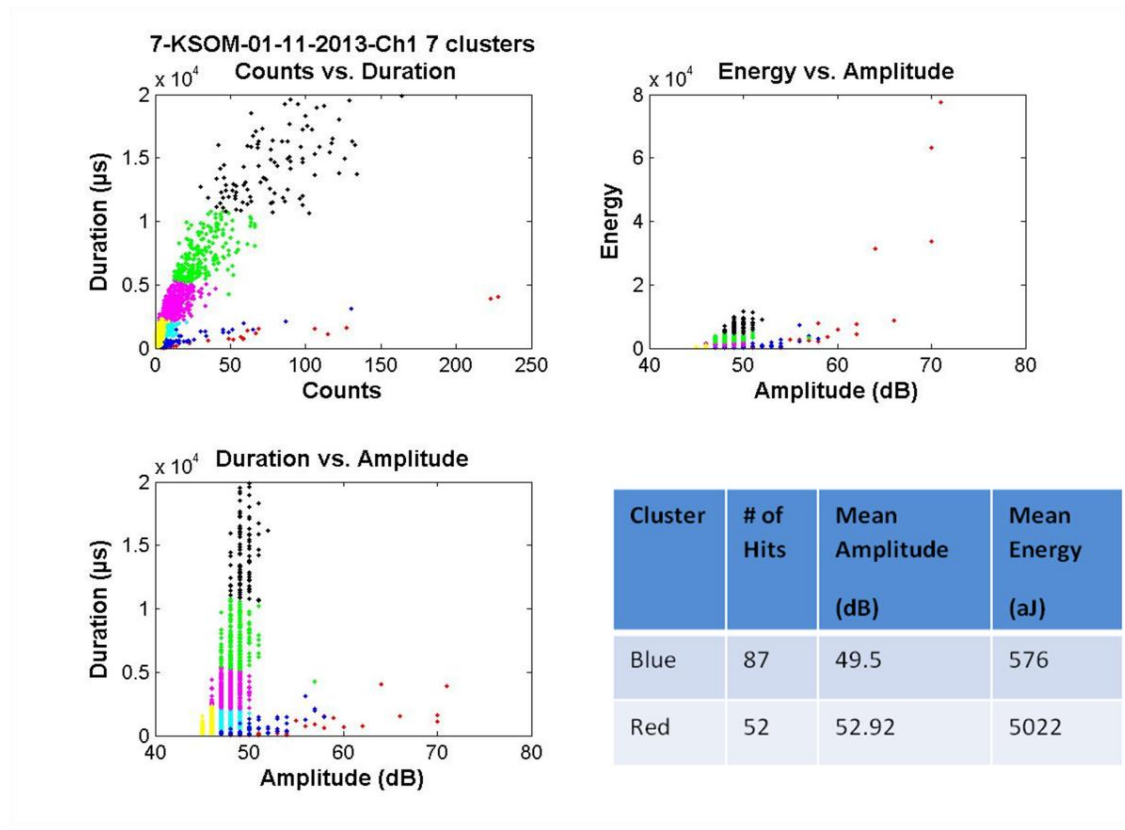


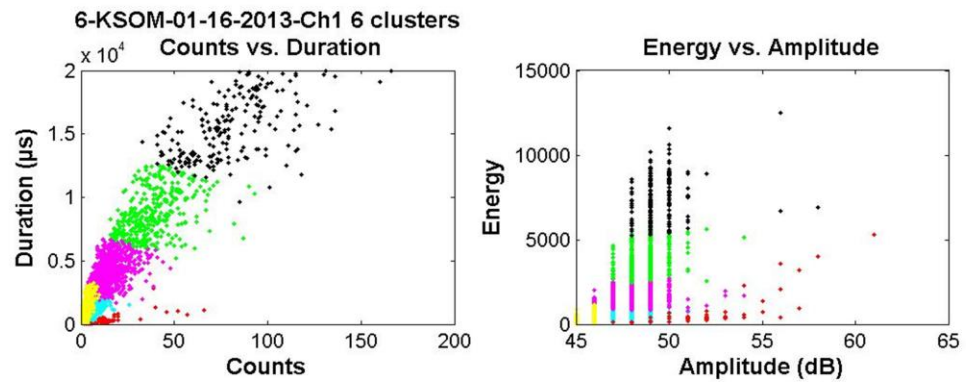
A.3 ERAU Sensor Channel 1 Clustered AE Plots



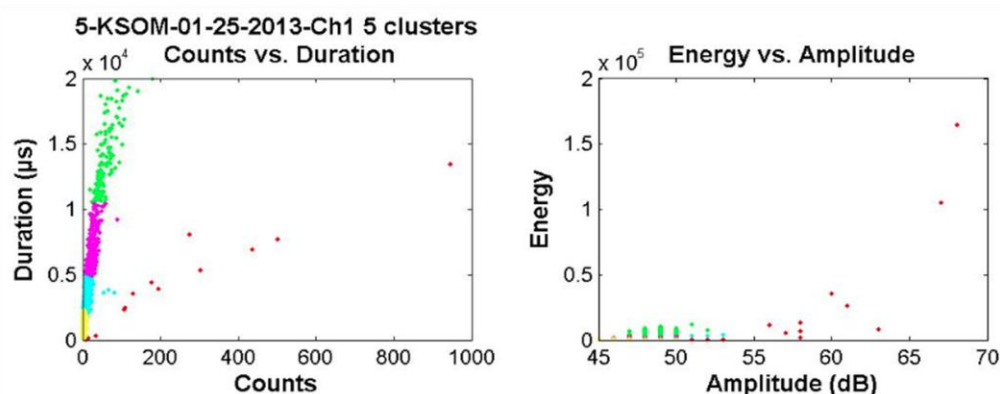




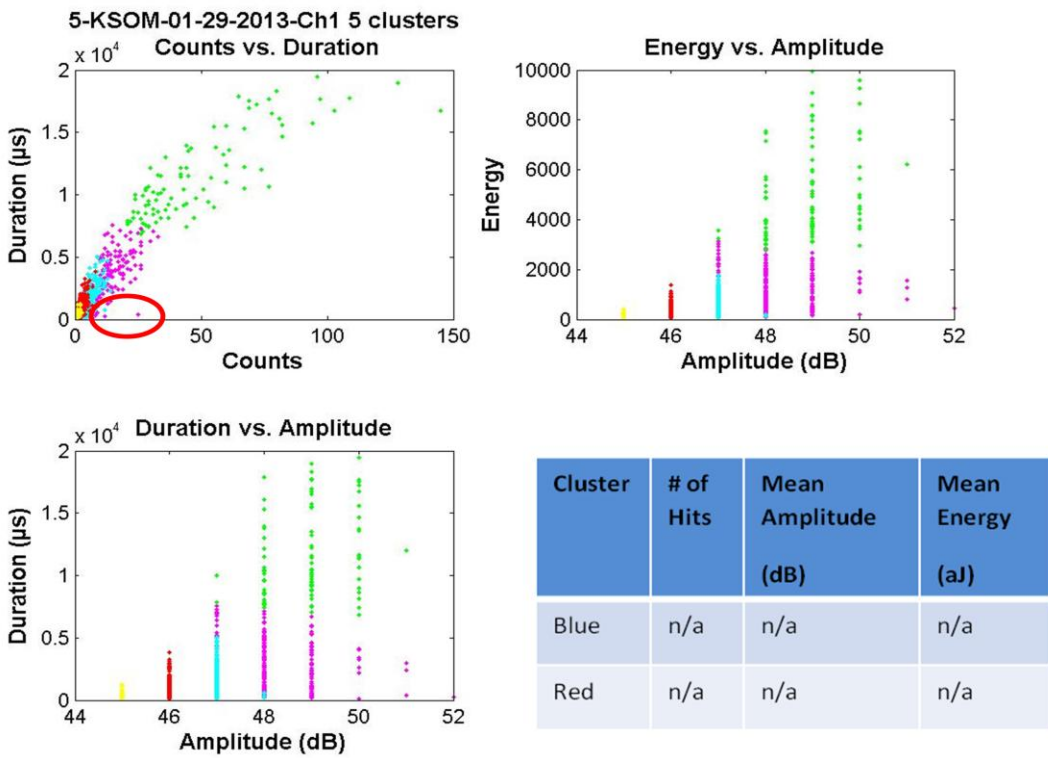
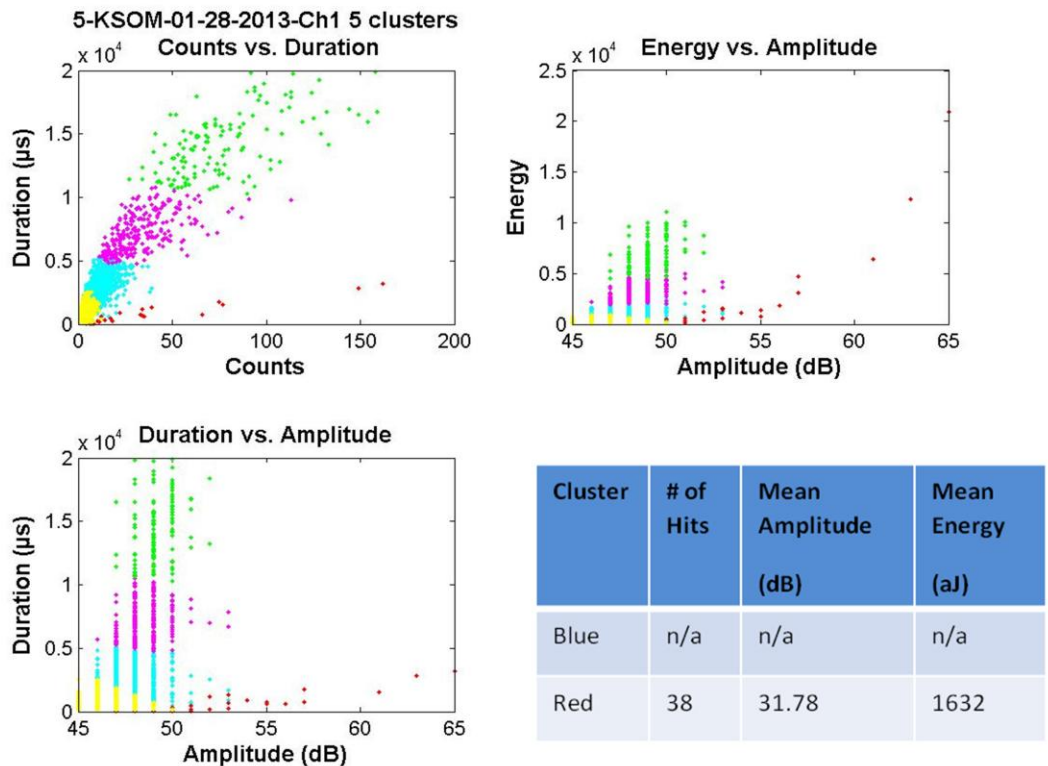




Cluster	# of Hits	Mean Amplitude (dB)	Mean Energy (aJ)
Blue	n/a	n/a	n/a
Red	56	52.21	730



Cluster	# of Hits	Mean Amplitude (dB)	Mean Energy (aJ)
Blue	n/a	n/a	n/a
Red	52	51.88	4300



APPENDIX B – Sensor Specification Sheets

B.1 PAC R15I-AST AE Transducer Product Data Sheet



R15I-AST Sensor

Integral Preamplifier
Acoustic Emission Sensor

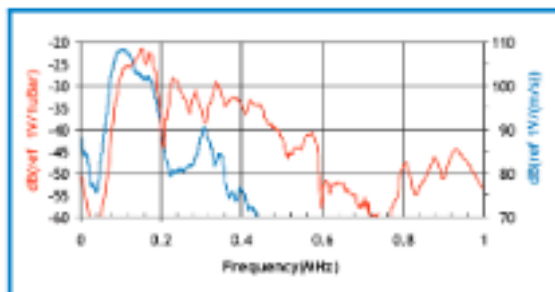
Description and Features

PAC's integral preamp sensors were specifically engineered to attain high sensitivity and have the capability to drive long cables without the need for a separate preamplifier. Incorporating a low-noise input, 40 dB preamplifier and a filter all inside the sensor housing, these transducers are completely enclosed in metal stainless steel (or aluminum) housings that are treated to minimize RFI/EMI interference. Care has also been taken to thermally isolate the critical input stage of the preamplifier in order to provide excellent temperature stability over the range of -35° to 75° C.

Their integrated Auto Sensor Test (AST™) capability allows these sensors to pulse as well as receive. This feature lets you verify the sensor coupling and performance at any time throughout the test.

Applications

This general purpose sensor provides a good mix of high sensitivity and high low frequency rejection. These properties make it very useful for monitoring common structures such as pipelines, vessels, bridges, and storage tanks in petroleum, refineries, chemical plants, offshore platforms, as well as factory and process monitoring applications. It is PAC's most popular and highest volume selling sensor.



Frequency response of the R15I-AST. Calibration based on ASTM E1106; Calibration based on ASTM E976.

Operating Specifications

Dynamic

Peak Sensitivity, Ref V/(m/s)	109 dB
Peak Sensitivity, Ref V/μbar	-22 dB
Operating Frequency Range	80-200 kHz
Resonant Frequency, Ref V/(m/s)	75 kHz
Resonant Frequency, Ref V/μbar	150 kHz
Directionality	+/-1.5 dB

Environmental

Temperature Range	-35 to 75°C
Shock Limit	500 g
Completely shielded crystal for maximum RFI/EMI immunity	

Physical

Dimensions	1.13" diameter x 1.23" h (29 x 31 mm)
Weight	70
Case Material	Stainless Steel (304)
Face Material	Ceramic
Connector	BNC
Connector Locations	Side

Ordering Information and Accessories

R15I	R15I-AST
Cable (specify cable length)	1234 - X
Magnetic Hold-Down	MHR15I
Amplifier	AE2A

Sensors include

NIST Calibration Certificate & Warranty

*AST – Auto Sensor Testing feature allows AE systems to control the sensor as a generator and a receiver at the same time. It can therefore characterize its own condition as well as send out a stimulated acoustic emission wave that other sensors can detect, so the condition of the nearby sensors also can be tested.



MISTRAS
A World of NDT Solutions

Product & Systems
Division

195 Clarksville Road, Princeton Junction, NJ 08550

Phone: 609-718-4000 • Fax: 609-718-0706 •

Email: sales.systems@mistrasgroup.com • www.mistrasgroup.com



B.2 PAC WD AE Transducer Product Data Sheet

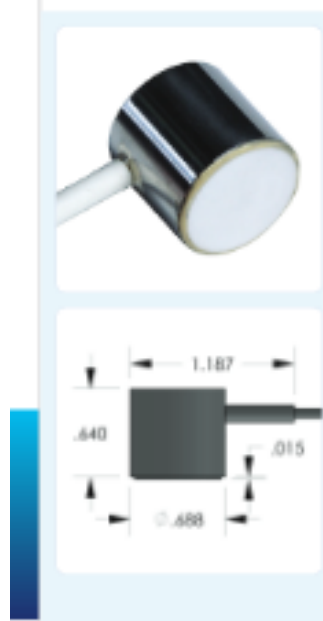


Products & Systems
Division



WD Sensor

Wideband Differential Sensor

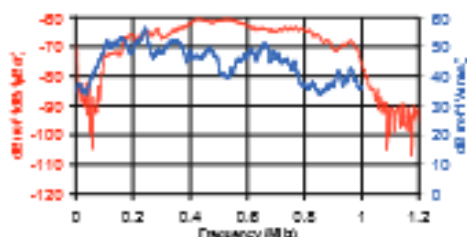


DESCRIPTION AND FEATURES

WD is a true differential wideband sensor with a very high sensitivity and bandwidth. It has a very good frequency response over the range of 100 – 900 kHz. Differential sensors differ from their general purpose counterparts by employing two sensing elements with opposite polarization directions. The two signal leads feed into a differential pre-amplifier which eliminates common-mode noise resulting in a lower noise output from the pre-amplifier. Noise improvements to the tune of 2 dB can be achieved using differential sensors over a single ended sensor. This sensor features a rugged steel construction with an integrated twin cable exiting on the side.

APPLICATIONS

This sensor is well suited for structural health monitoring of large structures like storage tanks, pipelines etc. This sensor is an ideal candidate for applications requiring high bandwidth for frequency analysis of the AE signals for noise discrimination and source identification. Wideband sensors are particularly well suited for research applications where a high fidelity AE response is required. It can be easily mounted using epoxy.



PRODUCT DATA SHEET

OPERATING SPECIFICATIONS

Dynamic	
Peak Sensitivity, Ref V/m/s	-56 dB
Peak Sensitivity, Ref V/pbar	-61 dB
Operating Frequency Range	100-1000 kHz
Resonant Frequency, Ref V/m/s	125 kHz
Resonant Frequency, Ref V/pbar	450 kHz
Directionality	+/-1.5 dB

Environmental	
Temperature Range	-45 to 177°C
Shock Limit	500 g
Completely enclosed crystal for RFI/GMI immunity	

Physical	
Dimensions	.07 OD x .057 H
	17.8 mm OD x 15.5 mm H
Weight	30 grams
Case Material	Stainless Steel
Race Material	Ceramic
Connector	SNC
Connector Locations	Side

ORDERING INFORMATION AND ACCESSORIES

WD	
Cable (specify length in 'm' instead of 'ft')	1 m
Magnetic Hold-Down	MHSTD
Pre-Amplifier	Q1/4, 2/4/8
Preamplifier to System Cable (specify length in 'm')	1224-K
Amplifier Subsystems	AESA or AESA

Sensors include:

NIST Calibration Certificate & Warranty



B.3 PAC Micro-30s AE Transducer Product Data Sheet

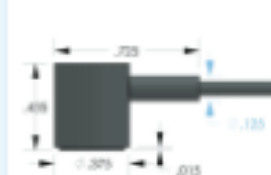


Products & Systems
Division



Micro30S Sensor

Miniature Sensor

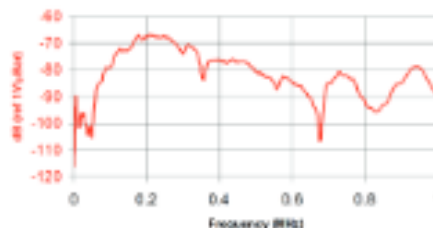


DESCRIPTION AND FEATURES

Micro30S sensor has a good frequency response over the range of 150 – 400 kHz. It has good sensitivity to AE signals even in presence of high background noise. Its small size and good bandwidth makes the sensor an ideal candidate for applications that have size and weight constraints on the sensors. The sensor features a small diameter, an integrated coaxial cable exiting from the side of the sensor.

APPLICATIONS

The high sensitivity and bandwidth makes them ideal for structural health monitoring of critical structures like aircrafts, storage tanks etc. Typical applications include monitoring for fatigue and corrosion cracking in metals, delaminations and fiber breakage in composites. It can be mounted easily using epoxy.



PRODUCT DATA SHEET

OPERATING SPECIFICATIONS

Dynamic	
Peak Sensitivity, Ref V/m/s	-65 dB
Peak Sensitivity, Ref V/μbar	-87.5 dB
Operating Frequency Range	150-400 kHz
Resonant Frequency, Ref V/m/s	125 kHz
Resonant Frequency, Ref V/μbar	225 kHz
Directionality	+/-1.5 dB

Environmental	
Temperature Range	-65 to 177°C
Shock Limit	500 g
Completely enclosed crystal for RR/GMI immunity	

Physical	
Dimensions	.047OD X 0.57H 10 mm OD X 12 mm H
Weight (g)	5 grams
Case Material	Stainless steel
Face Material	Ceramic
Connector	Milnorot
Connector Locations	Side

ORDERING INFORMATION AND ACCESSORIES

Micro30	Micro30
Cable (specify length in 'm' at end of PN)	1223-1
Preamplifier	0/1/4, 2/4/8
Preampl to System Cable (specify length in 'm')	1224-X
Amplifier Subsystems	AESA, AESA

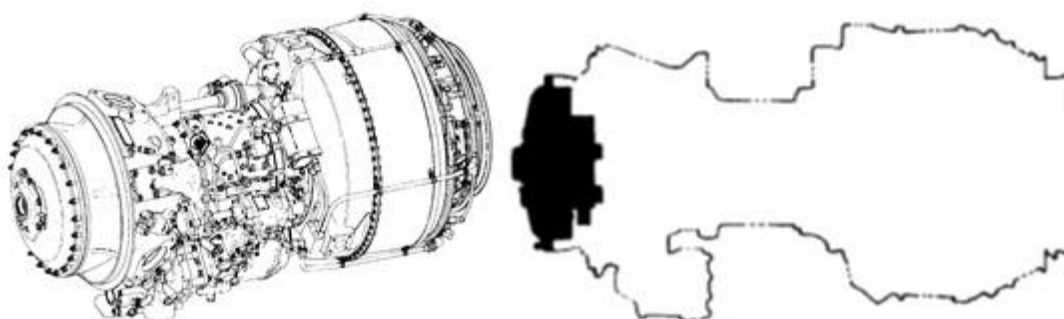
Sensors include
NIST Calibration Certificate & Warranty



APPENDIX C – Lycoming T-53 Test Stand

C.1 Lycoming T-53 Test Stand Design

In an effort to further develop acoustic testing and filtering techniques for this research, a test stand was designed and assembled at ERAU. This in-house test stand provides the opportunity to pursue some parametric studies to refine data acquisition techniques such as sensor types and location, amplitude threshold, shaft speed, time definition, and sampling rate. These improvements will ultimately be used to further develop the testing methods, data acquisition techniques and analysis procedures. The Lycoming T-5, 1-030-350-18, turbo shaft engine reduction gearbox is used. The stand has been designed to allow for the placement of acoustic emission transducers directly on a gear to minimize the attenuation of the recorded AE signal. The gearbox is driven by a 20 horsepower WEG three-phase electric motor at variable speeds using an L300P-150HFU2 Hitachi motor controller to generate acoustic noise signals similar in nature to the H60 ground test stand operation. This engine and gearbox location can be seen in the following figure:



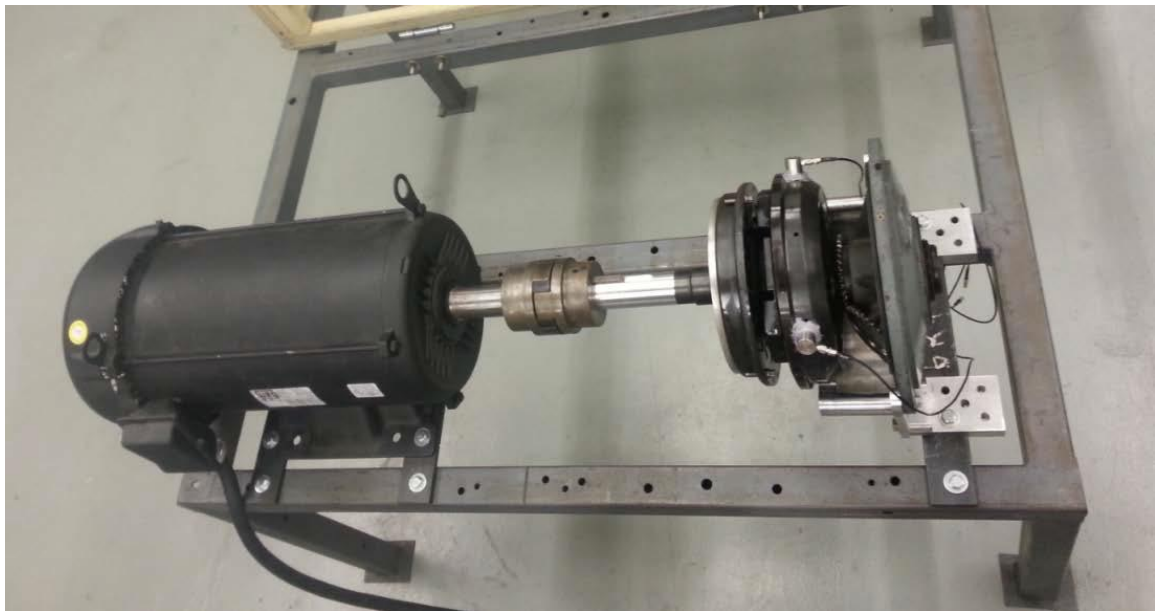
The WEG three-phase motor and Hitachi motor controller can be seen in the figure below.



The three-phase electric motor and T-53 gearbox were connected via a spline driveshaft and elastomer coupling. This coupling was used in order to reduce vibrations and minimize metal-on-metal rubbing. An oil bath tub is utilized to simulate a typical operational gearbox lubrication system. Lubrication further assists in minimizing acoustic emissions generated from gear lash. The elastomer coupling between splined shafts of the three phase motor and T-53 gearbox is shown in the figure below.



The overall test stand is depicted in the following figure:



C.2 T-53 Test Stand Data Acquisition

The PAC Pocket AE-2 portable AE data acquisition device is utilized to record AE data from sensors mounted on the ring gear as shown below. R15a sensors have a peak sensitivity of 69 dB, a resonant frequency of 150 kHz, and an operating frequency range of 50 kHz to 400 kHz.

